

博士論文

Reaction of formic acid on copper model catalysts studied by surface spectroscopies

(表面分光法を用いた銅系モデル触媒における
ギ酸の反応に関する研究)

塩澤 佑一朗

**Reaction of formic acid on copper model
catalysts studied by surface spectroscopies**

**A Thesis Submitted to the University of Tokyo
for the Degree of Doctor of Science
(Hakase (Kagaku))**

Yuichiro Shiozawa

March 2016

Acknowledgements

First of all, I would like to express my deepest gratitude to Professor Jun Yoshinobu. He supervised me during my master and doctor program, and taught the fundament for research in the field of physical chemistry, especially the surface science. His supervisions, encouragements, and supports were invaluable to this thesis.

I sincerely say my gratitude to Dr. Shinya Yoshimoto and Mr. Kozo Mukai for their fruitful discussions and a lot of advises. They also gave me a lot of instructions, encouragements, and supports. I also express my gratitude to Dr. Takanori Koitaya. I was guided by him during my master and doctor program, and was gave a lot of instructions and encouragements. I have interested in methanol synthesis reaction in the period with him. I am grateful to Professor Junji Nakamura (Tsukuba University) and Professor Yoshitada Morikawa (Osaka University) for their valuable discussions. I am also grateful to the staff members of the Photon Factory BL-13 for their technical support.

Many thanks go to all the present members of Yoshinobu Laboratory, Dr. Jiayi Tang, Mr. Yuki Yoshikura, Mr. Ryosuke Miyahara, Mr. Masahiro Hasegawa, and Mr. Hiroaki Ueda.

I would like to thank the previous members of Yoshinobu laboratory, Dr. Yosuke Harada, Dr. Sumera Shimizu, Dr. Enju Sakai, Mr. Hiroyuki Noritake, Mr. Kazutaka Fujimaki, Mr. Hirokazu Kikuchi, and Mr. Mamoru Fukasawa.

Many thanks go to the colleagues in Surface Science group of The Institute for Solid State Physics (ISSP); Professor Fumio Komori, Professor Yukio Hasegawa; and all the members of their laboratories.

A special thanks goes to the secretaries of Division of Nanoscale Science, Ms. Natsumi Ishibashi, Ms. Michiko Komaki, and Ms. Junko Kawamura.

I would like to acknowledge the financial support from the Advanced Catalytic Transformation program for Carbon utilization (ACT-C) of the Japan Science and Technology Agency (JST), and ISSP and Graduate School of Frontier Sciences for my employment as a research assistant.

Finally, I wish to express my gratitude to my family for their many supports.

Yuichiro Shiozawa, Kashiwa, January, 2017

Contents

Chapter 1.....	1
1.1 General Introduction.....	1
1.2 Aim of this Thesis	7
Chapter 2.....	9
2.1 Instruments for IRAS	9
2.2 Instruments for XPS	13
2.2.1 Instruments for laboratory XPS	13
2.2.2 Instruments for high-resolution XPS using synchrotron radiation.....	15
2.3 Sample preparation	18
2.4 Deposition of zinc.....	20
Chapter 3.....	22
3.1 Infrared reflection absorption spectroscopy.....	22
3.2 X-ray photoelectron spectroscopy.....	27
3.3 Temperature programmed desorption	29
Chapter 4.....	35
4.1 Introduction	36
4.2 Results and Discussion	39
4.2.1 The quantitative analysis of desorption kinetics parameter of HCOOH on Cu(111).....	39

4.2.2 The quantitative analysis of dissociation kinetics from HCOOH to monodentate formate on Cu(111).....	48
4.3 Conclusions.....	63
Chapter 5.....	64
5.1 Introduction	65
5.2 Results and Discussion	67
5.3 Conclusions.....	110
Chapter 6.....	111
6.1 Concluding remarks	111
6.2 Future perspective.....	114
References	116
List of Figures.....	122
List of Tables	126
List of Publications.....	127
Papers included in this thesis:.....	127
Papers to which I have contributed but which are not included in this thesis:	127

Chapter 1

Introduction

1.1 General Introduction

In recent years, methanol (CH_3OH) is of interest as a component of future hydrogen energy system, because methanol is the most useful chemicals to produce hydrogen molecules.¹ On the other hand, the synthesis of methanol from CO_2 and H_2 ($\text{CO}_2 + 3\text{H}_2 \rightarrow \text{CH}_3\text{OH} + \text{H}_2\text{O}$) is an important process, and Cu/ZnO catalyst is generally used for this reaction. The methanol synthesis reaction is an essential topic in the efficient use of CO_2 as a chemical feedstock.²

The hydrogenation of CO and CO_2 on metal catalysts have been studied by means of many experimental^{3–33} and theoretical^{34–36} methods. Copper based catalysts have been used for the research of CO_2 hydrogenation.^{7,8,10,12,13,19–33} Figure 1.1 shows the reaction network of simultaneous the methanol synthesis and water gas shift ($\text{CO} + \text{H}_2\text{O} \rightarrow \text{CO}_2 + \text{H}_2$) reaction over Cu catalysts based on theoretical study.³⁵ The conversion process from CO_2 to methanol is explained

as follows. First, a gaseous CO_2 molecule adsorbs on the surface as shown a process of R1.³⁵ The adsorbed CO_2 molecule reacts with a hydrogen atom to form a bidentate formate (HCOO) (R17).³⁵ When an oxygen atom of the bidentate formate is detached from the surface and is bound with a hydrogen atom, adsorbed formic acid (HCOOH) molecule is formed on the surface (R19).³⁵ There is a process that the adsorbed formic acid desorbs molecularly from the surface as a gaseous formic acid (R5).³⁵ When a carbon atom of the adsorbed formic acid molecule is hydrogenated by a hydrogen atom, a (H_2CO)OH is formed on the surface (R20).³⁵ The adsorbed (H_2CO)OH is dissociated into an adsorbed formaldehyde (CH_2O) molecule and a hydroxyl group (OH) (R23).³⁵ The adsorbed formaldehyde molecule desorbs molecularly or is hydrogenated by a hydrogen atom to form a methoxy (CH_3O) on the surface (R24).³⁵ An oxygen atom of the methoxy is hydrogenated by a hydrogen atom to form a methanol (R25, R45) on the surface.³⁵ Finally, adsorbed methanol desorbs from the surface as gaseous methanol (R7).³⁵ The previous theoretical studies provide important information for the elementary processes of methanol synthesis reaction, which contribute to the assignment of reaction intermediates in the experimental studies.

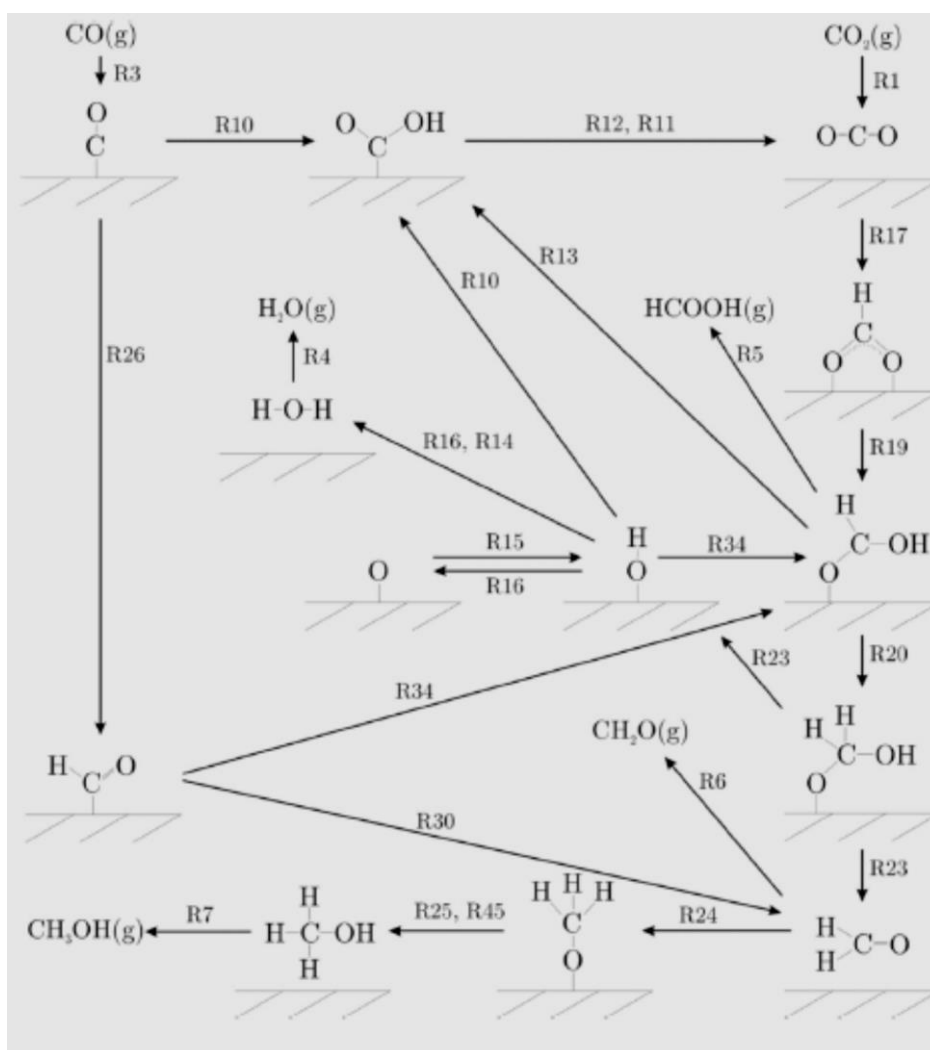


Figure 1.1. Reaction network of simultaneous the methanol synthesis and water gas shift reaction ($\text{CO} + \text{H}_2\text{O} \rightarrow \text{CO}_2 + \text{H}_2$) reaction over Cu catalysts.³⁵

On the other hand, Figure 1.2 shows the reaction network in both methanol synthesis and reverse water gas shift reaction ($\text{CO}_2 + \text{H}_2 \rightarrow \text{CO} + \text{H}_2\text{O}$) involving the possible intermediates on copper catalysts, as proposed in the previous experimental studies.^{7,8,10,12,13,19-33} As shown in Fig 1.2, adsorbed

formate and methoxy species could be stable intermediates for methanol synthesis reaction.^{20–33} However, despite many experimental studies, the elementary processes for intermediates of labeled “A” and “B” are still in the middle of being discussed.¹⁹ In addition, the possibility of interconversion of labeled “B” with formate species is indicated in Fig 1.2. The role of formate species in the reverse water gas shift reaction is still uncertain.¹⁹

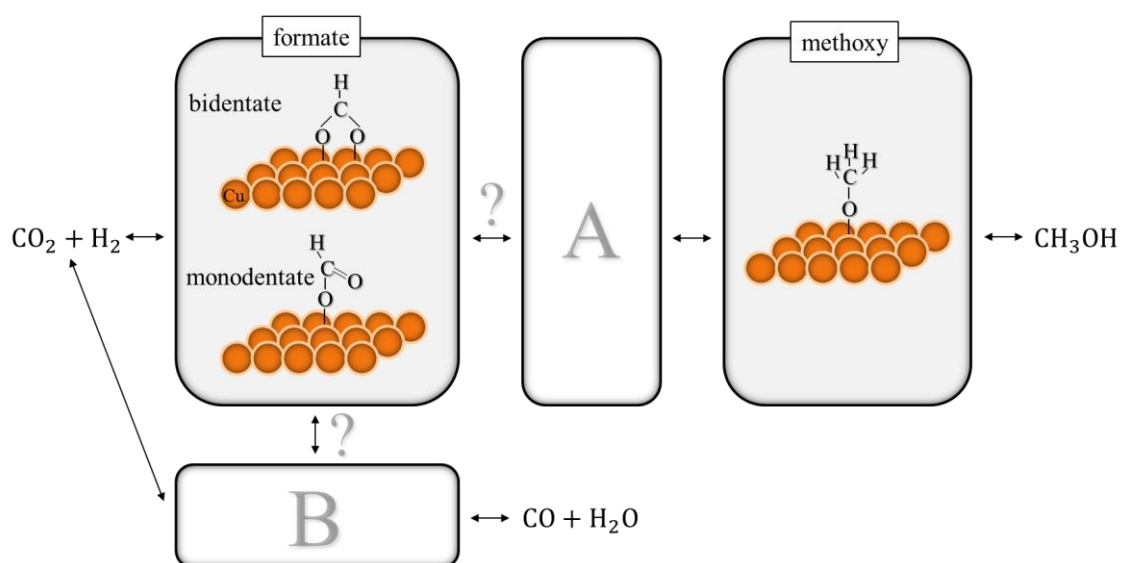


Figure 1.2. Reaction network both methanol synthesis and reverse water gas shift on copper.^{7,8,10,12,13,19–33}

The catalytic decomposition of formic acid (HCOOH) adsorbed on copper surfaces has been studied over the several decades.^{37–45} The decomposition of formic acid is of great importance, because the formate species is one of the stable intermediate species in the methanol synthesis reaction.⁴⁶ Formic acid decomposition has been studied on single crystal Cu(110)^{37–40,42} and Cu(100)⁴¹ and Cu(111)^{43–45} surfaces. Figure 1.3 shows a reaction scheme from formic acid to formate species on a Cu surface. The formic acid adsorbed on Cu(110) at 85 K was dissociated into a monodentate formate and a hydrogen atom at 200 K.³⁸ The monodentate formate was converted to the bidentate formate with further heating; this change begins at 200 K and is completed at about 300 K.³⁸ The dissociated hydrogen atoms were desorbed as H₂ at 273 K.⁴² The bidentate formate was decomposed and immediately desorbed as H₂ and CO₂ at 473 K (reaction-limited desorption).⁴²

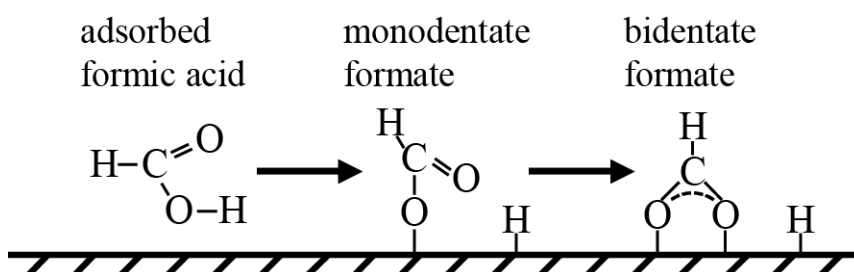


Figure 1.3. Reaction scheme from formic acid to formate species on a Cu surface.

As described above, the decomposition of formic acid is related to the elementary processes of the methanol synthesis reaction, meaning it is important to elucidate how formic acid molecules adsorb and dissociate into formate species on the Cu surfaces at a molecular level. The present thesis aims to understand the microscopic behavior and reaction of formic acid on copper model catalysts using modern surface spectroscopies.

1.2 Aim of this Thesis

The decomposition of formic acid on Cu(111) was first reported in 2013,⁴³ and only three studies have been reported on Cu(111) so far.^{43–45} The previous studies show that HCOOH adsorbed on Cu(111) forms polymeric structures via the hydrogen bonding network at low temperature; the annealing of this system induces into formate species.^{43–45} The previous studies have shed light on the qualitative knowledge of the decomposition reaction of formic acid on Cu surfaces.^{43,45} However, quantitative analysis of the reaction kinetics of formic acid adsorbed on Cu surfaces has not been reported. In order to understand the reaction kinetics of formic acid on Cu surfaces, the activation energies of each elementary process must be estimated.

On the other hand, there have been no reports on the decomposition of formic acid on well-defined Cu step and Zn-Cu alloyed surface. In recent years, the step surfaces have attracted much attention because unique catalytic reactions may occur at the step sites.^{18,47–50} Formic acid decomposition is the useful reaction in order to understand the adsorption and decomposition of the formate species on the Zn-Cu alloyed surface.

First, I investigate the desorption and decomposition kinetics of formic acid on Cu(111) using TPD, XPS and TR-IRAS. Based on these measurements, I estimated the activation energies for desorption of formic acid and for dissociation from formic acid into monodentate formate species. The adsorption states and dissociation process at a submonolayer coverage are discussed in detail. By comparing the previous theoretical studies on Cu(111) quantitatively, I demonstrate that the hydrogen bonding network stabilizes the adsorption of HCOOH and monodentate formate species.

Secondly, I investigate the decomposition reaction of formic acid on Zn-Cu(111) and Zn-Cu(997) as well as clean Cu(111) and Cu(997) using XPS, TPD and IRAS. I chose the Cu(997) surfaces in order to elucidate the adsorption and reaction of formic acid at step site. Based on these measurements, the adsorption states and dissociation process of formic acid adsorbed on Cu(997) and Zn-Cu(997) are discussed in detail. I demonstrate that the adsorption energy of monodentate formate species is stabilized at step sites and which lead to decrease the activation barrier between formic acid and monodentate formate species. I also demonstrate that the Zn atoms play a vital role in the stabilization of formate species on the Zn-Cu alloyed surface.

Chapter 2

Experimental

In the present study, the adsorption and dissociation of formic acid (HCOOH and DCOOH) on the Cu and Zn-Cu alloyed surfaces were studied using infrared reflection absorption spectroscopy (IRAS), X-ray photoelectron spectroscopy (XPS) and temperature programmed desorption (TPD). The experimental apparatus, sample preparation, and experimental procedure are described in this chapter.

2.1 Instruments for IRAS

The schematic illustration of IRAS system is shown in Figure 2.1. This system is equipped with a Fourier transform infrared spectrometer (Bruker, IFS66v/S), a quadrupole mass spectrometer (Balzers, Prisma QMS 200), a Spot-Profile-Analysis low energy electron diffraction apparatus (OMICRON, SPA-LEED), an ion source (SPECS, IQE 11/35) and a home-build evaporation source⁵¹. The experiments were conducted in UHV with a base pressure of

$<2 \times 10^{-10}$ Torr. The sample was cooled to 80 K by liquid nitrogen with a heat shield (Advanced Research Systems, Helitran LT-3B). The sample was heated by electron bombardment with a tungsten (W) filament. HCOOH (Wako Chemicals, >98.0% purity) and DCOOH (TCI, >99 atom%D purity) were dried over copper sulfate anhydride and further purified by several freeze-pump-thaw cycles. Gaseous molecules were introduced onto the sample surface using a pulse gas dosing system by a pulse valve (Parker Hannifin, Series 9).

IRAS measurements were performed using a Fourier transform infrared spectrometer with a mercury-cadmium-telluride (MCT) detector. The MCT detector is an intrinsic photoconductive detector operating at liquid nitrogen temperature and with a measurable wavenumber region of 7500-800 cm^{-1} . The IR beam is focused onto the sample in an UHV chamber, such that the incident/reflected angle is 84° with respect to the surface normal.⁵² IRAS spectra were obtained with 8 or 4 cm^{-1} resolution.

TPD measurements were performed using a quadrupole mass spectrometer (Balzers, Prisma QMS 200) by detecting molecular ion (M^+) signals of desorbed species. The sample was heated by a W filament at a constant ramp rate used

by a home-build proportional-integral-differential (PID) controller. The sample temperature measured by a K-type thermocouple was calibrated based on the TPD spectra of CO and H₂O from the Cu surfaces.^{53,54} The sample was heated at a heating rate of 1 K/s.

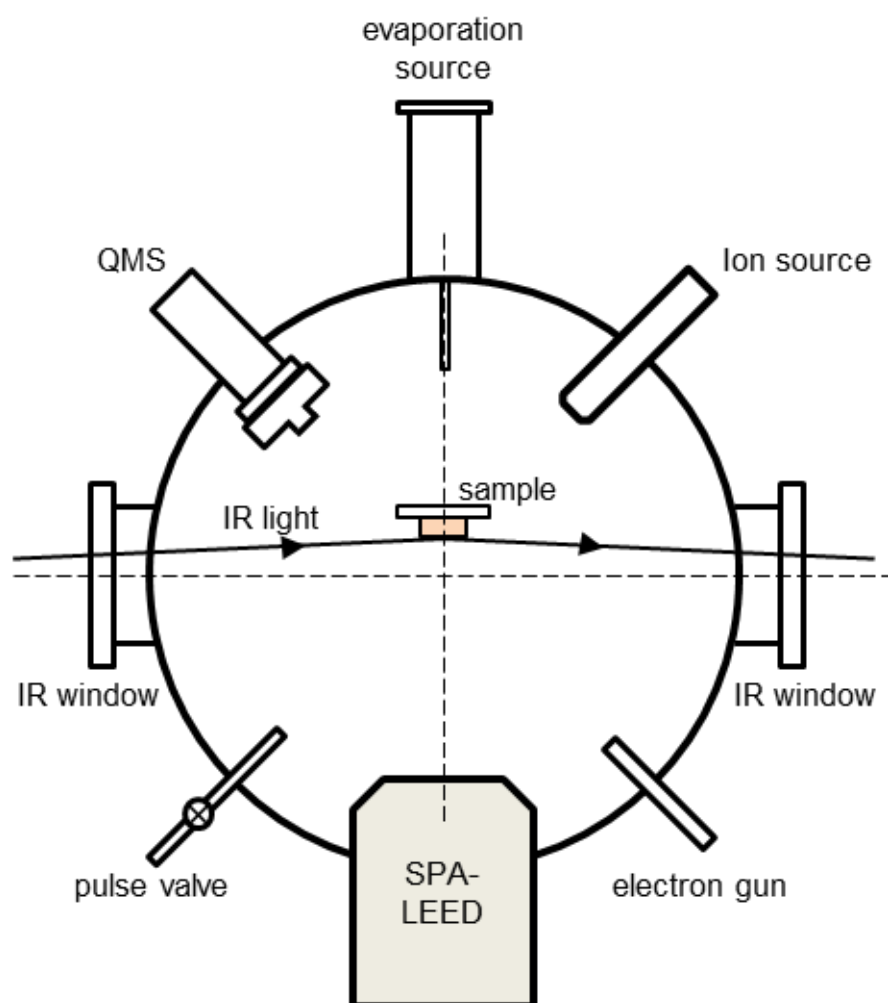


Figure 2.1. Schematic diagram of IRAS chamber (top view).

2.2 Instruments for XPS

2.2.1 Instruments for laboratory XPS

The schematic illustration of laboratory XPS system is shown in Figure 2.2. The laboratory XPS system is equipped with a hemispherical electron energy analyzer (SCIENTA, R3000), a quadrupole mass spectrometer (Balzers, Prisma QMS 200), a low energy electron diffraction (OCI, LEED), an ion source (SPECS, IQE 11/35) and a home-build evaporation source⁵¹. The experiments were conducted in an UHV chamber with a base pressure of $<2 \times 10^{-10}$ Torr. XPS measurements were carried out with an Al K_{α} X-ray source (VG, Microtech 8025) at a normal emission condition. The sample was cooled to 80 K by liquid nitrogen with a heat shield (Advanced Research Systems, Helitran LT-3B). The sample was heated by electron bombardment with a tungsten (W) filament. Gaseous molecules were introduced onto the sample surface using a pulse gas dosing system by a pulse valve (Parker Hannifin, Series 9).

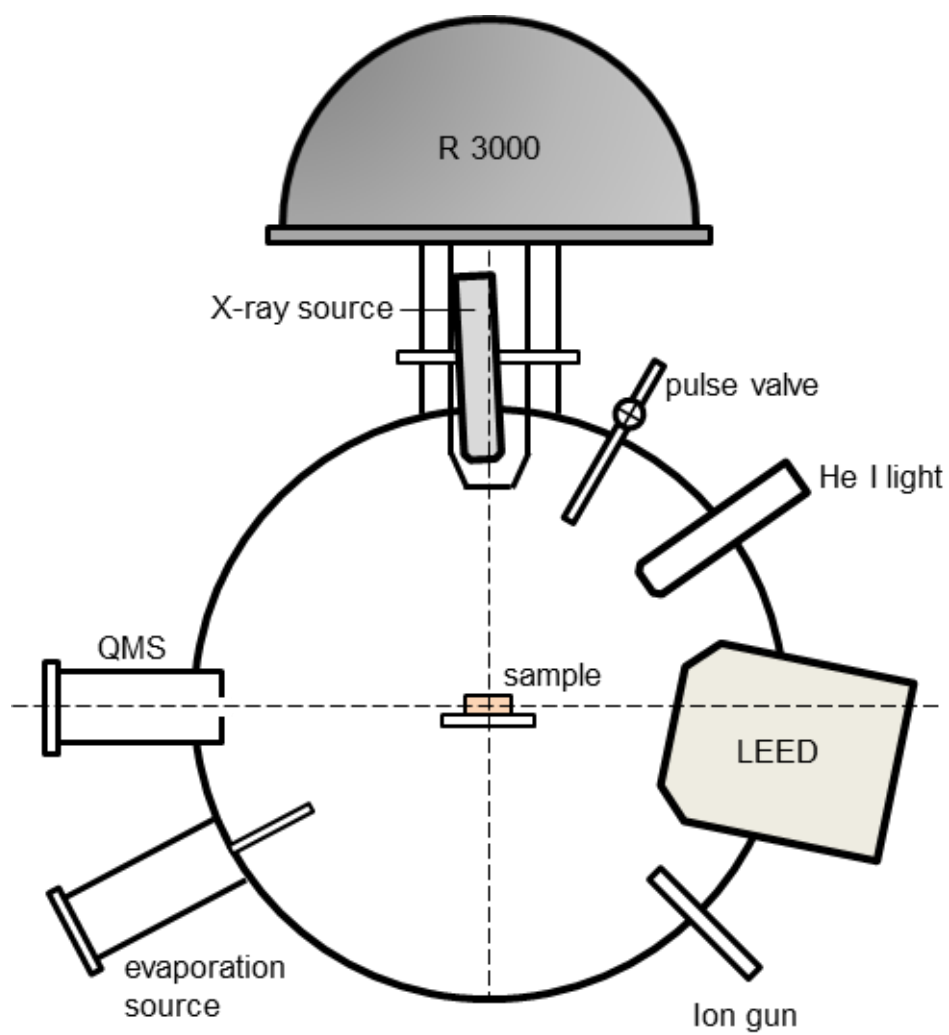


Figure 2.2. Schematic diagram of laboratory XPS chamber (top view).

2.2.2 Instruments for high-resolution XPS using synchrotron radiation

The schematic illustration of high-resolution XPS system is shown in Figure 2.3. The instruments are introduced at BL-13B of the synchrotron light source Photon Factory, KEK, Japan (PAC=2012-S2-006). This system equipped with a hemispherical electron energy analyzer (SPECS, Phoibos 100), a quadrupole mass spectrometer (Balzers, Prisma QMS 200), a low energy electron diffraction (Varian, LEED), an ion source (SPECS, IQE 11/35) and a home-build evaporation source⁵¹. The experiments were conducted in an UHV chamber with a base pressure of $<2 \times 10^{-10}$ Torr. The sample was cooled to 80 K by liquid nitrogen with a heat shield (Advanced Research Systems, Helitran LT-3B). The sample was heated by electron bombardment with a tungsten (W) filament. Gaseous molecules were introduced onto the sample surface using a pulse gas dosing system by a pulse valve (Parker Hannifin, Series 9). The C 1s and O 1s XPS spectra were measured using a photon energy of 630 eV. The zero binding energy was taken at the Fermi edge of Cu. All XPS measurements were carried out with a normal emission condition.

The theoretical energy resolution of XPS spectra (ΔE) can be estimated as follows. The energy resolution of a hemispherical electron energy analyzer (ΔE_1) is calculated by

$$\Delta E_1 = \frac{E_p S}{2R} \quad (2.1)$$

Here, S is the slit width (6 mm), R is the analyzer mean radius (100 mm), and E_p is the pass energy, which is determined by the electrostatic field between the inner and outer sphere. In this study, the energy resolution of the synchrotron light (ΔE_2) is calculated by⁵⁵

$$E/\Delta E_2 \approx 3000 \quad (2.2)$$

Therefore the total energy resolution of XPS spectra (ΔE) is estimated by

$$\Delta E = \sqrt{(\Delta E_1)^2 + (\Delta E_2)^2} \quad (2.3)$$

The total energy resolution of XPS spectra (ΔE) of a photon energy of 630 eV ($E_p = 6$ eV) is estimated to be 280 meV.

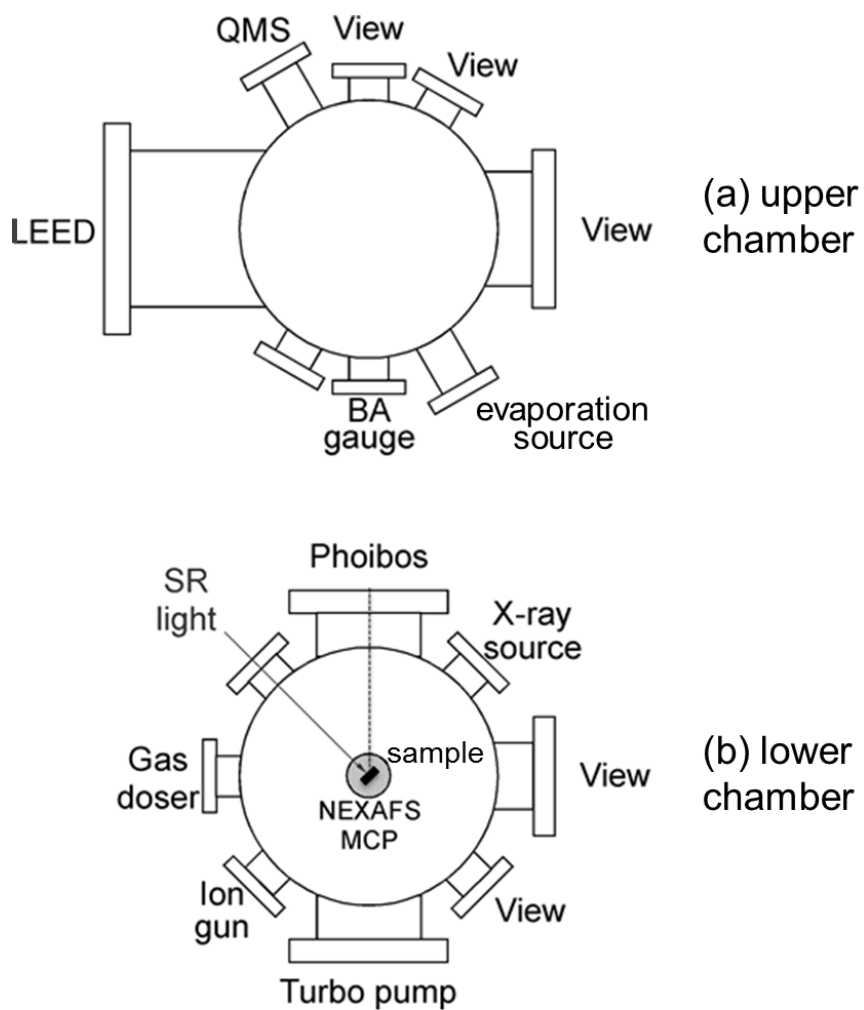


Figure 2.3. Schematic diagram of high-resolution XPS chamber (top view). (a) upper and (b) lower chamber.

2.3 Sample preparation

Figure 2.4 shows photographs of single crystals of (a) Cu(111) and (b) Cu(997) (SPL, 99.9999% purity) mounted by sample holder used in the IRAS and XPS chambers. Figure 2.5 shows a schematic model of the ideal Cu(997) surface without defects.⁵⁶ The Cu(997) surface has a close-packed terrace consists of nine atomic rows, and each terrace is separated by a monoatomic (111) step. The clean Cu(111) and Cu(997) surfaces were prepared by several cycles of Ne ion sputtering, and annealing at 650-700 K for 120 s. The well-defined clean Cu(111) surface was confirmed by LEED observation of the Cu(111) surface, XPS and TPD spectra of CO on Cu(111).⁵³ The well-defined clean Cu(997) surface was confirmed by LEED observation of the Cu(997) surface⁵⁶, XPS and IRAS spectra of CO on Cu(997).

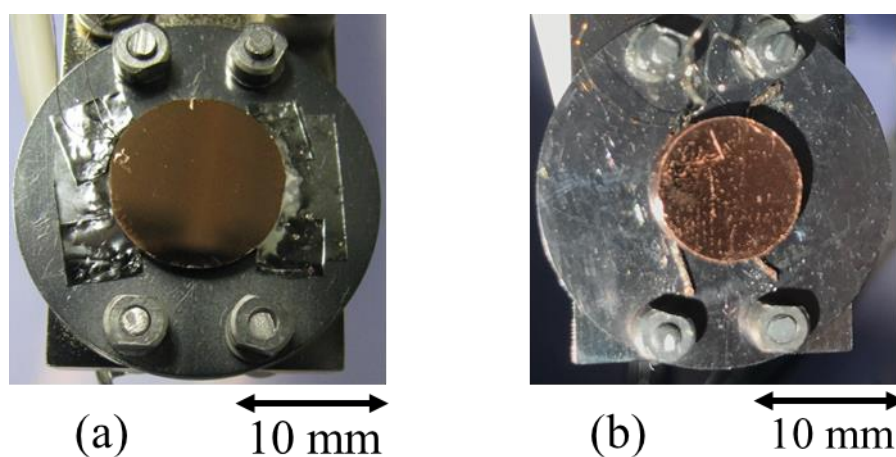


Figure 2.4. Photographs of single crystal of (a) Cu(111) and (b) Cu(997) mounted by sample holder used in IRAS and XPS chambers.

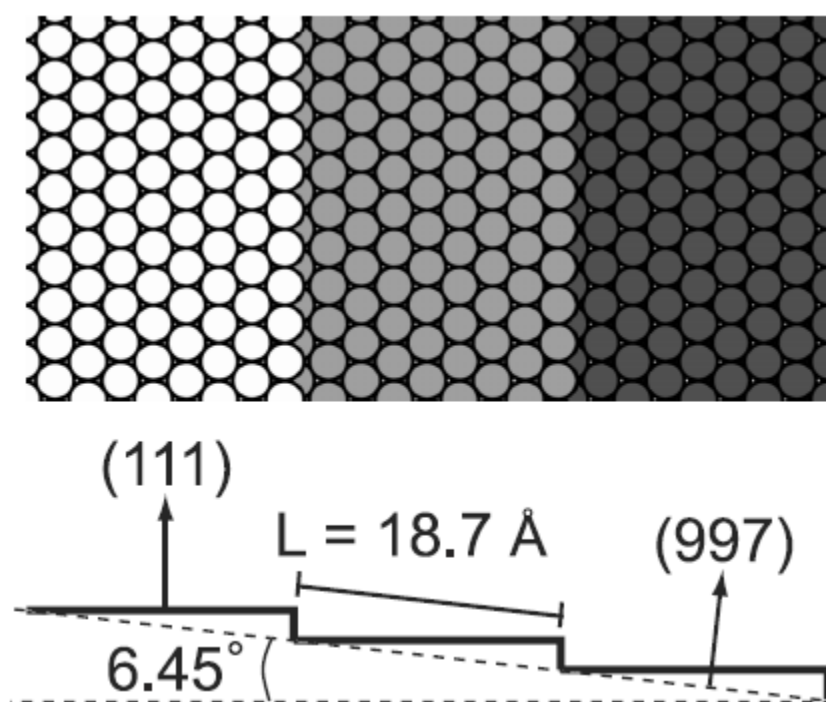


Figure 2.5. A schematic model of the ideal Cu(997) surface.⁵⁶

2.4 Deposition of zinc

We prepared Zn-Cu alloyed surfaces for the experiments discussed in chapter 5. Figure 2.6 shows a photograph of the Zn deposition in an UHV chamber. The home-build miniature effusion cell was used for the deposition of Zn.⁵¹ The Zn was vapor-deposited onto the Cu surfaces at 300 K by radiation heating a zinc wire (The Nilaco Corporation, 99.999% purity) in a quartz glass tube. The temperature of a quartz glass tube was monitored by a K-type thermocouple inserted in the tube. The rate of vapor-deposited was monitored by a quartz microbalance in another UHV system. After deposition of Zn, the sample was annealed at 470-475 K for 60 s to form Zn-Cu alloy.⁵⁷ The coverages of Zn were estimated by the peak area ratios of Zn 2p_{3/2}/Cu 2p_{3/2} at a photon energy of 1486.6 and 1100 eV.⁵⁸ The number of surface Cu atoms was defined as 1 ML.

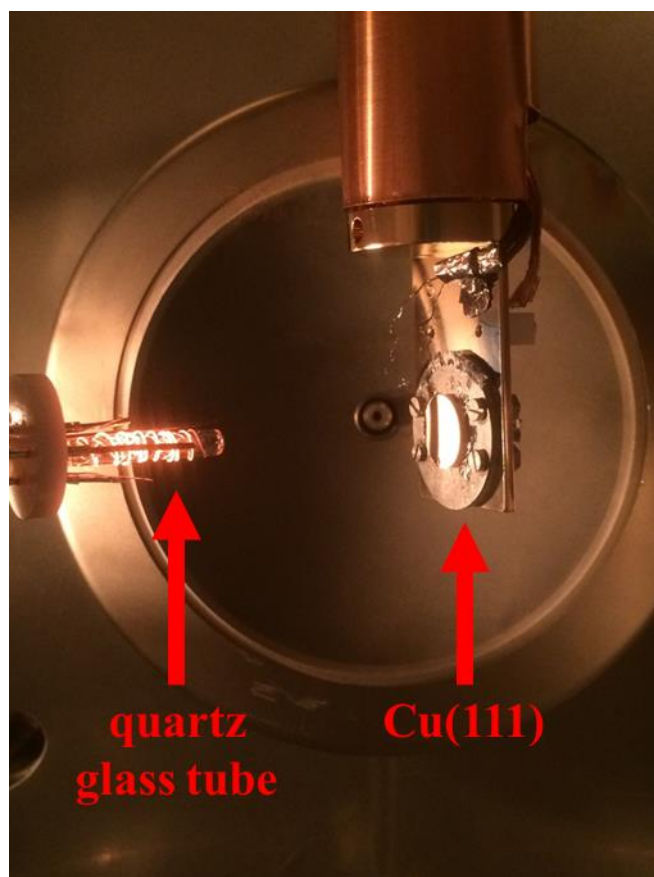


Figure 2.6. A photograph of the Zn deposition in an UHV chamber. The Zn is vapor-deposited onto the Cu(111) surface by radiation heating a zinc wire in a glass tube.

Chapter 3

Basic Principles

In the present study, the adsorption and dissociation of formic acid (HCOOH and DCOOH) on the Cu and Zn-Cu alloyed surfaces were studied using infrared reflection absorption spectroscopy (IRAS), X-ray photoelectron spectroscopy (XPS) and temperature programmed desorption (TPD). IRAS is used to probe the vibrational properties of adsorbed species. XPS probes the amounts and electronic state of the adsorbed species. TPD provides information of adsorbed species on the surfaces by detecting molecular ion signals of desorbed species. In chapter 3, the basic principles of the IRAS, XPS and TPD method are summarized.

3.1 Infrared reflection absorption spectroscopy^{59–61}

Infrared reflection absorption spectroscopy (IRAS) is one of the methods that can measure the vibration states of adsorbed species on the surface or interface. By analyzing the IRAS spectra, we can obtain information for the orientation of adsorbed species and the reactions on metal surfaces.

The principle of IRAS is explained as follows. The metal surface has high reflectance with grazing incidence angle for infrared light. The reflected infrared light can be obtained almost the same intensity as incident light. This reflected infrared light interferes with the incident light to form a standing wave on the metal surface. Therefore, the infrared absorption intensity is not proportional to the intensity of incident light but to the electric field strength of this standing wave. In Figure 3.1, the incident angle of infrared light is defined as Φ (the angle from the surface normal). The incident infrared light, the reflected infrared light and the Z axis are located in the same plane (incident plane), respectively. The incident infrared light can be divided into two components which are parallel (P-polarized light: \mathbf{E}_P^i) and perpendicular (S-polarized light: \mathbf{E}_S^i) to the incident plane. When the complex index of refraction for the metal is $\tilde{n} = n + ik$; in generally, $n^2 + k^2 \gg 1$ is established in the infrared region. By using Fresnel's equation, the following equations are obtained for reflected infrared light:

$$R_P = \frac{(n - \sec\phi)^2 + k^2}{(n + \sec\phi)^2 + k^2} \quad : \text{reflected light intensity of P polarized light} \quad (3.1)$$

$$R_S = \frac{(n - \cos\phi)^2 + k^2}{(n + \cos\phi)^2 + k^2} \quad : \text{reflected light intensity of S polarized light} \quad (3.2)$$

$$\tan\Delta = \tan(\delta_P - \delta_S) = \frac{2k \tan\phi \sin\phi}{\tan^2\phi - (n^2 + k^2)} \quad (3.3)$$

Here, $\Delta = \delta_P - \delta_S$ is the phase shift of the P- and S-polarized light by reflection.

The R_P and R_S indicate the reflected infrared light intensities of P- and S-polarized light, respectively. As shown in Figure 3.2, the S-polarized infrared light has only components parallel to the surface, and a phase shift of $-\pi$ occurs at all incident angles. This indicates that the electric field strength of S-polarized infrared light should become zero at the metal surface.

On the other hand, for the P-polarized infrared incidence, a phase shift occurs from 0 (normal incidence) to $-\pi$ (grazing incidence) as shown in Figure 3.3. The electric field formed by normal incidence always becomes weak because the electric field vectors of incident light and reflected light are reversed. However, when the P-polarized infrared light is incident at a large incident angle, a strong electric field is formed in the vertical direction of the metal surface. This effect can induce strongly the vibration in the surface perpendicular direction of adsorbed species.

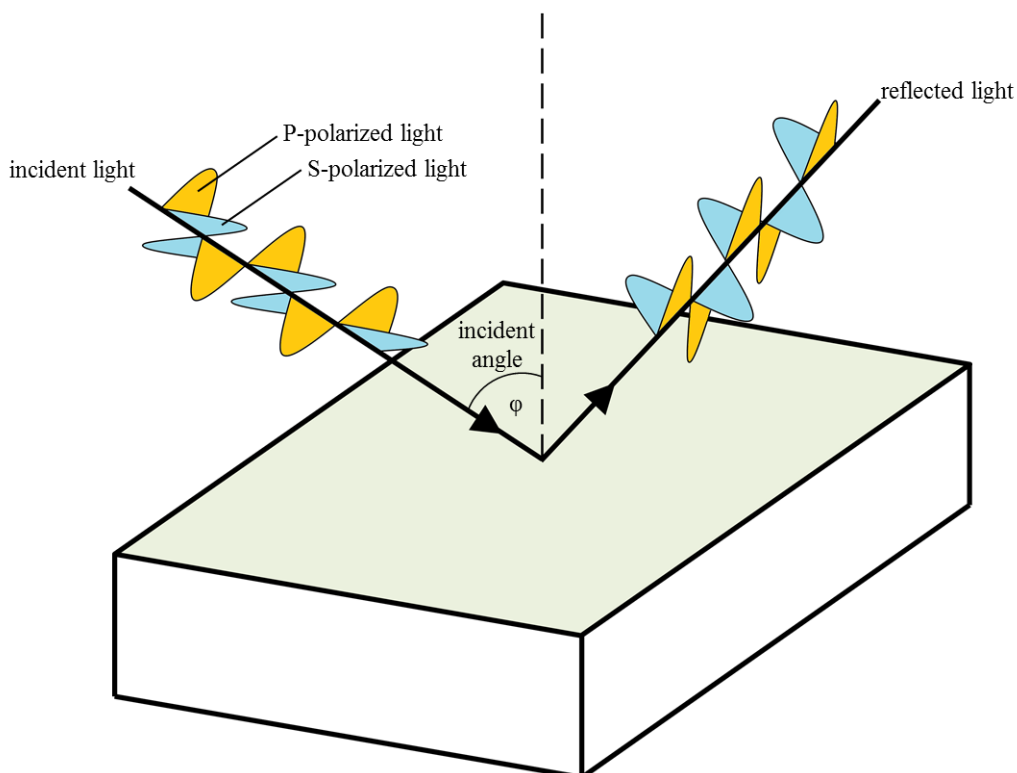


Figure 3.1. Infrared light entering and reflecting on the metal surface (including P-polarized light and S-polarized light).

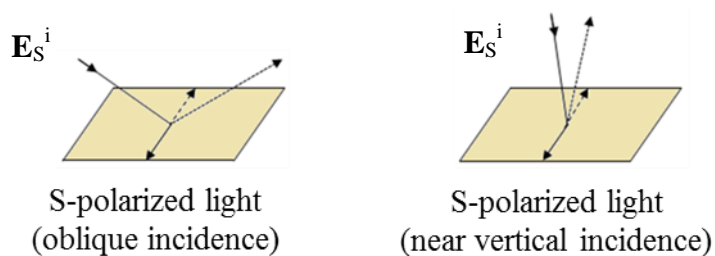


Figure 3.2. Phase shift when S-polarized light is incident and reflected on the metal surface.

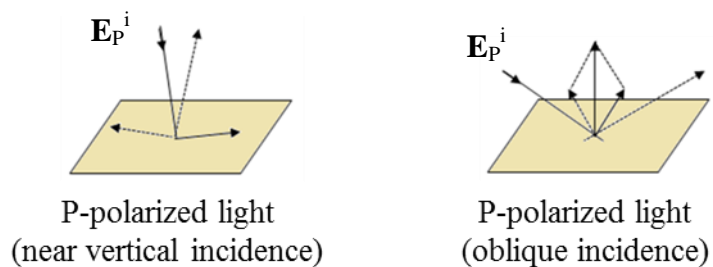


Figure 3.3. Phase shift when P-polarized light is incident and reflected on the metal surface.

When a molecule adsorbs on the metal surface, a mirror image corresponding to its orientation is formed in the metal. Figure 3.4 shows dynamic molecular and image dipoles when a molecule adsorbs its molecular plane parallel (left) or perpendicular (right) to the metal surface. The parallel component (Fig. 3.4, left) can form an image dipole oriented opposite to those of the molecule, which is screened by metal electrons. On the other hand, the perpendicular component (Fig. 3.4, right) has an image dipole in the same direction of the molecule, which can generate a dipole in the vertical direction of the metal surface. Thus, the vibration with dipole moments that changes parallel to the surface cannot be observed. This is called the surface vertical dipole selection rule.

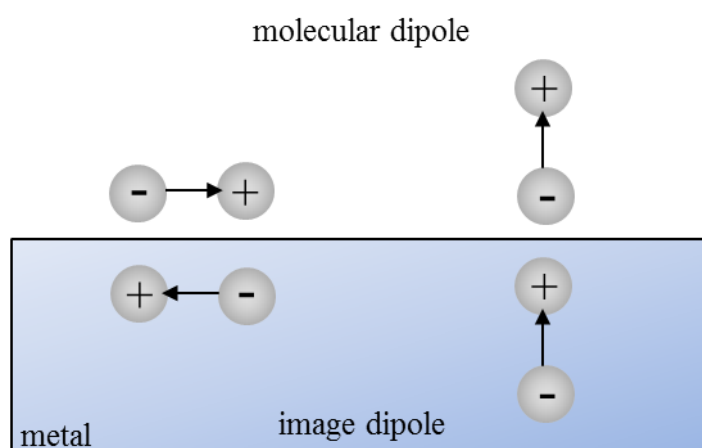


Figure 3.4. Dynamic molecular and image dipoles when a molecule adsorbs its molecular plane parallel (left) or perpendicular (right) to the metal surface.

3.2 X-ray photoelectron spectroscopy^{62,63}

Electronic information about the surface or inside of the sample is obtained in X-ray photoelectron spectroscopy (XPS). The principle of XPS is based on the description of Einstein's photoelectric effect. When light with the energy ($h\nu$) larger than the work function is incident onto the sample, electron emission from the surface can be induced. The work function (ϕ) is defined as the minimum energy required to remove electrons from the highest occupied energy level to the vacuum level. The vacuum level is the energy of electrons in vacuum removed away from adjacent particles (zero kinetic energy). The vacuum level can be used as zero energy.

In XPS, monochromatic X-rays are incident on the surface to emit the core level electrons. The energy of the X-ray ($h\nu$), the binding energy of the electron (E_B), the work function (ϕ), and the kinetic energy of the photoelectron (E_k) are defined, the following relationship holds.

$$E_k = h\nu - (E_B + \phi) \quad (3.4)$$

A part of the energy of the excitation light is consumed to exceed the binding energy barrier of the core level electrons ($E_B + \phi$), and the remaining energy is

converted into the kinetic energy of the emitted photoelectrons (E_k). When the kinetic energy of photoelectrons is measured with constant $h\nu$, the binding energy of electrons in the occupied state can be obtained. The core level electrons have a peculiar binding energy in each molecular orbital (e.g., the E_B of O 1s becomes larger than that of C 1s). By using this principle, we can perform element identification of the sample.

The binding energies of the core level electrons of atoms or molecules depend on the species to which it is bounded. This is because charge transfer occurs between the bound species. The charge transfer shifts the binding energy of the core level electrons to higher (or lower) by leaving a partial positive (or negative) charge on the atoms or molecules. This is understood by the increase (or decrease) in Coulomb interaction between the core level electrons and the nucleus. When the atom becomes more oxidized, the binding energy of the core level electrons increases. This is called chemical shift, and we can know the chemical bonding state of the atoms.

3.3 Temperature programmed desorption^{64–67}

Temperature programmed desorption (TPD) provide information of adsorbed species on the surface by detecting molecular ion signals of desorbed species.

The principle of TPD is explained as follows.

Adsorbed species can escape from the adsorption potential and desorb from the surface, when it exceeds the activation energy E_d for the desorption by heating. The desorption rate is described by Polanyi-Wigner equation.

$$r(\theta, T) = -\frac{d\theta}{dt} = \nu_d(\theta, T)\theta^{n(\theta)}\exp\left[\frac{-E_d(\theta)}{RT}\right] \quad (3.5)$$

Here, θ , T , ν_d , n and E_d are the coverage of adsorbed species, absolute temperature, pre-exponential factor for the desorption, desorption order and activation energy for the desorption, respectively. Figure 3.5 shows the simulated TPD spectra based on Polanyi-Wigner equation.

The zero order desorption is often observed when the atoms or molecules multilayers sublime from the surface, and the desorption rate does not depend on the coverage θ . The TPD spectra have an asymmetrical shape and the intensity rapidly decreases above the desorption peak maxima. In

addition, the desorption peak maxima is shifted to higher temperature side with increasing coverage θ .

The half order desorption is observed when the desorption occur at island edges on the surface. If molecular desorption occurs at the circular island edges, the number of adsorbed species at the island edge is proportional to the square root of coverage. Thus, the desorption kinetics could be a half order at submonolayer coverages.

The first order desorption is often observed in desorption of molecules adsorbed on the surface, and the desorption rate increases in proportion to the coverage θ . The TPD spectra show an asymmetric shape. When the temperature exceeds the desorption peak maxima, the intensity gradually decreases than the zero order desorption. The desorption peak maxima is constant regardless of the coverage θ .

The second order desorption is often observed when the adsorbed atoms are recombined and immediately desorbed, and the desorption rate is proportional to the square of the coverage θ . The TPD spectra show a symmetric

shape. The desorption peak maxima is shifted to lower temperature side with increasing coverage θ .

Applying the natural logarithm on both sides of the equation (3.5), the following equation is obtained.

$$\ln\left(-\frac{d\theta}{dt}\right) = (\ln v_d + n \ln \theta) + \frac{-E_d}{R} \times \frac{1}{T} \quad (3.6)$$

Here, $(\ln v_d + n \ln \theta)$ will never become constant because the pre-exponential factor v_d depends on the coverage θ . However, in the temperature region where the decrease of the coverage θ is small (the leading edge on the low temperature side of the desorption peak), $(\ln v_d + n \ln \theta)$ can safely assume a constant, and Arrhenius plot can be applied. This method is called threshold TPD (TTPD) method, which is enable to estimate the kinetic parameters of the desorption.⁶⁴⁻⁶⁷

Figure 3.6 show the demonstration of the TTPD method using the simulated TPD spectra. In Fig. 3.6 (a), blue line is the simulated TPD spectra based on Polanyi-Wigner equation. The desorption order, activation energy and pre-exponential factor for the desorption are assumed as zero, 20 kJ/mol and

$10^{-13} \text{ ML} \cdot \text{s}^{-1}$, respectively. In order to approximate the experimental conditions, a noise spectra in the TPD spectra is generated; green line is the noise spectra simulated by random sampling numbers of Gaussian distribution. Black line is the simulated TPD spectra added the noise spectra, which is applied the TTPD method to estimate the activation energy and pre-exponential factor for the desorption. In Fig. 3.6 (b), the desorption onsets and 9.57% threshold increments are indicated by arrows. Fig. 3.6 (c) shows an Arrhenius plot of the TPD spectra in Fig. 3.6 (b). The activation energy (E_d) and pre-exponential factor (ν_0 , zero order desorption) can be estimated by a fitted line in Fig. 3.6 (c). The activation energy and pre-exponential factor for desorption are independently estimated to be $20.85 \pm 2.62 \text{ kJ/mol}$ and $10^{13.60 \pm 1.92} \text{ ML} \cdot \text{s}^{-1}$, respectively. These estimated values are consistent with the simulated values ($E_d = 20 \text{ kJ/mol}$ and $\nu_0 = 10^{-13} \text{ ML} \cdot \text{s}^{-1}$) within the error ranges. Thus, the accuracy of the estimated value depends greatly on the signal-noise-to-ratio of the TPD spectra.

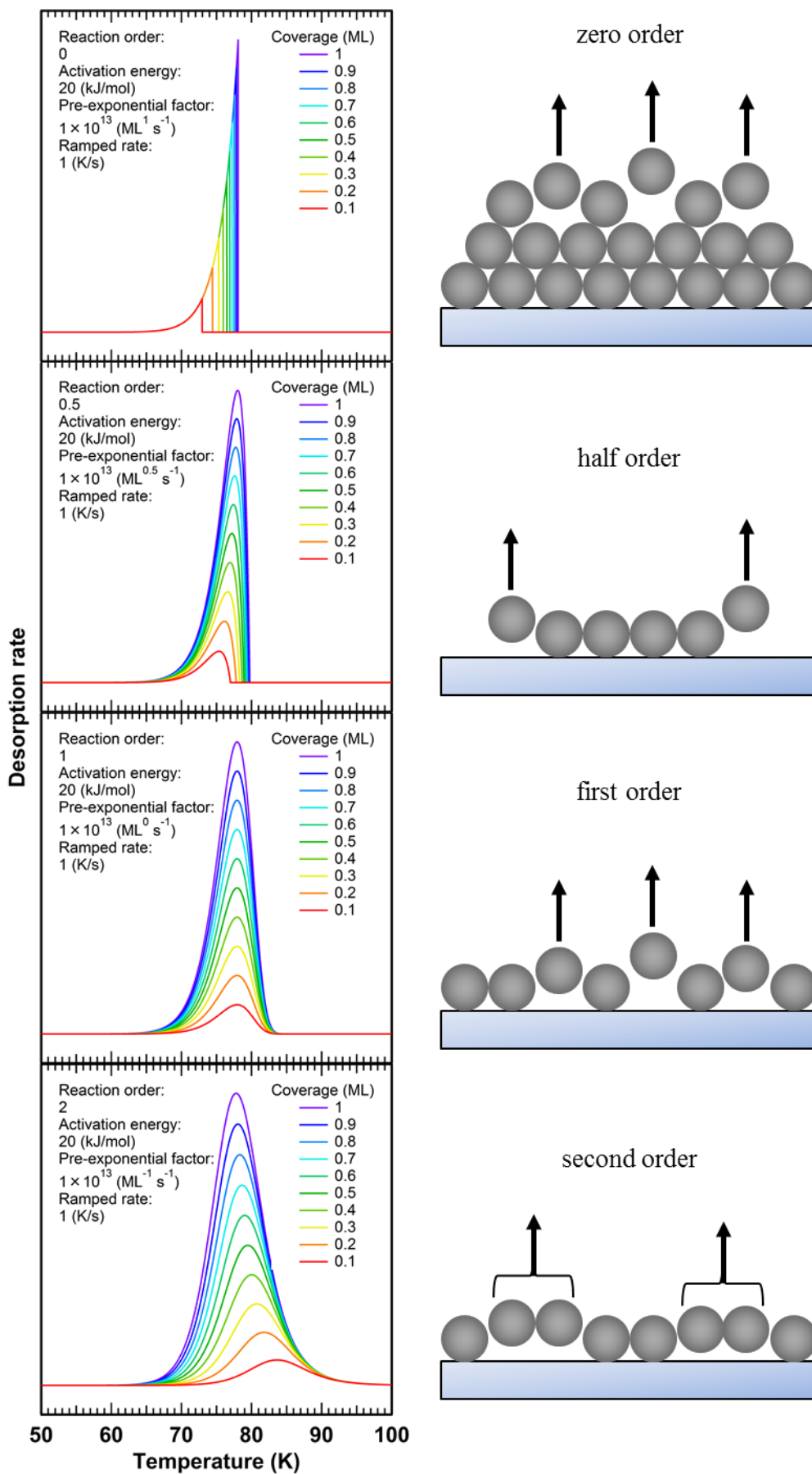


Figure 3.5. Simulated TPD spectra based on Polanyi-Wigner equation.

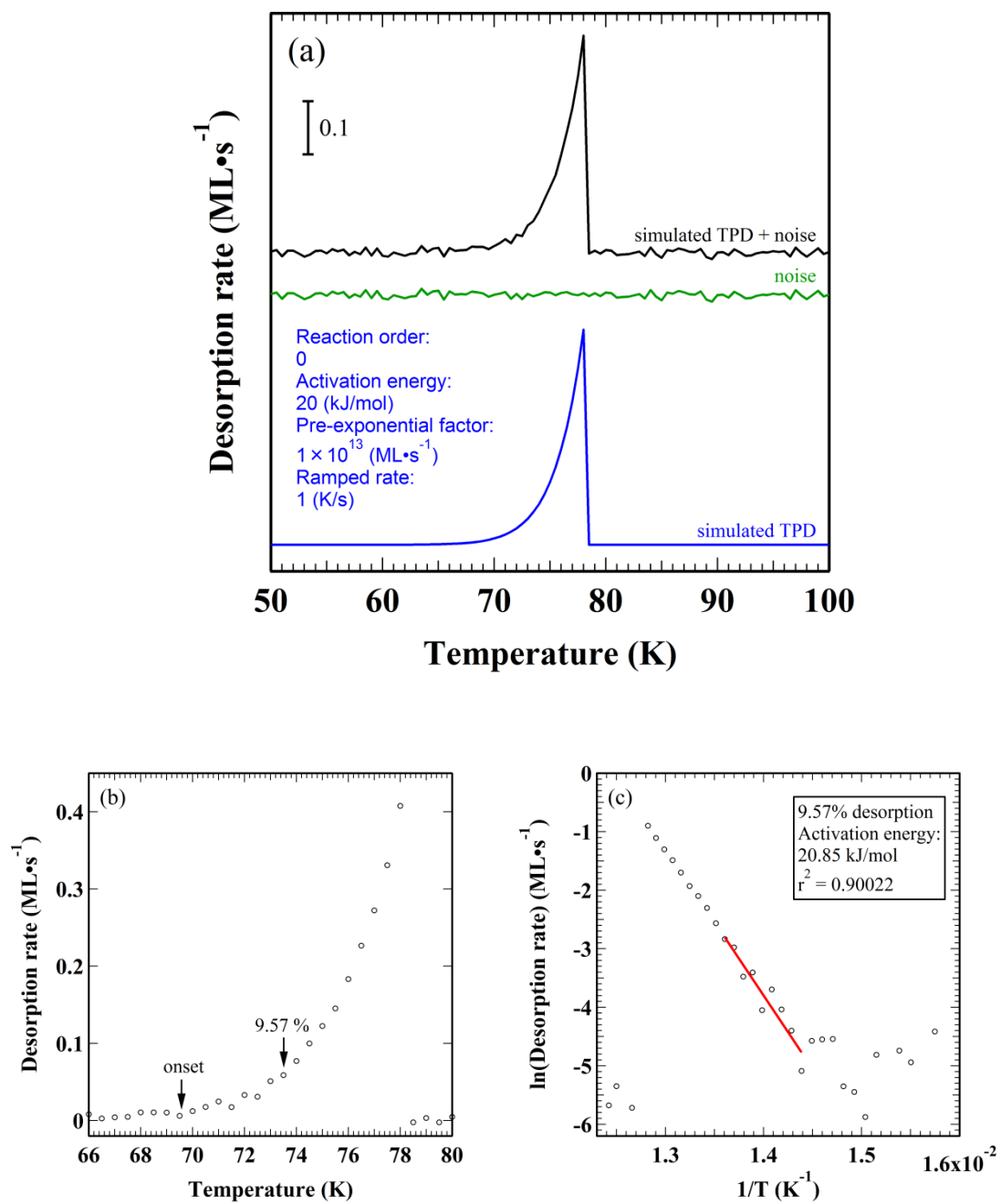


Figure 3.6. The demonstration of threshold TPD method using the simulated TPD spectra added the noise spectra.

Chapter 4

Quantitative analysis of desorption and decomposition kinetics of formic acid on Cu(111): the importance of hydrogen bonding between adsorbed species

Quantitative analysis of desorption and decomposition kinetics of formic acid (HCOOH) on Cu(111) were performed by temperature programmed desorption (TPD), X-ray photoelectron spectroscopy (XPS) and time-resolved infrared reflection absorption spectroscopy (TR-IRAS). The activation energy for desorption is estimated to be 53-75 kJ/mol by the threshold TPD (TTPD) method as a function of coverage. Vibrational spectra of the first layer HCOOH at 155.3 K indicate that adsorbed molecules form a polymeric structure via the hydrogen bonding network. Adsorbed HCOOH molecules are gradually dissociated into monodentate formate species. The activation energy for the dissociation into monodentate formate species is estimated to be 65.0 kJ/mol at a submonolayer coverage (0.26 molecules/surface Cu atom). The hydrogen bonding between adsorbed HCOOH species plays a vital role in the stabilization of HCOOH on Cu(111). The monodentate formate species are stabilized at higher coverages.

4.1 Introduction

Basic knowledge of adsorption states of formic acid is important for understanding its reaction kinetics on solid surfaces. Formic acid molecules sometimes form hydrogen bonding on metal surfaces, which induces the red shift of O-H stretching mode and the blue shift of O-H bending mode of formic acid.^{38,68-70} Baber *et al.* reported that the deprotonation of formic acid on Cu(111) can be induced by pre-adsorbing polymeric formic acid clusters at low temperatures; the annealing of this system at 175 K induces the dissociation of the acidic O-H bond of HCOOH adsorbed on the edges of the polymeric clusters.⁴³ The polymeric clusters were assigned to α -polymeric formic acid judging from the out-of-plane O-H bending mode in infrared reflection absorption spectroscopy (IRAS) spectra. On the other hand, Marcinkowski *et al.* reported that β -polymeric formic acid forms on Cu(111) at 85 K by using a high-resolution scanning tunneling microscopy (STM).⁴⁵ Figure 4.1 shows the adsorbed structures of formic acid based on α - and β -polymeric formic acid.⁷⁰ The adsorption structure of polymeric formic acid on Cu(111) at low temperature is not fully elucidated. A morphological change of the adsorbed formic acid may

originate from the experimental conditions such as the initial coverages of formic acid, sample temperature, surface structure etc.

The α - and β -polymeric formic acid are sometimes adsorbed with its molecular plane parallel to the surface.⁶⁸⁻⁷⁰ STM measurements show the α -polymeric formic acid species form islands even at submonolayer coverages.⁴³ These observations indicate that the hydrogen bonding network plays an important role in the island formation and the HCOOH dissociation on Cu(111).

In chapter 4, we report the desorption and decomposition kinetics of formic acid on Cu(111) using TPD, XPS and TR-IRAS. Based on these measurements, we estimated the activation energies for desorption of formic acid and for dissociation from formic acid into monodentate formate species. The adsorption states and dissociation process at a submonolayer coverage are discussed in detail. By comparing the previous theoretical studies on Cu(111) quantitatively, we demonstrate that the hydrogen bonding network stabilizes the adsorption of HCOOH and monodentate formate species.

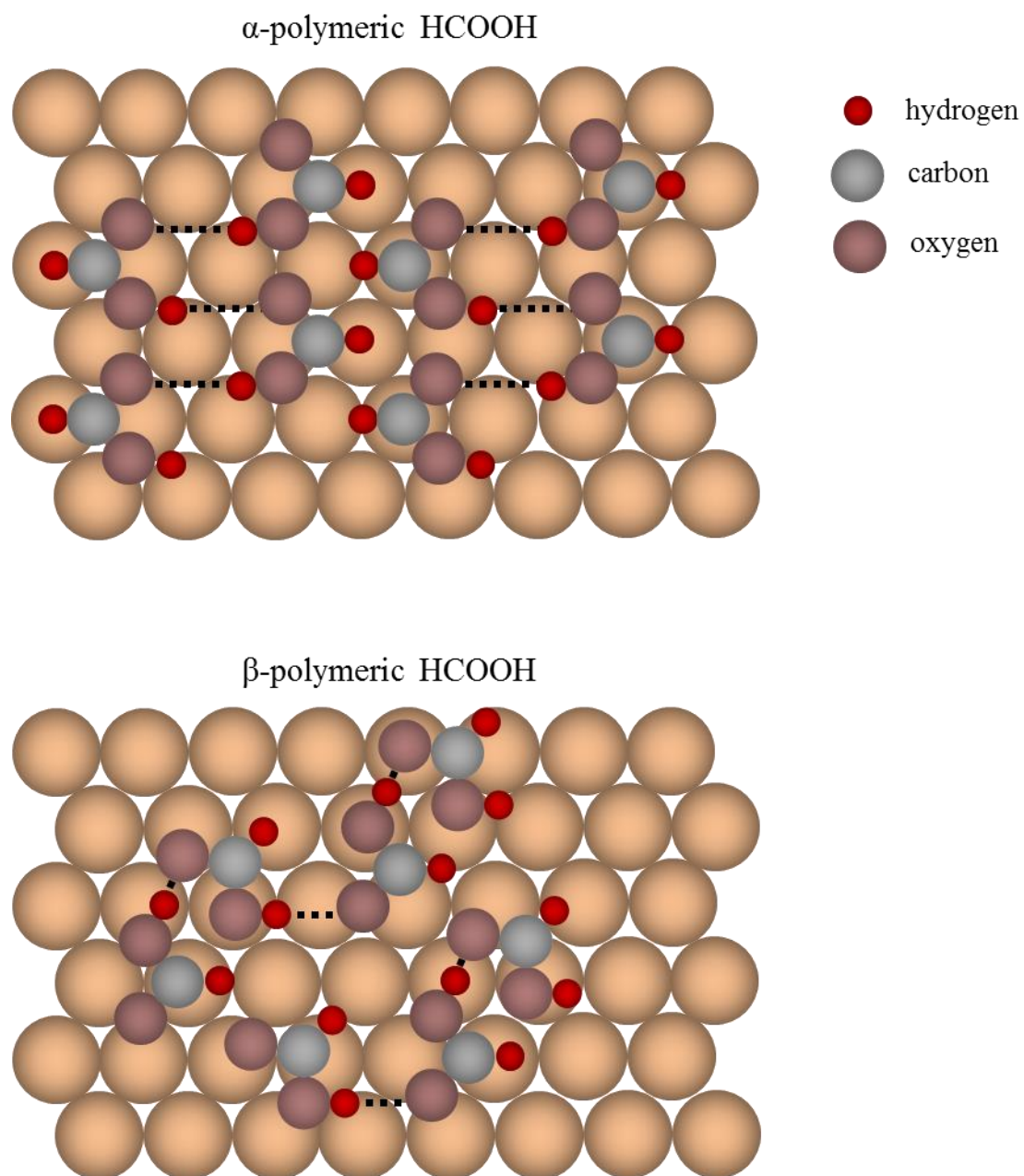


Figure 4.1. Model structures of adsorbed formic acid molecules as α - and β -polymeric formic acid.⁷⁰

4.2 Results and Discussion

4.2.1 The quantitative analysis of desorption kinetics parameter of HCOOH on Cu(111).

Figure 4.2 shows the TPD spectra of DCOOH adsorbed on Cu(111) at 85 K. Although the TPD of formic acid on Cu(110)^{37,39,40,42} has been investigated extensively, there are only a few reports on TPD of formic acid on Cu(111).^{44,45} The molecular DCOOH ($m/e = 47$) was desorbed at 180 K. A similar result has been reported in the case of DCOOH/Cu(110).³⁷ The H₂ ($m/e = 2$) was desorbed at 331 K, and the D₂ ($m/e = 4$) and CO₂ ($m/e = 44$) were desorbed at 447 K. These results indicate that a part of the formic acid desorb molecularly from Cu(111) at 180 K and the other molecules are dissociated; some DCOOH molecules are dissociated into the formate (DCOO) and a hydrogen atom. The dissociated hydrogen atoms were recombined and desorbed as H₂ at 331 K. The adsorbed formate species were further decomposed, and D₂ and CO₂ were immediately desorbed at 447 K (reaction limited desorption). These observations are similar to the previous results on Cu(110).^{37,39,42}

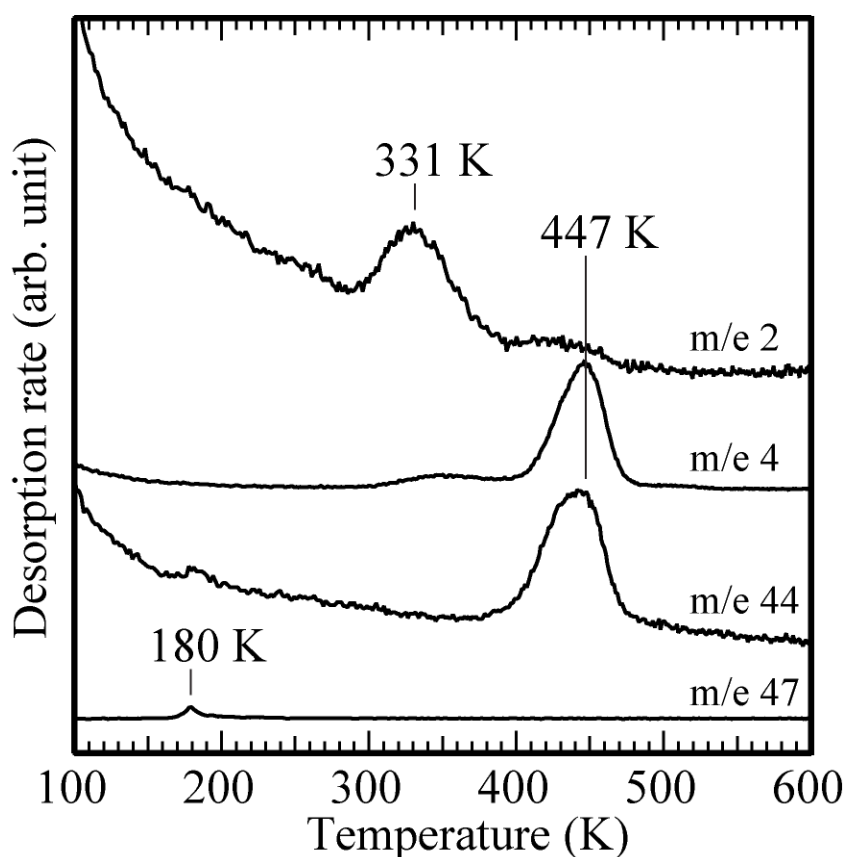


Figure 4.2. Multiplex TPD spectra of DCOOH adsorbed on Cu(111) at 85 K. The mass-to-charge-ratios (m/e) 47, 44, 4, and 2 correspond to DCOOH^+ , CO_2^+ , D_2^+ , and H_2^+ , respectively. The initial coverage of DCOOH was ~ 0.35 ML. The heating rate was 1.1 K/s.

Figure 4.3 shows C1s XPS spectra of the first layer HCOOH and CO on Cu(111) at 83 K at their saturation coverages. Similar XPS measurements were performed in order to estimate the initial coverages of adsorbed HCOOH. A peak for HCOOH was observed at 288.5 eV. On the other hand, three peaks were observed at 285, 290 and 294 eV for CO on Cu(111); the shoulder peaks at 290

and 294 eV were assigned to the shake-up satellites of CO on Cu(111).⁷¹ According to Hollins *et al.*, the saturation coverage of CO on Cu(111) was 0.52 ML.⁷² As compared with the integrated areas in Fig. 4.3, the saturation coverage of HCOOH was estimated to be 0.35 ML; here the number of surface Cu atoms is defined as 1 ML. On the other hand, the ideal structure of α -polymeric HCOOH species on Cu(111) shows the saturation coverage of 0.4 ML.⁶⁹ The present estimation is almost consistent with the saturation coverage of α -polymeric HCOOH; a small difference (0.05 ML) may originate from the defects and domain boundary of adsorbed HCOOH species.

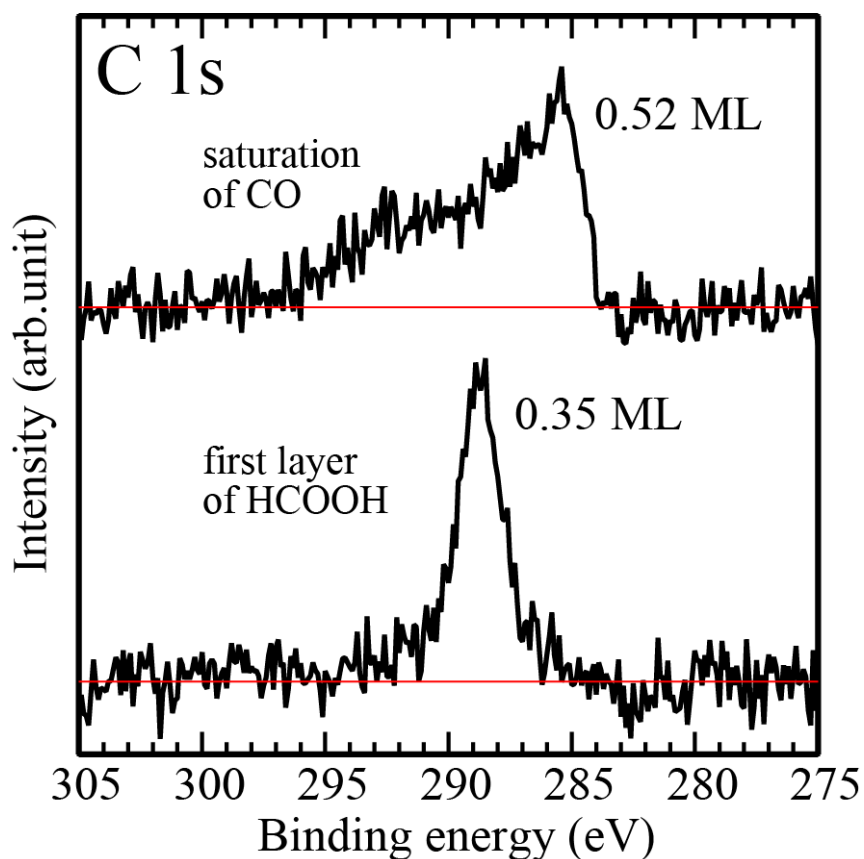


Figure 4.3. C1s XPS spectra of the saturated first layer HCOOH and CO saturation on Cu(111) at 83 K. When the number of surface Cu atoms was defined as 1 ML, the saturation coverage of CO was 0.52 ML⁷² and the first layer HCOOH was estimated to be 0.35 ML.

Figure 4.5 shows a series of TPD spectra of HCOOH adsorbed on Cu(111) at 85 K as a function of initial coverages. The mass number 29 (HCO^+) is the major cracking fragment of HCOOH. The TPD spectra in Fig. 4.4 have the following features. (1) With increasing coverage, the desorption peak maxima are shifted to higher temperatures. (2) The peak shape is asymmetrical. (3) At

submonolayer coverages, the leading edges of the desorption spectra are not perfectly aligned. These features indicate that the desorption order for molecular HCOOH should be between zero and first. In general, a zero order desorption at submonolayer coverages is observed in the case of a two-phase equilibrium between individual adsorbates and islands.^{73,74} On the other hand, if a molecular desorption occurs at island edges, the desorption kinetics should be a half order at submonolayer coverages, because the number of HCOOH species at the island edge is proportional to the square root of coverage. In fact, recent STM measurements have shown that adsorbed HCOOH species form islands at submonolayer coverages.⁴³ Thus, we concluded that the desorption order at submonolayer coverages is either zero or half.

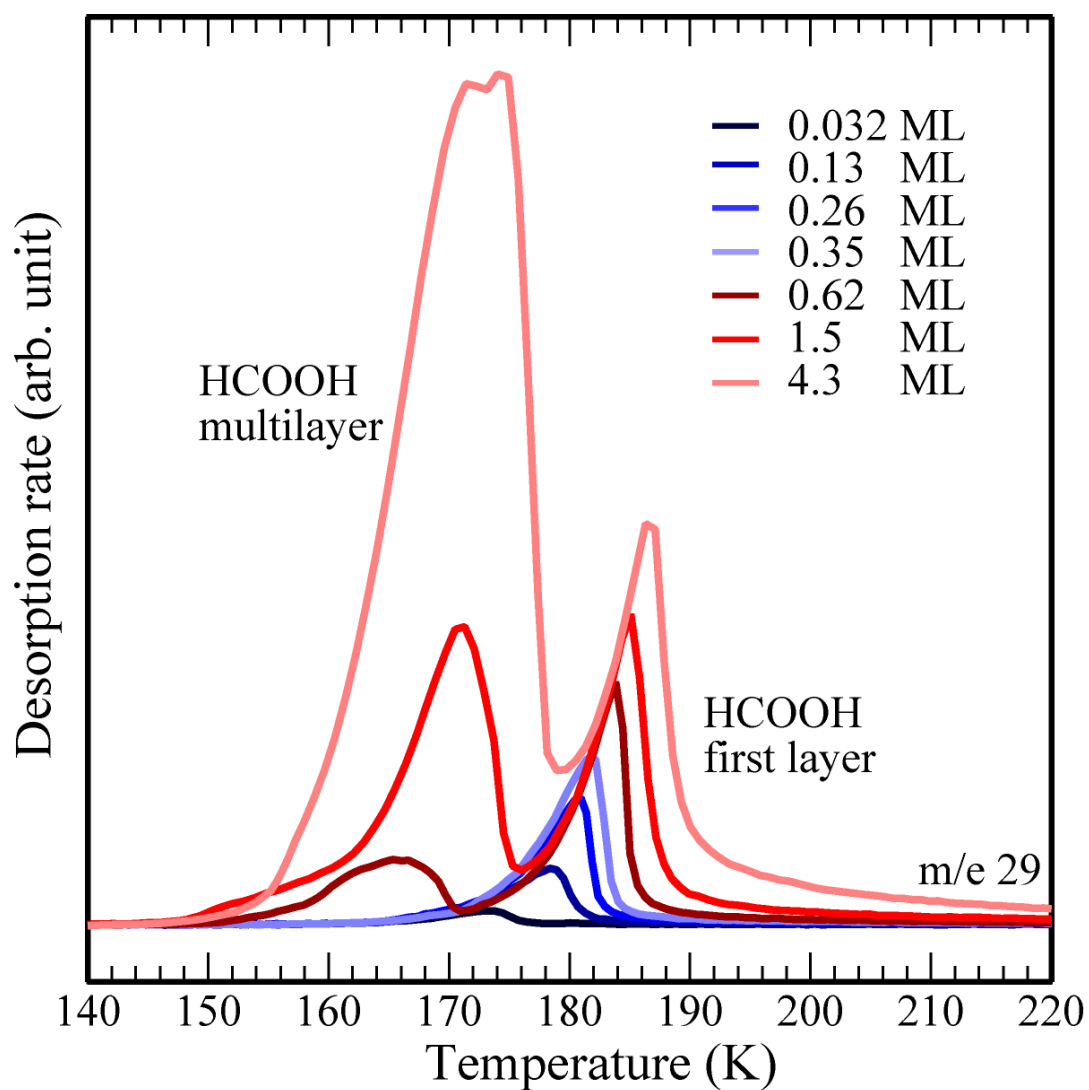


Figure 4.4. TPD spectra of HCOOH adsorbed on Cu(111) at 85 K as a function of coverages. The heating rate was 1.1 K/s.

Figure 4.5 shows an Arrhenius plot of one of the TPD spectra (0.26 ML) in Fig. 4.4. Here, the activation energy (E_d) can be directly estimated by the threshold TPD method without assuming of the desorption order.⁶⁵⁻⁶⁷ The activation energy for desorption is estimated to be 75 kJ/mol, in the case of 0.26 ML (Fig. 4.5). In order to estimate the pre-exponential factor for desorption, we need to assume the desorption order; the pre-exponential factors for zero (ν_0) and half ($\nu_{1/2}$) order desorption are estimated to be 10^{20} ML s⁻¹ and 10^{21} ML^{1/2} s⁻¹, respectively, in the case of 0.26 ML.

Figure 4.6 shows the activation energies for desorption of HCOOH as a function of initial coverage. The estimated values (53-75 kJ/mol) are considerably large in comparison with the previous theoretical estimations on Cu(111); the calculated adsorption energies were 0.22 eV (21 kJ/mol)³⁵ and 0.24 eV (23 kJ/mol)³⁶. It is noted that these theoretical studies assumed an isolated HCOOH molecule. However, in reality, adsorbed HCOOH species form a hydrogen bonding network on the Cu(111) surface.⁴³ The adsorbed HCOOH species in a hydrogen bonding network (i.e., α -polymeric HCOOH as discussed later) is more stable than an isolated HCOOH molecule. There is a tendency that the activation energy is slightly increased with the increase in HCOOH coverage.

This is probably due to the formation of α -polymeric HCOOH; a hydrogen bonding network is well-developed at higher coverages of adsorbed HCOOH on Cu(111). The decrease in activation energy at $\theta_{\text{ini}} = 0.35$ ML may be due to a lateral interaction between domains; as the coverage of the first layer HCOOH reaches saturation, a repulsive interaction may occur between HCOOH island domains.

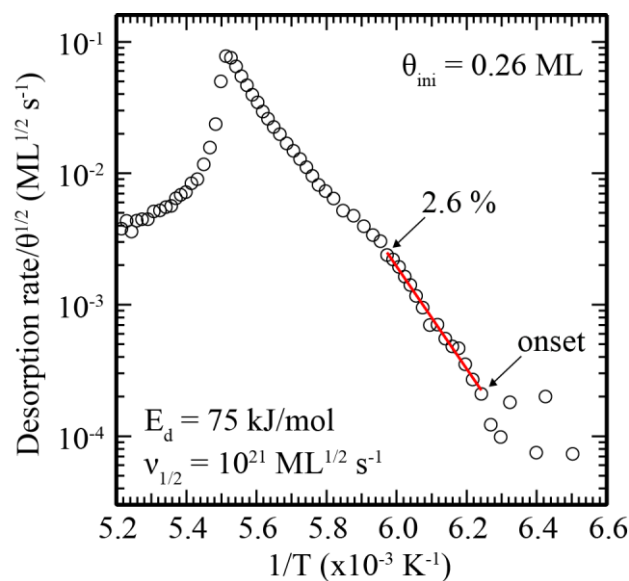


Figure 4.5. Arrhenius plot of TPD spectra for the first layer HCOOH on Cu(111) as a function of inverse temperature. The desorption onsets and 2.6% threshold increments are indicated by arrows. The desorption order was assumed to be a half for the estimation of the pre-exponential factor. The initial coverage of HCOOH (θ_{ini}) = 0.26 ML.

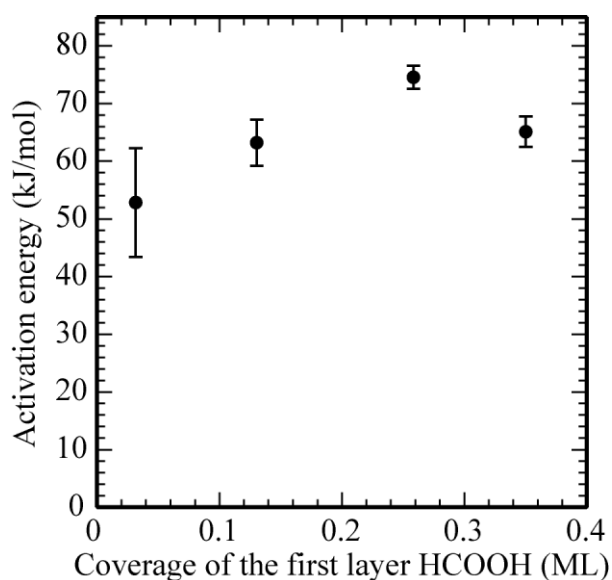


Figure 4.6. The activation energy for desorption of HCOOH on Cu(111). The initial coverage of HCOOH = 0.032, 0.13, 0.26 and 0.35 ML.

4.2.2 The quantitative analysis of dissociation kinetics from HCOOH to monodentate formate on Cu(111).

Figure 4.7 shows a series of TR-IRAS spectra of 0.26 ML HCOOH adsorbed on Cu(111) at 155.3 K as a function of elapsed time. Gaseous HCOOH molecules were introduced onto the Cu(111) surface at $t = 0$ (s). The spectra were arranged at 76.4 s intervals from the bottom spectra. Four peaks were observed at 1709, 1655, 1080 and 980 cm^{-1} . The peak assignments are summarized in Table 4.1. The peak at 1709 cm^{-1} is assigned to a CO double bond stretching mode $\nu(\text{C}=\text{O})$ of α -polymeric HCOOH.^{43,69,70} The peaks at 1080 and 980 cm^{-1} are assigned to the out-of-plane bending modes of CH $\pi(\text{CH})$ and OH $\pi(\text{O}-\text{H})$ of α -polymeric HCOOH, respectively.^{43,69,70} Formic acid molecules could form monomer, dimer, α -polymer, and β -polymer species on the metal surfaces.⁶⁸⁻⁷⁰ The α -polymer and β -polymer are adsorbed with its molecular plane parallel to the surface. The $\pi(\text{O}-\text{H})$ vibrational mode for α -polymer is observed at 975⁴³, 980⁷⁰ and 981⁶⁹ cm^{-1} . The present observation of 980 cm^{-1} is close to those of α -polymer species. The peak at 1655 cm^{-1} is assigned to a double bond stretching mode $\nu(\text{C}=\text{O})$ of monodentate formate.³⁸ With the increase of elapsed time, the 1080 and 980 cm^{-1} peaks decrease, and the peak

assigned to the monodentate formate (1655 cm^{-1}) increases. This indicates that α -polymeric HCOOH species were dissociated into monodentate formate species. Similar TR-IRAS experiments were conducted at 152.3, 158.3 and 161.3 K.

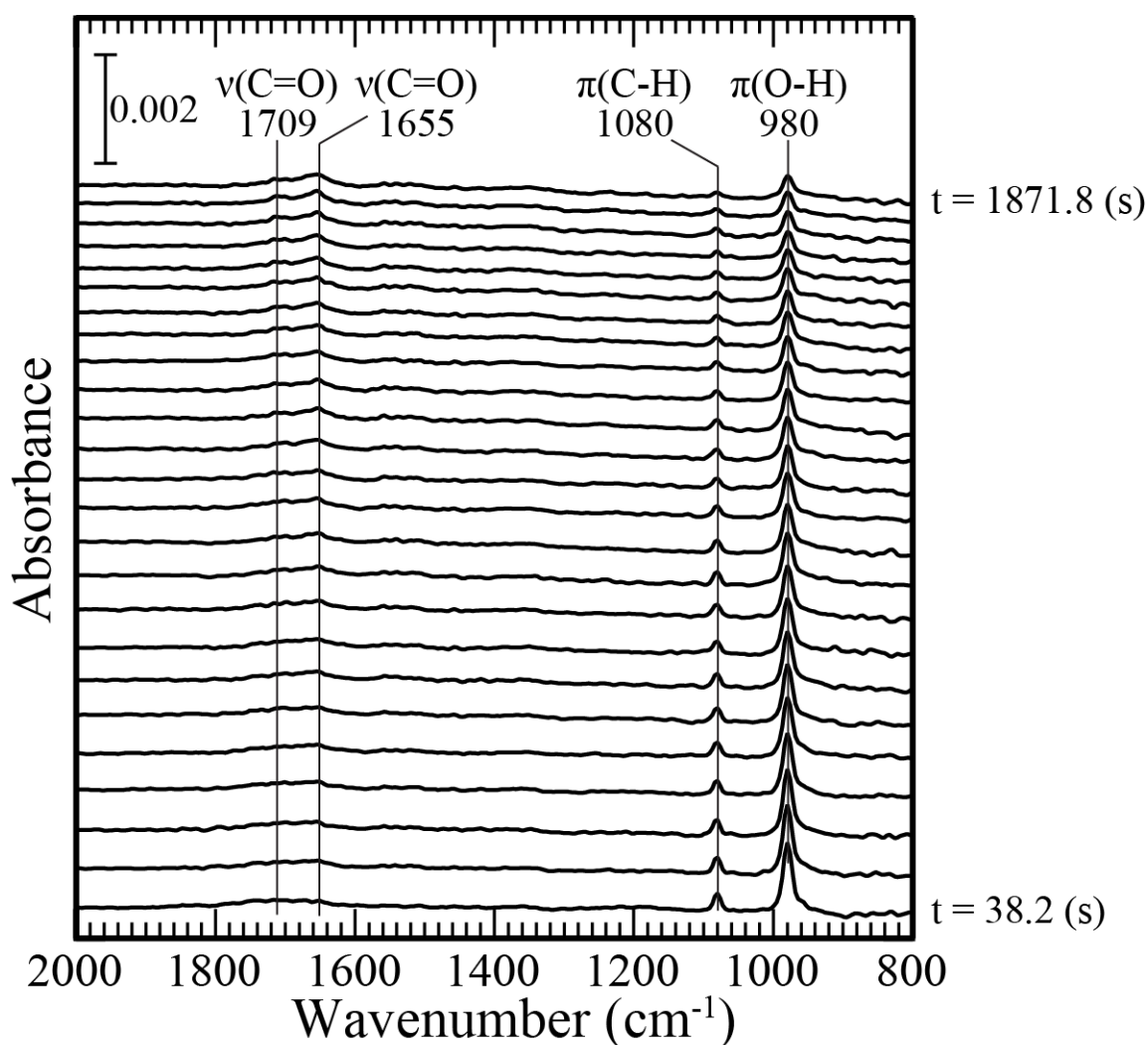


Figure 4.7. TR-IRAS spectra of 0.26 ML HCOOH adsorbed on Cu(111) at 155.3 K as a function of elapsed time after the gas injection at $t = 0\text{ s}$. The spectra were arranged at 76.4 s intervals from the bottom spectra.

Table 4.1. Assignments of the observed vibrational peaks (cm^{-1}) of HCOOH and formate species on Cu(111).^{38,43,44,69,70}

Vibrational mode	Cu(111) ⁴⁴ (chapter 4)	Cu(110) ³⁸ (IRAS)	Cu(111) ⁴³ (IRAS)	Pt(111) ⁷⁰ (HREELS)	Au(111) ⁶⁹ (HREELS)
$\nu(\text{C}=\text{O})$ formic acid	1709 α -polymeric	1733 condensed	1720 α -polymeric	1720 α -polymeric	1714 α -polymeric
$\nu(\text{C}=\text{O})$ formate	1655 monodentate	1640 - 1670 monodentate	1655 ($\nu_{\text{as}}(\text{OCO})$) linked-formate ⁴³	-	-
$\pi(\text{C}-\text{H})$ formic acid	1080 α -polymeric	1078 condensed	1084 α -polymeric	-	1082 α -polymeric
$\pi(\text{O}-\text{H})$ formic acid	980 α -polymeric	960 condensed	975 α -polymeric	980 α -polymeric	981 α -polymeric

ν : stretching mode, π : out-of-plane bending mode

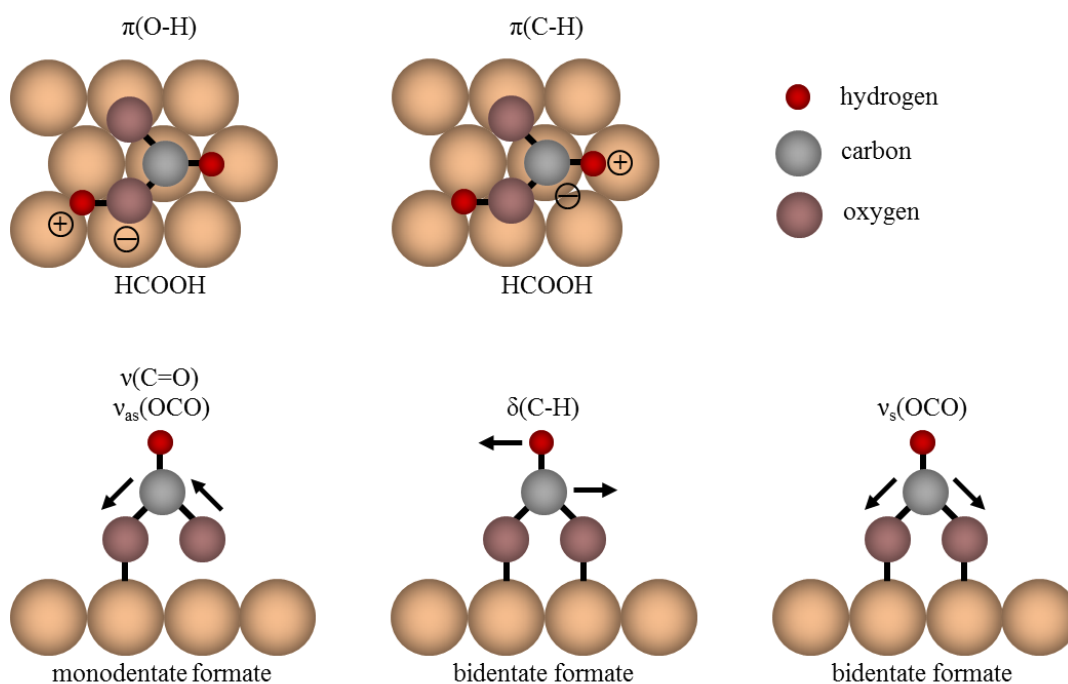
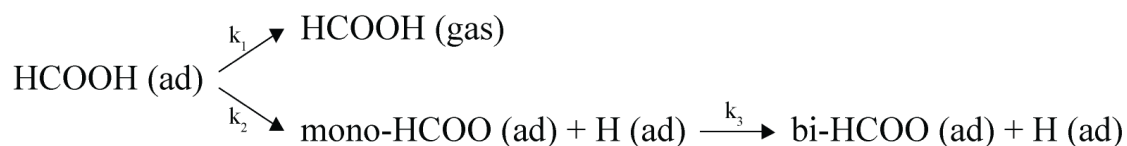


Figure 4.8. Internal vibrations of HCOOH, monodentate formate and bidentate formate species on Cu(111).

Figure 4.9 shows the plots of (a) the integrated area of $\nu(\text{C}=\text{O})$ of the monodentate formate at 1655 cm^{-1} and (b) logarithms with the integrated area of $\pi(\text{O}-\text{H})$ of the formic acid at 980 cm^{-1} as a function of elapsed time at the indicated temperatures. In Fig. 4.9 (a), the peak assigned to $\nu(\text{C}=\text{O})$ of monodentate formate increases, but the intensity of each peak is too weak to analyze their kinetics quantitatively. We should note that the decrease of $\pi(\text{O}-\text{H})$ intensities could include the desorption and dissociation of adsorbed HCOOH species and the conversion from monodentate formate to bidentate formate as shown below:



The k_1 ($\text{ML}^{1/2}\text{ s}^{-1}$; here we assume a half order desorption) is the rate constant for the desorption of adsorbed HCOOH , the k_2 (s^{-1}) is the rate constant for the first order dissociation from HCOOH to monodentate formate and the k_3 (s^{-1}) is the rate constant for the conversion from monodentate formate to

bidentate formate. On the other hand, $\nu(\text{OCO})$ of bidentate formate ($\sim 1345 \text{ cm}^{-1}$) was not clearly observed within the decrease of adsorbed HCOOH. Thus, the decrease of adsorbed HCOOH can be written as follows:

$$-\text{d}[\text{HCOOH (ad)}]/\text{dt} = k_1 \cdot [\text{HCOOH (ad)}]^{1/2} + k_2 \cdot [\text{HCOOH (ad)}].$$

In order to confirm the branching ratio between the desorption and dissociation for adsorbed HCOOH species, XPS measurements were performed. HCOOH desorption was activated on Cu(111) by heating the sample above $\sim 170 \text{ K}$ (Fig. 4.2). According to the decrease of the area intensity for C 1s spectra, 90% of the adsorbed HCOOH was desorbed molecularly from the Cu(111) surface by this heating.

On the other hand, after the isothermal observation of the HCOOH adsorbed Cu(111) surface at 158.9 K for 2400 s , the HCOOH species mostly changed into monodentate formate species. The post-annealing XPS data indicated that the decrease in the area intensity of C 1s spectra was less than 6%. Thus, the predominant reaction in this isothermal experiment at 158.9 K is the dissociation into monodentate species, i.e., $k_1 \cdot [\text{HCOOH (ad)}]^{1/2} \ll k_2 \cdot [\text{HCOOH (ad)}]$. Therefore, we can safely assume that $-\text{d}[\text{HCOOH (ad)}]/\text{dt} \doteq k_2[\text{HCOOH (ad)}]$,

and the k_2 of the rate constant for dissociation was directly estimated from the decrease of the $\pi(\text{O-H})$ peak in the TR-IRAS spectra at each temperature. Here, we assume the conversion from HCOOH to monodentate formate species to be a first order reaction at the temperature range between 152.3 and 161.3 K, and the fitting in Fig. 4.9 (b) was performed, assuming the first-order dissociation.

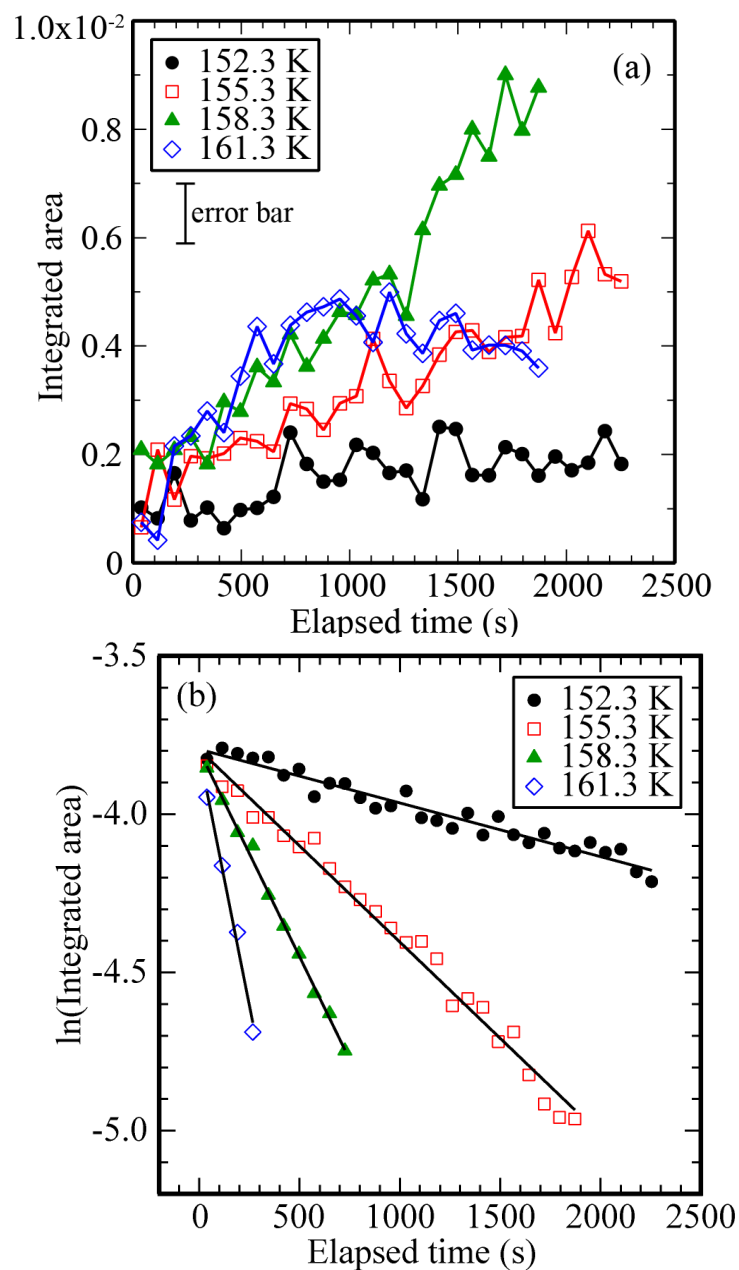


Figure 4.9. (a) The plots of integrated area of monodentate formate $\nu(\text{C}=\text{O})$ as a function of elapsed time. (b) The plots of integrated area of formic acid $\pi(\text{O}-\text{H})$ as a function of elapsed time. The fittings were performed by assuming a first order dissociation reaction at each temperature. At $t = 0$ (s), 0.26 ML HCOOH was adsorbed on $\text{Cu}(111)$. The error bar was estimated from signal-noise-to-ratio of IRAS spectra.

Figure 4.10 shows an Arrhenius plot of the rate constants (k_2) for dissociation from HCOOH to monodentate formate. The activation energy of O-H dissociation (E_a) was estimated to be 65.0 ± 4.5 kJ/mol and the pre-exponential factor (ν_1) was estimated to be $10^{18.6 \pm 1.5} \text{ s}^{-1}$.

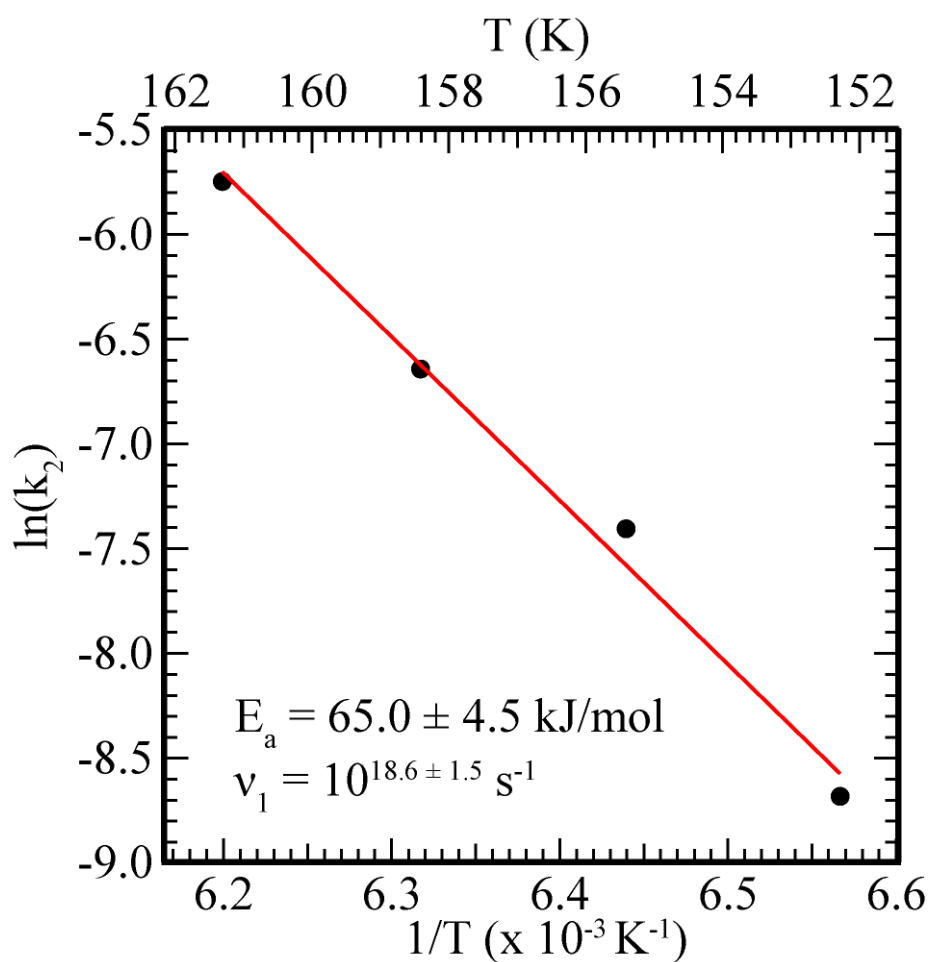


Figure 4.10. Arrhenius plot of $\ln(k_2)$ of $\pi(\text{O-H})$ for HCOOH on Cu(111). The initial coverage of HCOOH (θ_{ini}) = 0.26 ML.

In the previous theoretical studies, no stable monodentate formate species on Cu(111) were found at 1/9 ML coverage.³⁵ The activation energy from formic acid to bidentate formate was calculated to be 0.68 eV (66 kJ/mol)³⁵ and 0.61 eV (59 kJ/mol)³⁶. They have noted that the coverage effects (lateral adsorbate-adsorbate interactions) can play an important role in determining the structural stability of various adsorbed states.³⁵

Figure 4.11 shows a series of TR-IRAS spectra of 0.26 ML HCOOH adsorbed on Cu(111) at 165.1 K as a function of elapsed time. The spectra were arranged at 239 s intervals from the bottom spectrum. At least five peaks were observed at 1709, 1655, 1360, 1345 and 980 cm^{-1} . The peaks at 1709 and 1655 cm^{-1} are assigned to $\nu(\text{C}=\text{O})$ of α -polymeric HCOOH and monodentate formate species.^{43,69,70} The peak at 980 cm^{-1} is assigned to $\pi(\text{O}-\text{H})$ of α -polymeric HCOOH.^{43,69,70} The peak of $\pi(\text{C}-\text{H})$ for α -polymeric HCOOH (1080 cm^{-1}) was too weak to be detected. The peaks at adsorbed HCOOH were only observed within 119 s at 165.1 K. There is no spectroscopic evidence that HCOOH exists on the surface at 358 s. The peaks at 1360 and 1345 cm^{-1} are previously assigned to

the stretching mode $\nu(\text{OCO})$ of linked-formate (monodentate formate species) and bidentate formate, respectively.⁴³ However, with the increase of elapsed time, the peak assigned to $\nu(\text{C=O})$ of monodentate formate species (1655 cm^{-1}) decreases, and the peaks at 1360 cm^{-1} and at 1345 cm^{-1} increase. We consider that the peak at 1360 cm^{-1} originates from $\nu(\text{OCO})$ of bidentate formate species. After annealing at 165.1 K , HCOOH species dissociate into bidentate formate via monodentate formate at a submonolayer coverage. If the island structure remains after the dissociation of adsorbed HCOOH , the bidentate formate of the inner part of an island could show different vibrational energies in comparison with the island edges. The observed two peaks for $\nu(\text{OCO})$ at 1360 and 1345 cm^{-1} may be due to this local environmental effect. After annealing above 215 K , the peak at 1360 cm^{-1} completely disappeared and only the peak at 1345 cm^{-1} was observed.⁴³ The bidentate formate species could diffuse on the $\text{Cu}(111)$ surface at higher temperature. The environment around bidentate formate species may become homogeneous. Thus, the vibrational frequency of bidentate formate species can be changed by their surrounding environment.

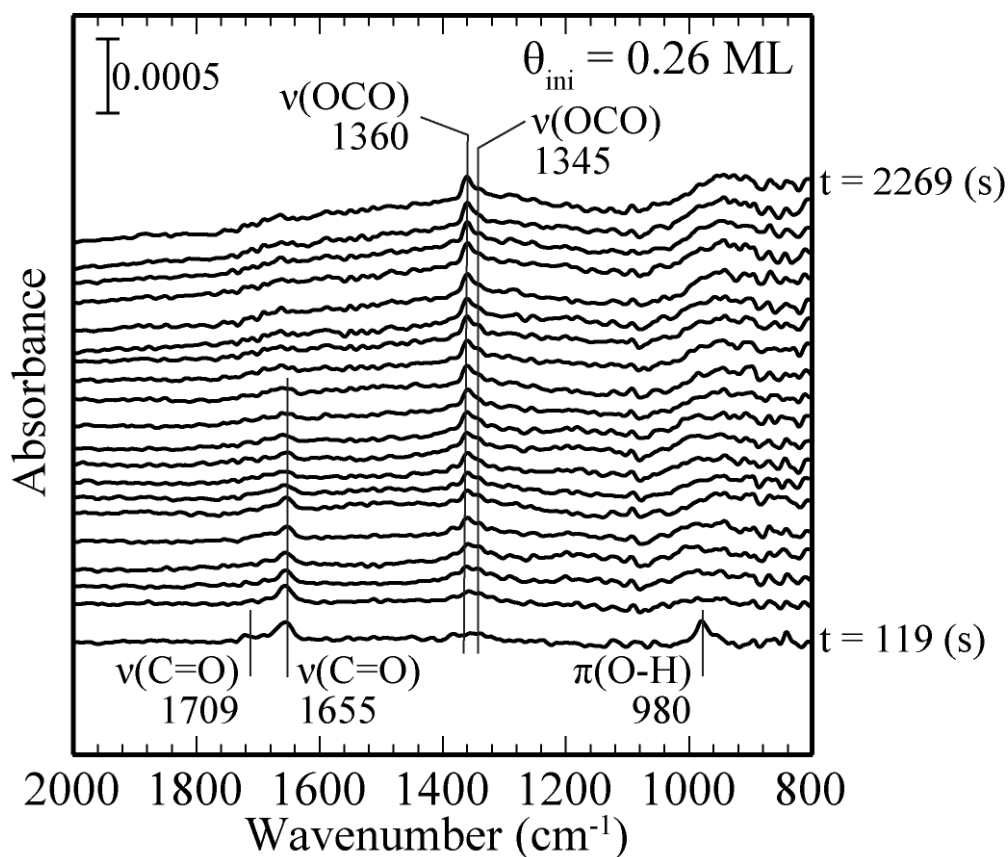


Figure 4.11. TR-IRAS spectra of 0.26 ML HCOOH adsorbed on Cu(111) at 165.1 K as a function of elapsed time after the gas injection at $t = 0$ s. The spectra were arranged at 239 s intervals from the bottom spectra.

Figure 4.12 shows a series of TR-IRAS spectra of 0.5 ML HCOOH adsorbed on Cu(111) at 165.1 K (more than mono layer) as a function of elapsed time. The spectra were arranged at 239 s intervals from the bottom spectra. Four peaks were observed at 1738, 1656, 1080 and 980 cm^{-1} . The peak at 1738 cm^{-1} is assigned to $\nu(\text{C}=\text{O})$ of multilayer HCOOH.^{43,69,70} The peak at 1656 cm^{-1} is

assigned to $\nu(\text{C}=\text{O})$ of monodentate formate species.^{38,43} The peaks at 1080 and 980 cm^{-1} are assigned to $\pi(\text{CH})$ and $\pi(\text{O}-\text{H})$ of α -polymeric HCOOH, respectively.^{43,69,70} The STM study has reported that the dissociation of α -polymeric HCOOH occurs at the island edges, because HCOOH must transfer a hydrogen atom to a Cu vacant site when it is dissociated into monodentate formate and a hydrogen atom.⁴³ If HCOOH molecules cover the entire surface of Cu(111), dissociation can occur only after the desorption of some HCOOH molecules from the surface. The present TPD measurements show that the threshold temperatures for desorption of the first layer and multilayer HCOH are 165 K and 150 K, respectively (Fig. 4.4). With the increase of elapsed time, the 1080 and 980 cm^{-1} peaks decrease, and the peak assigned to the monodentate formate species (1656 cm^{-1}) increases, indicating that α -polymeric HCOOH was dissociated into monodentate formate species. This process is similar to the result for 0.26 ML HCOOH on Cu(111) at 155.3 K (Fig. 4.7). Thus, the desorption of adsorbed HCOOH is a rate-limiting step for the dissociation from HCOOH to monodentate formate species at higher initial coverages of adsorbed HCOOH. Monodentate formate species were not easily converted into bidentate formate species at a high initial coverage. The number of surface Cu atoms

required to form the bidentate formate is twice that of monodentate formate; the saturation coverage of bidentate formate on Cu(111) was estimated to be 0.25 ML.⁴⁶ If the first layer coverage reaches near saturation, it is difficult for monodentate formate species to move on the surface in order to access Cu vacant sites to form a bidentate configuration.

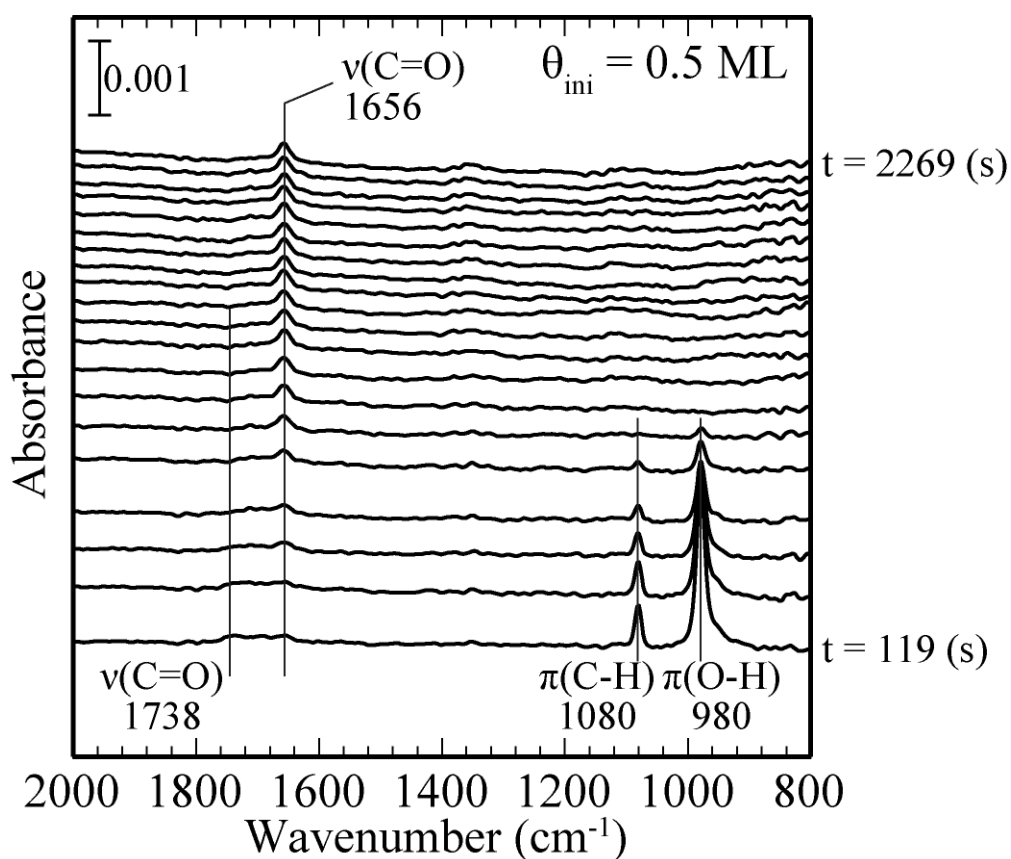


Figure 4.12. TR-IRAS spectra of 0.5 ML HCOOH adsorbed on Cu(111) at 165.1 K as a function of elapsed time after the gas injection at $t = 0$ s. The spectra were arranged at 239 s intervals from the bottom spectra.

There are two important factors that control the reaction kinetics of HCOOH on Cu(111). The first one is the structure of the adsorbed HCOOH species. The α -polymeric HCOOH species are stabilized by the hydrogen bonding network, which needs more energy to desorb from the surface than an isolated HCOOH on Cu(111). The second one is the amount of vacant sites on Cu(111).

Adsorbed HCOOH species must transfer a hydrogen atom to a Cu vacant site when they are dissociated into formate species. In addition, monodentate formate species are not easily changed into bidentate formate species at higher initial coverages of adsorbed HCOOH (Fig. 4.12). Therefore the number of Cu vacant sites controls the reaction rate from adsorbed HCOOH into bidentate formate via monodentate formate species.

The previous theoretical study reported that the activation energy from monodentate to bidentate formate species was calculated to be only 0.03 eV (3 kJ/mol)³⁶. This small value suggests that the process from monodentate to bidentate formate is very fast. However, based on the present TR-IRAS results (152.3~161.3 K), the process must be slower than the dissociation from HCOOH to monodentate formate. This indicates that the activation energy from monodentate to bidentate formate species was larger than that for the dissociation of HCOOH species at 0.26 ML at this temperature range, i.e., more than 65 kJ/mol. The theoretical studies assumed simply an isolated monodentate formate species, where vacant sites are available around the monodentate formate.

4.3 Conclusions

In chapter 4, we conducted the quantitative analysis of desorption and decomposition kinetics of the first layer HCOOH on Cu(111) using TPD, XPS and TR-IRAS. HCOOH molecules on Cu(111) at low temperature are stabilized to form α -polymer species. The surface reaction of HCOOH on Cu(111) involves both desorption and dissociation at low temperature. The HCOOH desorption from the Cu(111) surface could be the zero or half order process at submonolayer coverages. When the HCOOH coverage is 0.26 ML, the activation energy for desorption is estimated to be 75 kJ/mol. The dissociation of HCOOH into monodentate formate is the first order process at a submonolayer coverage. The activation energy for dissociation is estimated to be 65.0 kJ/mol. The present results show that the presence of a hydrogen bonding network stabilizes the HCOOH species and leads to a change into monodentate formate species. The monodentate formate species are also stabilized due to the coverage effects.

Chapter 5

The dissociation of formic acid on Zn-Cu(111) and Zn-Cu(997) studied by TPD, high-resolution XPS and IRAS

The decomposition of formic acid (HCOOH) on Zn-Cu(111) and Zn-Cu(997) were performed by high-resolution X-ray photoelectron spectroscopy (HR-XPS), temperature programmed desorption (TPD) and infrared reflection absorption spectroscopy (IRAS). Less than 4% of adsorbed HCOOH are dissociated into the bidentate formate species on Zn-Cu(111). On the other hand, a part of adsorbed HCOOH (17%) are dissociated into monodentate formate species on Cu(997) at 83 K, indicating that the stepped Cu surface has higher reactivity for the HCOOH dissociation at low temperature. When the Zn-Cu surface alloy was formed on Cu(997), the coverage of formate species increased in contrast to the Zn-Cu(111). The desorption peak maximum of the formate decomposition on Zn-Cu(997) were higher than Cu(997). Vibrational spectra of formate species on Zn-Cu(997) show that bidentate formate species were observed at the Zn-Cu alloyed sites after heating at 472 K.

The Zn plays an important role in the stabilization of the formate species on the Zn-Cu alloyed surface.

5.1 Introduction

The stepped surfaces have attracted much attention, because unique catalytic reactions may occur at the step sites.^{18,47–50,56,75,76} For example, the stepped Cu surfaces have some reactivity for CO₂ dissociation under ultrahigh vacuum.^{75,76} Although CO₂ is chemically inert, the step site on a Cu surface plays an important role for the molecular activation.

The alloying effects are also important in the area of metal catalysts because specific catalytic activities emerge upon alloying. In fact, the binary Zn-Cu catalyst shows excellent catalytic activity for methanol synthesis reaction from CO₂ and H₂.^{5,13,16–18} According to the previous studies of powdered Cu/ZnO catalysts for methanol synthesis reaction, the ZnO functions as a physical spacer between Cu nanoparticles for the high Cu surface areas on industrial catalysts.^{17,18,77} In addition, Nakamura *et al.*¹⁷ reported that in a powdered Cu/ZnO catalyst the formation of the Cu–Zn surface alloy is responsible for the promotion

of methanol synthesis activity from CO_2 and H_2 .¹⁷ The role of the Cu–Zn site in the reaction mechanism is the promotion of the hydrogenation of formate to methoxy species.¹⁷

However, the exact role of Zn is not fully understood yet. In reality, there are variable defects and lattice strain in a heterogeneous catalyst. According to the previous theoretical study, alloying of Zn into the Cu(211)-step decreased the activation barriers between intermediates for methanol synthesis reaction.¹⁸ In order to understand the role of Zn, the reaction including the intermediates (i.e., formate species) must be studied experimentally on well-defined Zn-Cu step surface.

In chapter 5, we report the decomposition reaction of formic acid on Zn-Cu(111) and Zn-Cu(997) as well as clean Cu(111) and Cu(997) using XPS, TPD and IRAS. Based on these measurements, the adsorption states and dissociation process of HCOOH on Cu(997) and Zn-Cu(997) are discussed in detail. We demonstrate that the Cu(997) has higher reactivity for the HCOOH dissociation than that on Cu(111) at low temperature. The HCOOH adsorbed on the Zn-Cu alloyed surfaces are less stable than clean Cu surfaces. However the

produced formate species are stabilized up to 500 K on the Zn-Cu alloyed surfaces.⁷⁸ Thus, the Zn plays a vital role in the stabilization of formate species on the Zn-Cu surfaces.

5.2 Results and Discussion

Figure 5.1 shows C 1s XPS spectra of clean (black), multilayer (green) and the first layer (red) cyclohexane on Cu(111) at 84 K. The spectra were measured using a photon energy of 630 eV. There have been no reports for XPS spectra of cyclohexane on Cu(111). The coverages of adsorbed HCOOH and formate species on Cu(111) were estimated by the C 1s spectra for the first layer cyclohexane (Wako chemicals, 99.5% purity). The peak of multilayer cyclohexane was observed at 284.5 eV, and the peak of the first layer cyclohexane was observed as a shoulder peak at 284.1 eV (green). According to TPD measurements, the desorption peaks for multilayer and the first layer cyclohexane on Cu(111) were observed at 140 K and 180 K, respectively.⁷⁹ The first layer cyclohexane on Cu(111) was prepared by annealing the multilayer cyclohexane at 159 K for 60 s (red). The peak is asymmetric on the high binding

energy side, which might be due to the vibrational fine structures for the first layer cyclohexane.^{80,81} The structure for the first layer cyclohexane on Cu(111) shows a ($\sqrt{7} \times \sqrt{7}$) R19.1° structure, and thus the coverage of the C atom for the first layer cyclohexane on Cu(111) is defined as 6/7 ML.⁸²

Figure 5.2 shows C 1s XPS spectra of clean (black) and CO saturation (red) on Cu(997) at 80 K. The spectra were measured using a photon energy of 630 eV. Three peaks were observed at 286, 289 and 293 eV for CO on Cu(997); the shoulder peaks at 289 and 293 eV were assigned to the shake-up satellites of CO on Cu(997).⁷¹ The coverages of HCOOH and formate species on Cu(997) were estimated by the C 1s spectra for the saturation coverage of CO on Cu(997). According to the LEED for the saturation coverage of CO on Cu(997) at 85 K, a (1.4×1.4) superstructure was observed, and the saturation coverage of CO on Cu(997) is determined as 0.52 ML.⁵⁶

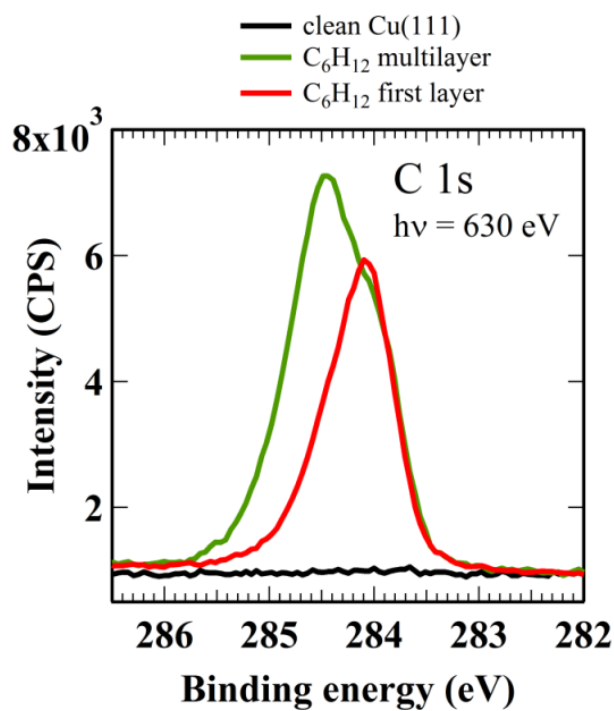


Figure 5.1. C 1s XPS spectra of clean (black), multilayer (green) and the first layer (red) cyclohexane on Cu(111) at 84 K. The spectra were measured using a photon energy of 630 eV.

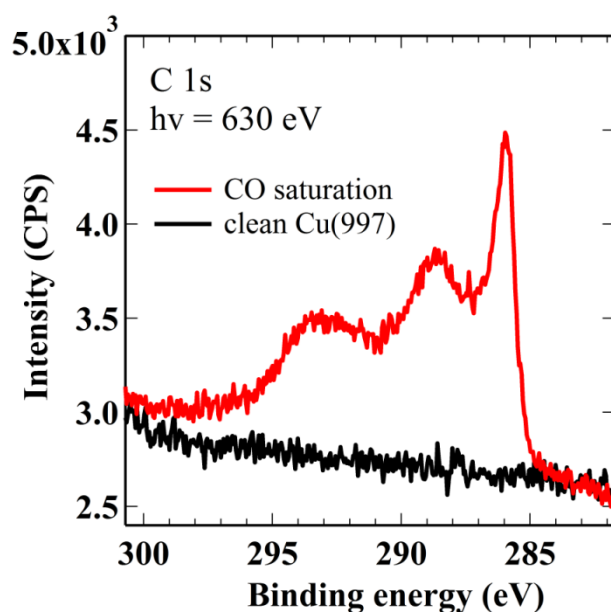


Figure 5.2. C 1s XPS spectra of clean (black) and CO saturation (red) on Cu(997) at 80 K. The spectra were measured using a photon energy of 630 eV.

Figure 5.3 show a series of (a) C 1s and (b) O 1s XPS spectra of 0.28 ML HCOOH (less than mono layer) on Cu(111) at 80 K and subsequent annealing. The spectra were measured using a photon energy of 630 eV. Baber *et al.* have already reported the XPS results for multilayer HCOOH adsorbed on Cu(111) at 90 K and subsequent annealing.⁴³ Three peaks were observed at 289.5 (533.1), 288.5 (532.1) and 287.7 (531.0) eV in Fig. 5.3 (a) and (b), respectively for C 1s (O 1s). The peak at 289.5 (533.1) eV is assigned to the first layer HCOOH on Cu(111).⁴³ After heating the sample up to 188 K, adsorbed HCOOH peaks (C 1s: 289.5 eV and O 1s: 533.1 eV) gradually decreased and shoulder peaks (C 1s: 288.5 eV and O 1s: 532.1 eV) became visible. According to the present IRAS measurements, adsorbed HCOOH species (0.26 ML) dissociated into monodentate formate species after annealing at 152.3~161.3 K (chapter 4.3.2).⁴⁴ Therefore, the peak at 288.5 (532.1) eV is assigned to monodentate formate species. This is also in agreement with Baber *et al.*; they reported that the peak of monodentate formate species (linked-formate) was observed at 288.0 eV, when the HCOOH and formate species are co-adsorbed on Cu(111).⁴³ According to the present TPD result, the desorption peak for the first layer HCOOH on Cu(111) was observed at 182 K (chapter 4.3.1).⁴⁴ After

heating the sample to 215 K which is sufficiently higher than the desorption peak for the first layer HCOOH, adsorbed HCOOH desorbed molecularly from the surface and only the formate derived peak was observed. The peak at 287.7 (531.0) eV is assigned to bidentate formate species because this peak was observed above room temperature. These XPS results are consistent with the present IRAS measurements; adsorbed HCOOH species dissociate into bidentate formate via monodentate formate at a submonolayer coverage.⁴⁴ The bidentate formate should be stable on Cu(111) up to 447 K (chapter 4.3.1).⁴⁴

Figure 5.3 (c) C 1s and (d) O 1s show a series of XPS spectra of 0.28 ML HCOOH (less than mono layer) on Zn (0.4 ML)-Cu(111) at 80 K and subsequent annealing. Two peaks were clearly observed at 289.5 (533.1) eV and 289.1 (532.0) eV for C 1s (O 1s) spectra. The peaks at 289.5 eV (C 1s) and 533.1 eV (O 1s) were observed up to 175 K, which are assigned to adsorbed HCOOH on Zn-Cu(111). After annealing the sample at 188 K, the peaks of adsorbed HCOOH decreased and small peaks are observed at 289.5 and 533.1 eV. The desorption temperature of HCOOH adsorbed on Zn-Cu(111) was lower than that on Cu(111). The peaks at 289.5 eV (C 1s) and 533.1 eV (O 1s) remained after further annealing to 377 K. According to the previous O 1s XPS

spectra for post methanol synthesis reaction, the O 1s for the bidentate formate on Zn-Cu(111) was observed at 531.7 eV.⁷⁸ Therefore, the peak at 532.0 (289.1) eV is assigned to the bidentate formate species on Zn-Cu(111). The peak of monodentate formate species was not clearly observed on Zn-Cu(111). This is probably due to higher binding energy of monodentate formate species on the Zn-Cu surface in comparison with that on a clean Cu surface. It is predicted that the peak of monodentate formate species should be observed between adsorbed HCOOH and bidentate formate species.

We estimated the coverage of bidentate formate species to the initial coverage of adsorbed HCOOH. In Fig. 5.3 (a) and (c) of C 1s spectra, the peaks of adsorbed HCOOH (blue line) and bidentate formate species (red line) were fitted by single Voigt peaks with a Shirley-background, respectively. The 13% of adsorbed HCOOH dissociated into the bidentate formate species on Cu(111) at 309 K. On the other hand, adsorbed HCOOH mostly desorbed from the Zn-Cu(111) surface at 188 K and some HCOOH were dissociated. Less than 4% of adsorbed HCOOH dissociated into the bidentate formate species on Zn-Cu(111) at 377 K.

The previous STM study reported the formation process of Zn-Cu surface alloy.⁸³ After annealing the Zn-deposited Cu(111) at 523 K, Zn atoms distributed homogeneously over the terrace to form the alloy.⁸³ The Zn at the terrace sites inactivates the HCOOH dissociation on Cu(111). These results may originate from the adsorbed HCOOH structure: the HCOOH on Zn-Cu(111) does not form the stable structure like polymeric HCOOH.

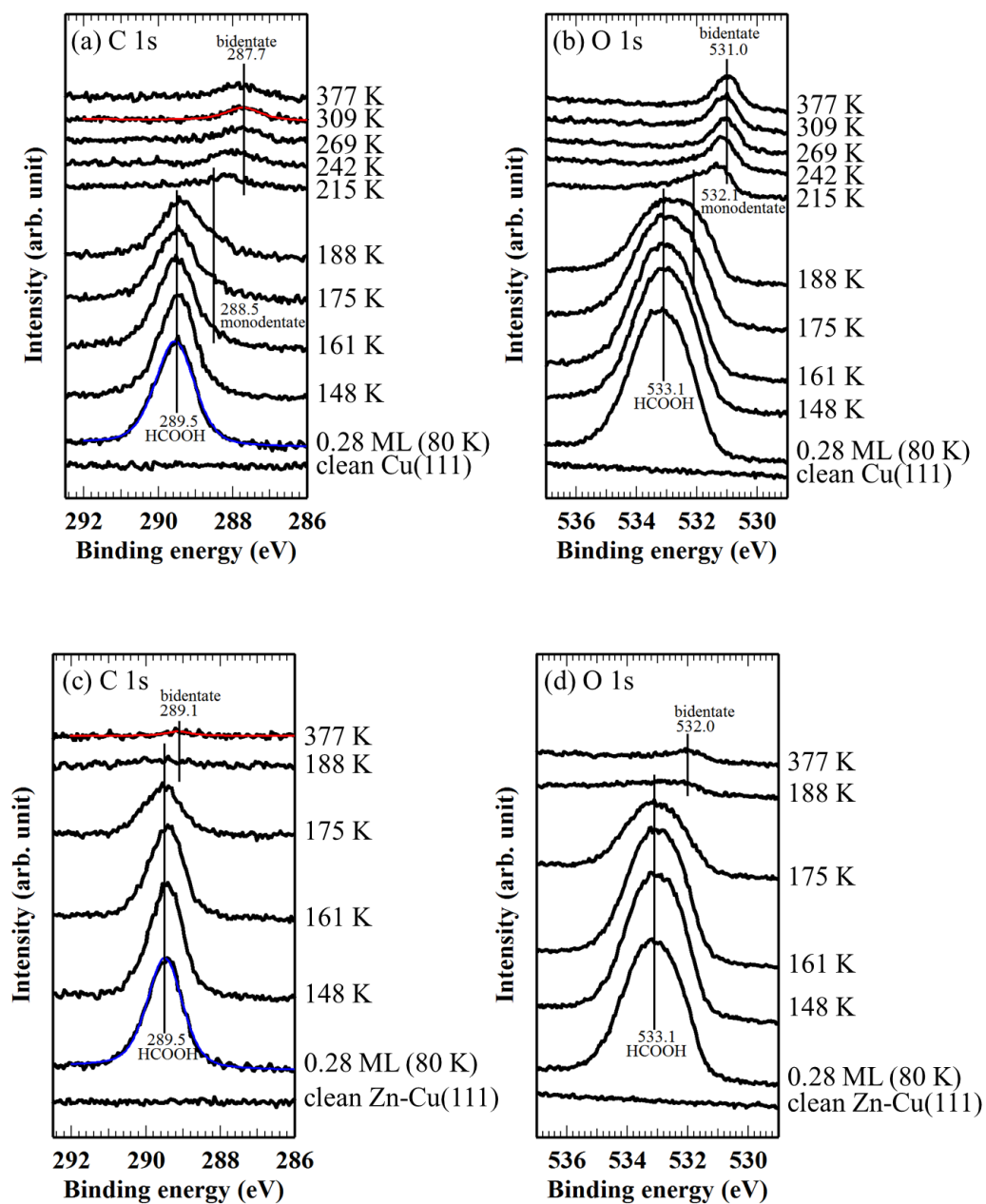


Figure 5.3. A series of (a) C 1s and (b) O 1s XPS spectra of HCOOH (0.28 ML) on Cu(111) at 80 K and subsequent annealing. A series of (c) C 1s and (d) O 1s XPS spectra of HCOOH (0.28 ML) on Zn (0.4 ML)-Cu(111) at 80 K and subsequent annealing. The spectra were measured using a photon energy of 630 eV.

Figure 5.4 shows a series of (a) C 1s and (b) O 1s XPS spectra of 0.28 ML HCOOH on Cu(997) at 83 K and subsequent annealing. Three peaks were observed at 289.8 (533.3), 288.4 (531.7) and 287.7 (531.0) eV for C 1s (O 1s) spectra. The peak at 289.8 (533.3) eV is assigned to molecular HCOOH adsorbed on Cu(997). The binding energies both C 1s and O 1s of HCOOH on Cu(997) were higher than Cu(111). This is probably due to the difference of adsorbed HCOOH structure which will be discussed later with IRAS measurements. A shoulder in the lower binding energy side at 288.4 (531.7) eV indicates the early dissociation from adsorbed HCOOH into monodentate formate species even at 83 K. The 13% of adsorbed HCOOH dissociated into the monodentate formate species on Cu(997), indicating that the stepped Cu surface has a higher reactivity for HCOOH dissociation at low temperature. After annealing the sample up to 160 K, adsorbed HCOOH peaks (C 1s: 289.8 and O 1s: 533.3 eV) gradually decreased and a monodentate formate peaks (C 1s: 288.4 and O 1s: 531.7 eV) slightly increased in intensity. With further heating at 300 K, the bidentate formate peaks were observed (C 1s: 287.7 eV and O 1s: 531.0 eV). The 17% of adsorbed HCOOH dissociated into the bidentate formate

species at 300 K. After heating to 500 K, all of the adsorbed species have desorbed from the Cu(997) surface.

Figure 5.4 shows a series of (c) C 1s and (d) O 1s XPS spectra of 0.28 ML HCOOH on Zn (0.4 ML)-Cu(997) at 82 K and subsequent annealing. At least two peaks were observed at 289.9 (533.4) and 288.9 (531.7) eV for C 1s (O 1s) spectra. The peak at 289.9 (533.4) eV is assigned to the first layer HCOOH on Zn-Cu(997). After heating up to 160 K, the adsorbed HCOOH peaks (C 1s: 289.9 eV and O 1s: 533.4 eV) gradually decreased and shoulder peaks (C 1s: 288.9 eV and O 1s: 531.7 eV) were observed. The peak at 288.9 (531.7) eV is assigned to the bidentate formate species on Zn-Cu(997), which remained after heating up to 450 K.

The 20% of adsorbed HCOOH dissociated into the bidentate formate species on Zn-Cu(997) at 300 K. The percentage of bidentate formate species for initial adsorbed HCOOH becomes increased in contrast to the results on Zn-Cu(111). When the Zn-Cu surface alloy is formed on Cu(997), the Zn atoms can locate at both the step sites and terrace sites. The Zn atoms located at the terrace site inactivated the HCOOH dissociation as shown Fig. 5.3. Thus, the Zn

atoms at the step sites have some reactivity for the HCOOH dissociation, which lead to increase the percentage of bidentate formate species.

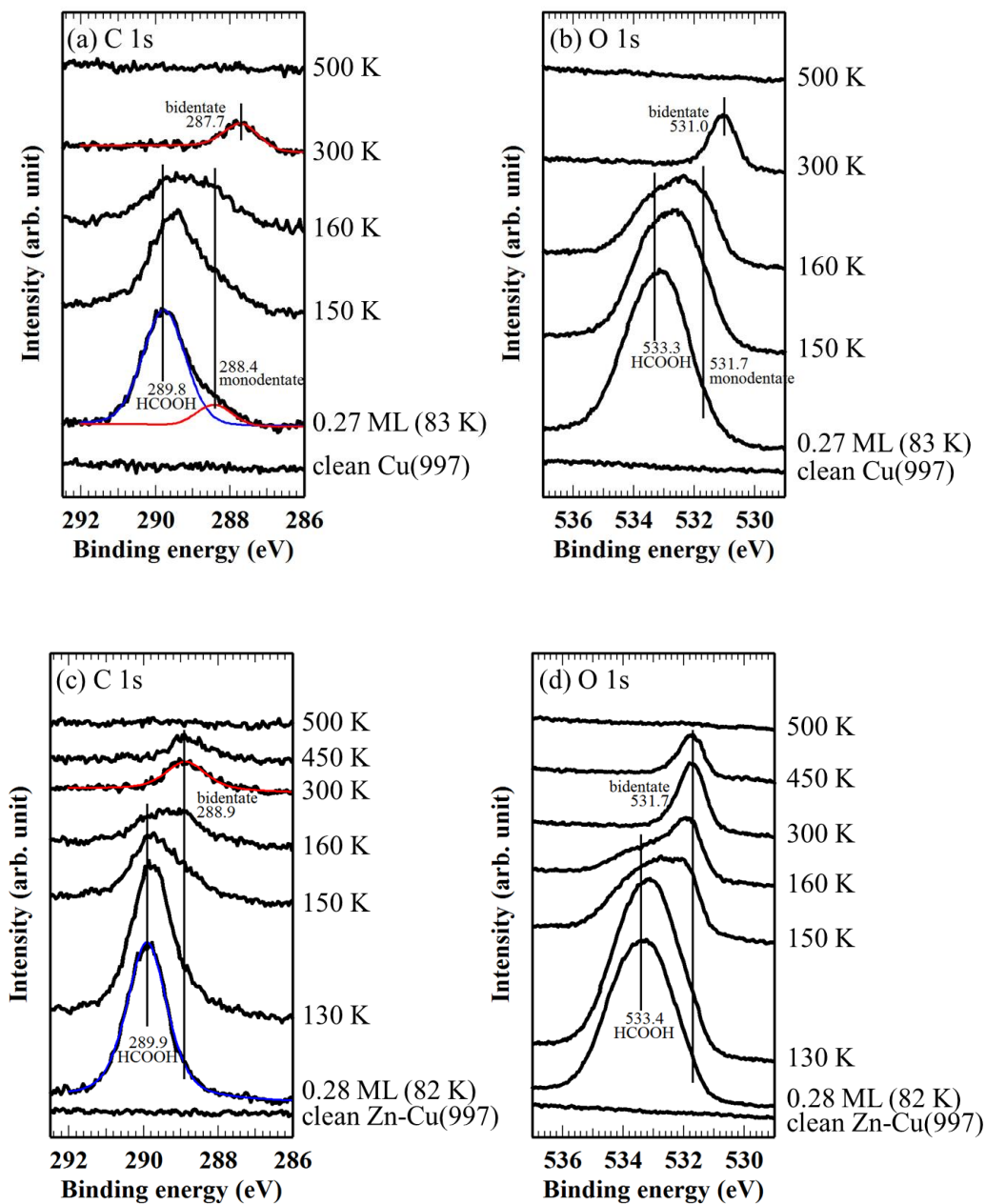


Figure 5.4. A series of (a) C 1s and (b) O 1s XPS spectra of HCOOH (0.27 ML) on Cu(997) at 83 K and subsequent annealing. A series of (c) C 1s and (d) O 1s XPS spectra of HCOOH (0.28 ML) on Zn (0.4 ML)-Cu(997) at 82 K and subsequent annealing. The spectra were measured using a photon energy of 630 eV.

The present XPS results show that the step site can play an important role in increasing the activity of adsorbed HCOOH dissociation. However, information for the orientation of adsorbates cannot be obtained from the XPS. In order to understand the dissociation of adsorbed HCOOH in detail, we carried out the TPD and IRAS measurements on Cu(997) and Zn-Cu(997) to compare with the results on Cu(111) and Zn-Cu(111).

Figure 5.5 shows multiplexed TPD spectra of HCOOH adsorbed on Cu(997) as a function of HCOOH exposure at 82 K. In Fig. 5.5 (a) and (b), the mass number 29 (HCO^+) is the major cracking fragment of HCOOH. At low HCOOH exposure (3~7 shots), a small peak was observed at 245 K in Fig. 5.5 (a). This desorption peak is assigned to adsorbed HCOOH at the Cu step sites because it was not observed on Cu(111). With increasing HCOOH exposure, the peak of the first layer HCOOH was observed at 172 K in Fig. 5.5 (b). The peaks of the first layer HCOOH (10~20 shots) have the different feature in comparison with the TPD spectra for HCOOH/Cu(111); the desorption peak maxima are not shifted with increasing HCOOH coverages. This feature indicates that the desorption order for molecular HCOOH should be first. This is probably due to the different structure of adsorbed HCOOH species; a hydrogen bonding

network is not well-developed on Cu(997) (as discussed later with IRAS measurements). The desorption peak maxima for the saturation coverage of the first layer HCOOH on Cu(111) and Cu(997) are 182 K and 172 K, respectively. The HCOOH adsorbed on Cu(111) needs more activation energy to desorb from the surface than the HCOOH adsorbed on Cu(997). We think this is due to the stabilization of adsorbed HCOOH via a hydrogen bonding network on Cu(111).^{43,44} The desorption peak at ~150 K was observed at higher HCOOH exposure (30 and 35 shots), which is assigned to adsorbed HCOOH of multilayer.

Fig. 5.5 (c) and (d) show the mass number 44 (CO_2^+) and 2 (H_2^+), respectively. We know that the present XPS measurements show that a part of adsorbed HCOOH desorbs molecularly from Cu(997) and the other HCOOH is dissociated into the formate and a hydrogen atom in Fig. 5.4 (a) and (b). In Fig. 5.5 (d), the dissociated hydrogen atoms were recombined and desorbed as H_2 at 327 K. The peaks at 327 K were gradually shifted to lower desorption temperature with increasing the peak intensity. This is assigned to the second order kinetics for the recombination desorption of hydrogen atoms.^{45,84} In Fig. 5.5 (c) and (d), the adsorbed formate species were decomposed, and H_2 and

CO₂ were immediately desorbed at 450 K. These observations are similar to the results on Cu(111).^{44,45}

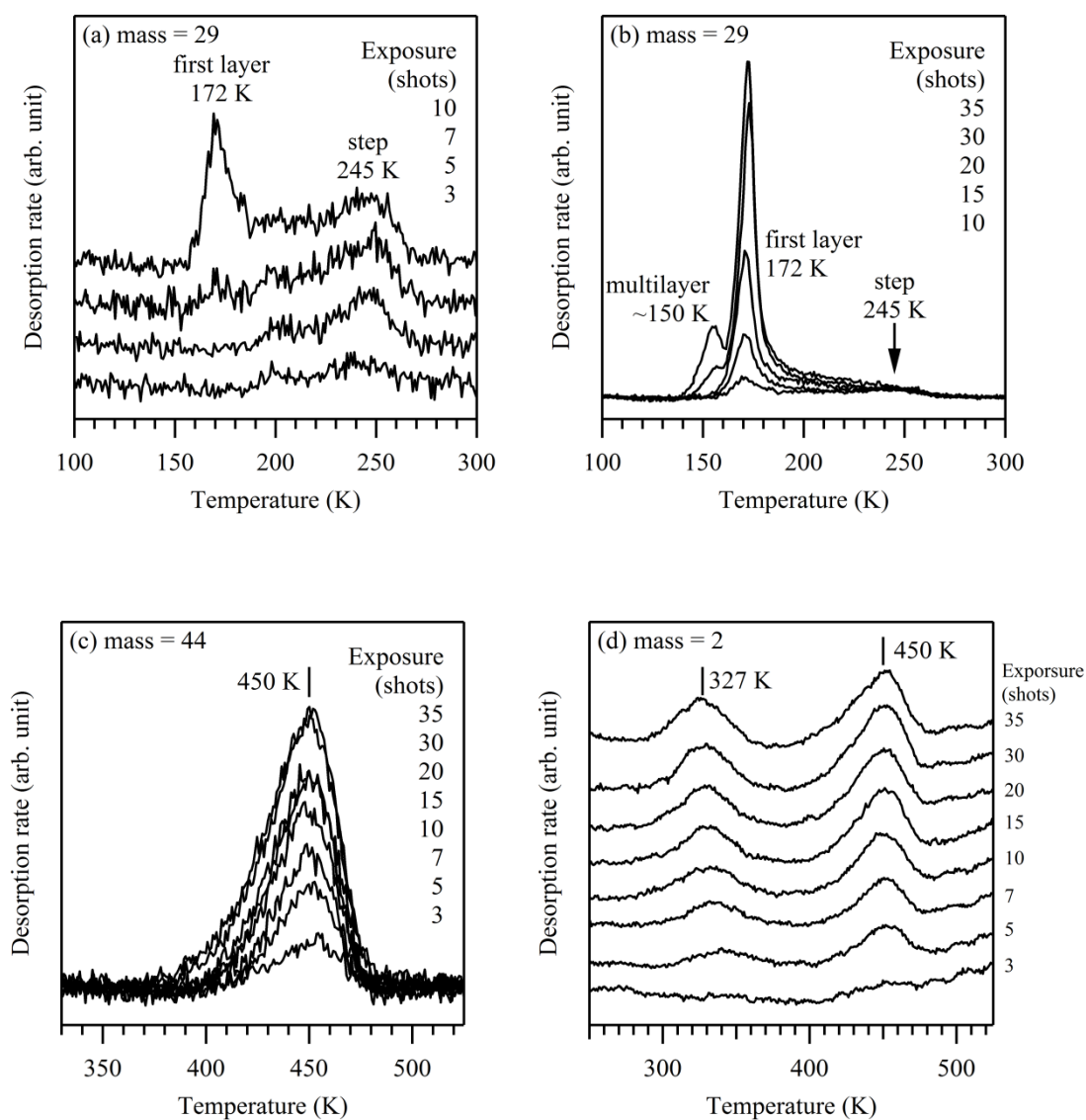


Figure 5.5. Multiplexed TPD spectra of HCOOH adsorbed on Cu(997) as a function of HCOOH exposure at 82 K. (a) mass = 29 (HCO⁺, the major cracking fragment of HCOOH) at lower HCOOH exposures (3~10 shots), (b) mass = 29 at higher HCOOH exposures (10~35 shots), (c) mass = 44 (CO₂⁺) and (d) mass = 2 (H₂⁺). The heating rate was 1 K/s.

In order to estimate the coverage of Zn on Zn-Cu(997), the titration was performed based on the saturated adsorption of CO on Zn-Cu(997).⁵⁷ Fig. 5.6 (a) shows multiplexed TPD spectra of CO (mass number 28: CO⁺) adsorbed on Zn-Cu(997) as a function of the coverage of Zn. Black line indicates the TPD spectra for CO saturation on the clean Cu(997) surface. The desorption peaks at 90~170 K are assigned to adsorbed CO at the terrace sites.⁵³ The desorption peaks at 170~210 K are assigned to adsorbed CO at the step sites. When Zn-Cu(997) alloyed surfaces were formed, these desorption peaks gradually decreased with increasing the coverage of Zn. This is due to the weakening of the bonds between CO and the Zn-Cu alloyed surface.⁵³ In addition, the Zn atoms locate at both the step sites and terrace sites. When the total integrated area for CO saturation on the clean Cu(997) surface is defined as 1 ML, the coverage of Zn is estimated from the decrease of integrated area for CO saturation on Zn-Cu(997).

Fig. 5.6 (b) shows multiplexed TPD spectra of Zn (mass number 64: Zn⁺) on Zn-Cu(997) as a function of the coverage of Zn. Two desorption peaks were observed at 620~580 and 550 K. According to the previous TPD measurements of Zn on Cu(111), the desorption peaks at low coverages of Zn were observed at

600~550 K (first layer).^{57,85} With increasing coverages of Zn, multilayer peaks of Zn were observed at 550~400 K.^{57,85} Therefore the desorption peak both 620~580 and 550 K are assigned to the first layer of Zn.^{57,85}

Fig. 5.6 (c) shows Zn coverage as a function of the integrated area of Zn desorption peak in Fig. 5.6 (b). The vertical axis indicates the coverage of Zn, which is defined as follows:

$$\theta_{Zn} = 1 - \frac{\text{Integrated area of CO saturation on Zn-Cu(997)}}{\text{Integrated area of CO saturation on clean Cu(997)}}$$

Integrated areas of CO saturation on clean Cu(997) or Zn-Cu(997) are estimated from Fig. 5.6 (a). In Fig. 5.6 (c), a linear dependency may indicate a 2-D growth mode of the first layer.⁵⁷ The coverages of Zn on Zn-Cu(997) in TPD and IRAS experiments were estimated by Fig. 5.6 (c).

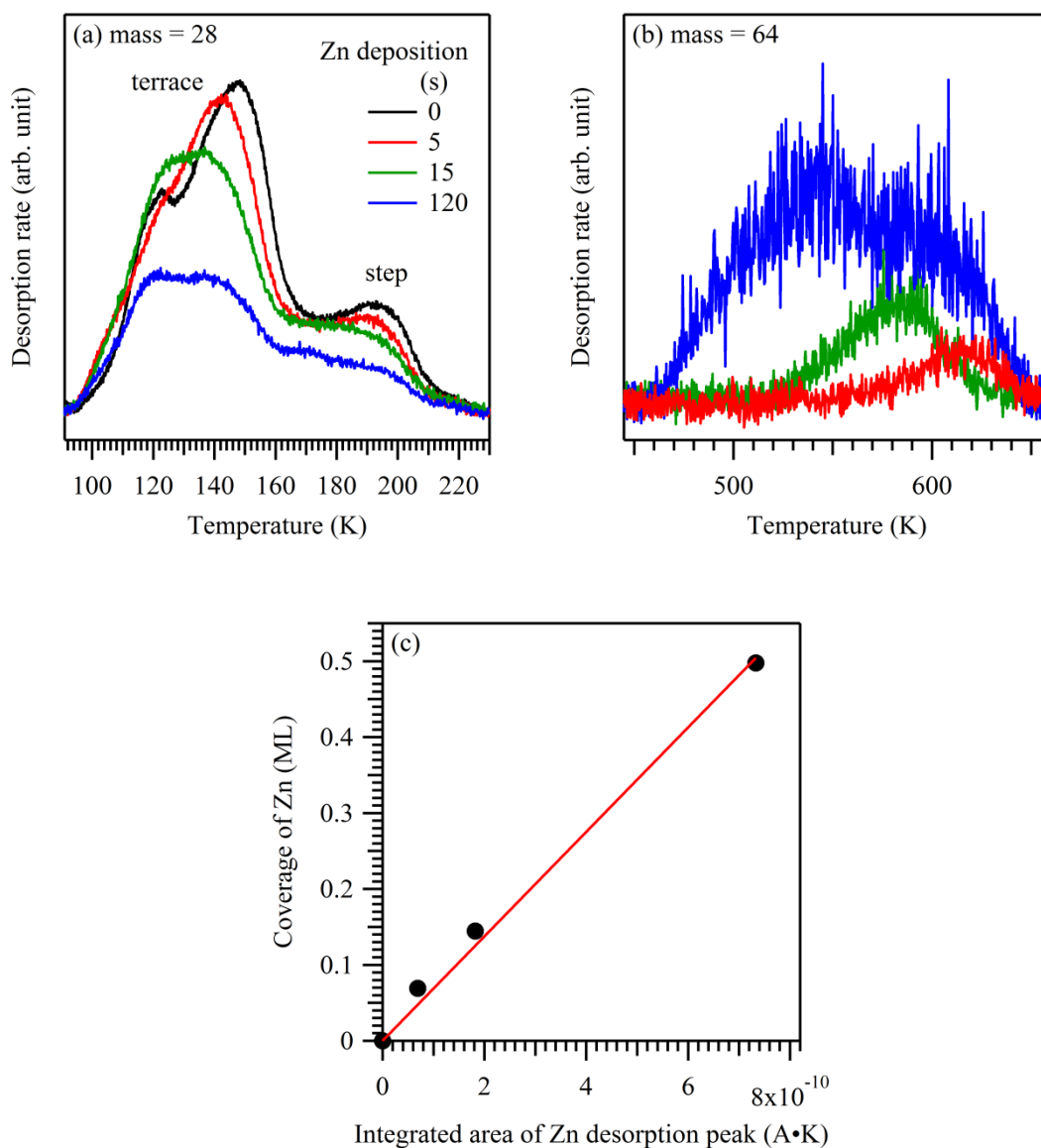


Figure 5.6. Multiplexed TPD spectra of CO adsorbed on Zn-Cu(997) as a function of the coverage of Zn. (a) mass = 28 (CO⁺), (b) mass = 64 (Zn⁺) and (c) Zn coverage as a function of the integrated area of Zn desorption peak. The heating rate was 1 K/s.

Figure 5.7 shows the multiplex TPD spectra of HCOOH adsorbed on Zn-Cu(997) as a function of HCOOH exposure at 82 K. Fig. 5.7 (a), (b), (c) and (d) originated from the same experiment. In Fig. 5.7 (a), three desorption peaks were observed at ~150, 170 and 230 K, which are assigned to adsorbed HCOOH of multilayer, the first layer on a terrace and step sites on Zn-Cu(997), respectively. The desorption peak maxima for adsorbed HCOOH of the first layer and step sites on Zn-Cu(997) were lower than Cu(997). As similar to the case on Cu(997), the desorption peak maxima of the first layer HCOOH were not shifted with increasing HCOOH coverages. This indicates that the desorption order for molecular HCOOH on Zn-Cu(997) should be first.

Fig. 5.7 (b) and (c) show TPD spectra for the mass number 44 (CO_2^+) and 2 (H_2^+), respectively. In Fig. 5.7 (c), the desorption temperature of H_2 for the recombining of hydrogen atoms (327 K) did not change in comparison with Cu(997). However, the decomposition and desorption temperatures of adsorbed formate species were 10 K higher than Cu(997) in Fig. 5.7 (b) and (c). This indicates that formate species is stabilized on the Zn-Cu alloyed surfaces. These results are important in terms of methanol synthesis reaction on the Zn-Cu

catalysts. The Zn can play an important role in the stabilization of reaction intermediates (i.e., formate species, etc.) on the Zn-Cu surface.⁷⁸

Fig. 5.7 (d) shows TPD spectra of the mass number 64 (Zn^+). Two desorption peaks were observed at ~600 and ~690 K. According to the previous TPD measurements of Zn on Cu(111) as shown in Fig. 5.8, the desorption peaks at low coverages of Zn were observed at 600~550 K (first layer).^{57,85} With increasing the coverage of Zn, multilayer peaks of Zn were observed at 550~400 K.^{57,85} Therefore the desorption peak at ~600 K in Fig. 5.7 (d) is assigned to the first layer of Zn.^{57,85} So far there is no report for TPD spectra of Zn on the Cu step surfaces. The desorption peak at ~690 K was observed when the Zn and formate species are co-adsorbed on Zn-Cu(997). The coverages of Zn were estimated to be 0.2 ML from Fig. 5.6 (c).

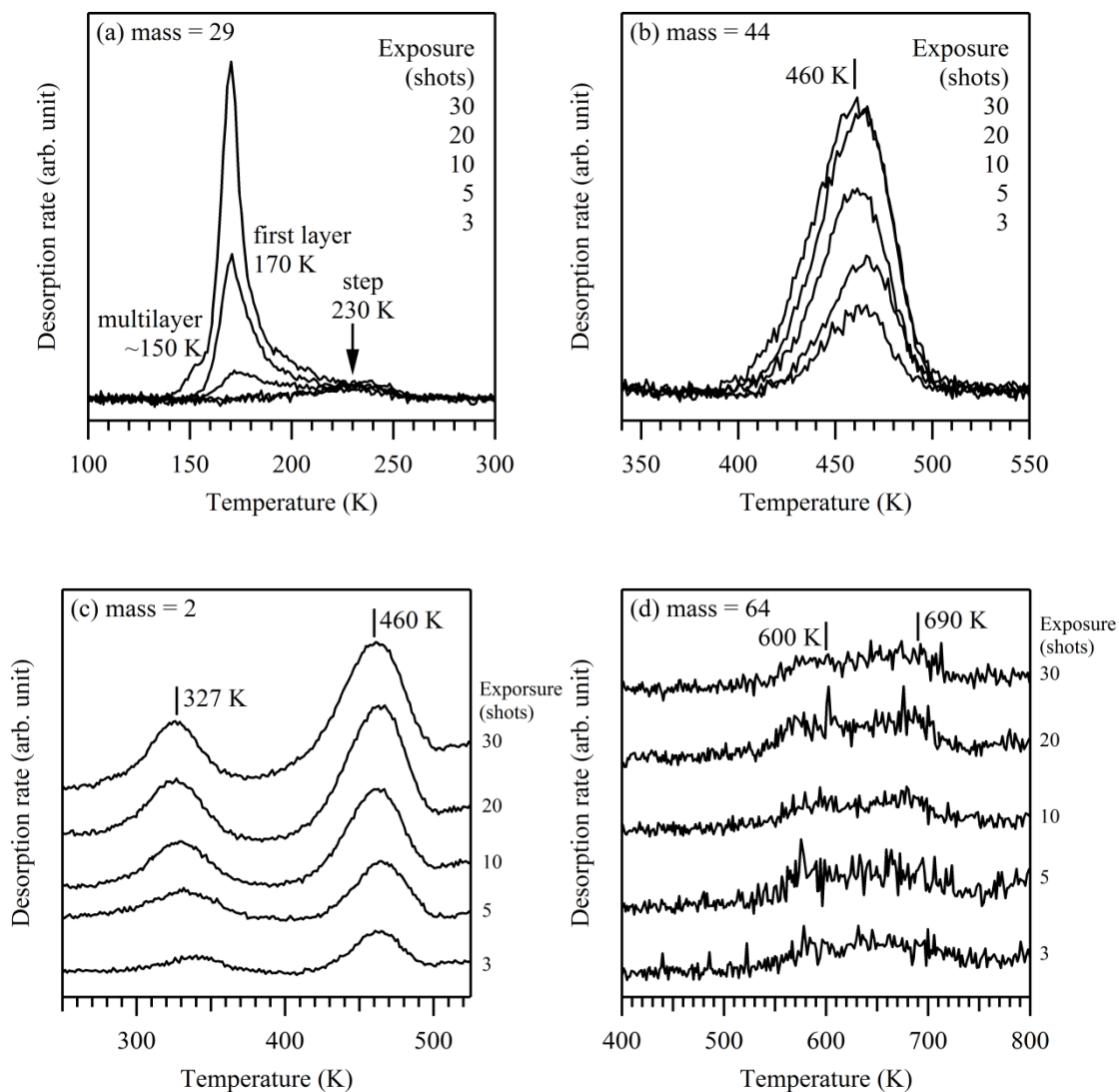


Figure 5.7. TPD spectra of HCOOH adsorbed on Zn-Cu(997) as a function of HCOOH exposure at 82 K. (a) mass = 29 (HCO^+ , the major cracking fragment of HCOOH), (b) mass = 44 (CO_2^+), (c) mass = 2 (H_2^+) and (d) mass = 64 (Zn^+). The heating rate was 1 K/s. $\theta_{\text{Zn}} = 0.2 \text{ ML}$.

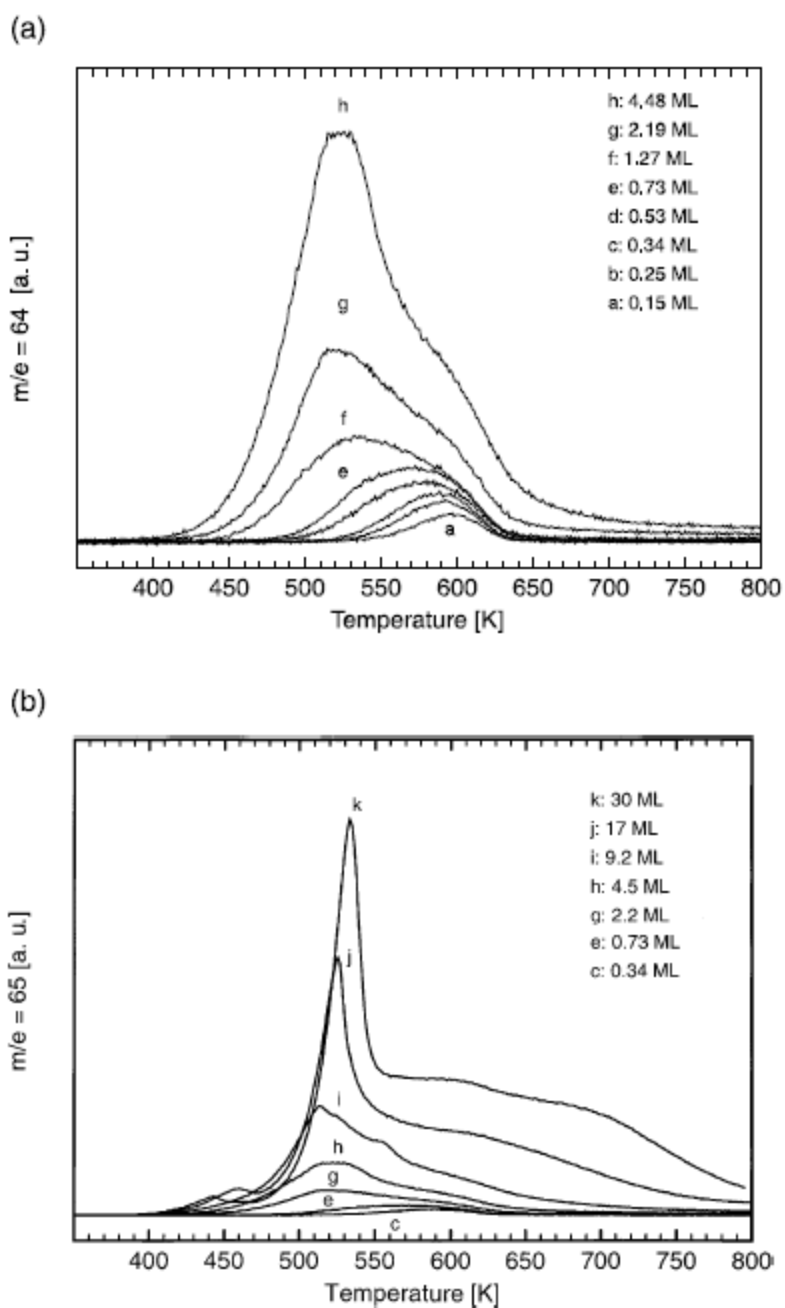


Figure 5.8. The previous study for TPD of Zn on Cu(111) as a function of the coverage of Zn. The heating rate was 5 K/s. (a) low coverages from 0.15 to 4.48 ML; (b) high coverages from 0.34 to 30 ML.⁵⁷

Figure 5.9 shows multiplex TPD spectra of 5 shots HCOOH (less than mono layer) adsorbed on Zn-Cu(997) at 82 K as a function of the Zn coverage. Black and blue lines indicate the TPD spectra for Zn of 0.2 ML and 1.9 ML, respectively. In Fig. 5.9 (a), broad desorption peaks of HCOOH adsorbed at the step sites were observed, and the desorption peak maximum was further shifted to lower temperature at a higher Zn coverage. On the other hand, the decomposition-limited desorption peaks of adsorbed formate species were further shifted to higher temperature in Fig. 5.9 (b) and (c). Thus, the adsorption energies of formate species must be increased at a higher Zn coverage. On the other hand, the desorption temperature of H₂ for the recombining of hydrogen atoms was shifted to lower temperature (300 K) in Fig. 5.7 (c). This is probably due to the lower adsorption energy of hydrogen on a Zn-Cu alloyed surface than that on a clean Cu surface. According to the previous TPD measurements of hydrogen from Zn(0001), the desorption peaks were observed at 306~319 K.^{86,87}

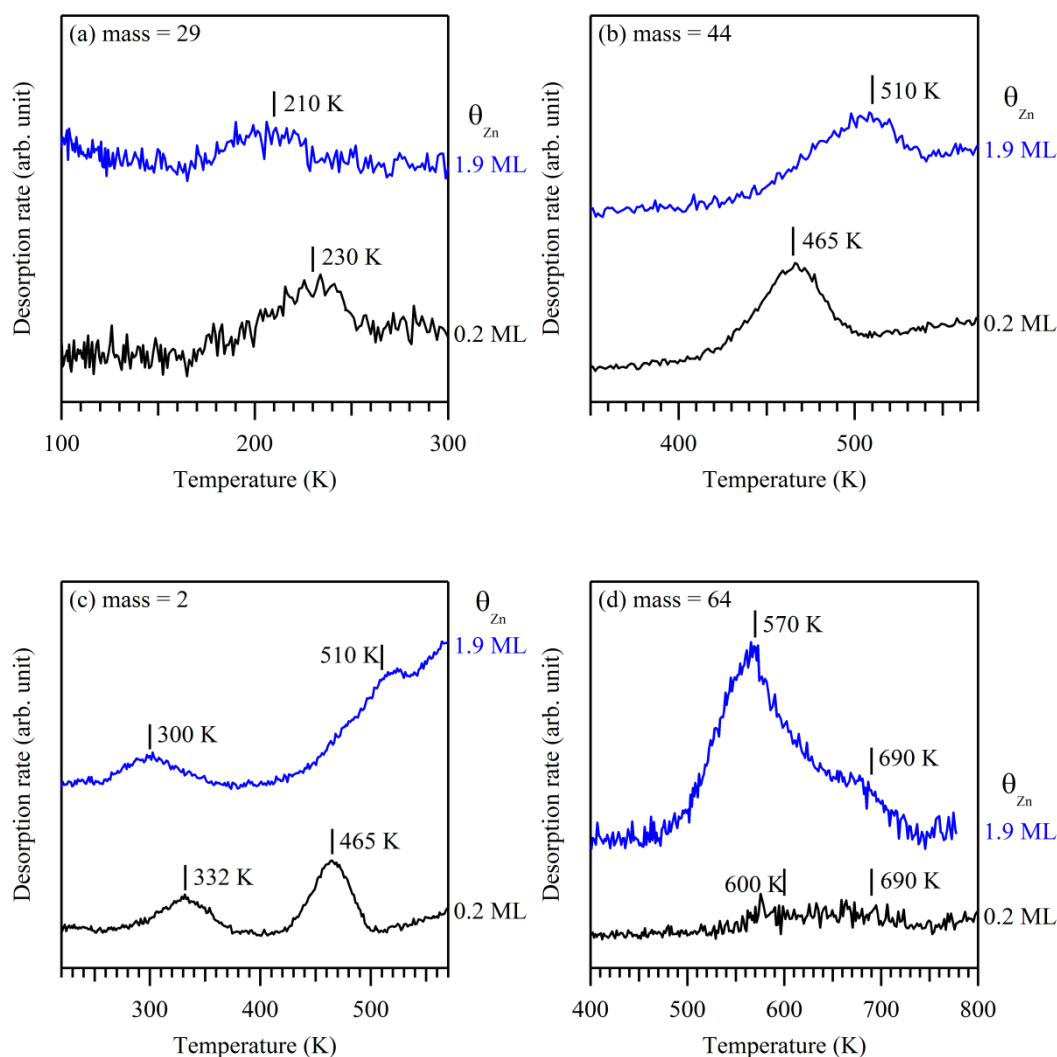


Figure 5.9. TPD spectra of 5 shots HCOOH adsorbed on Zn-Cu(997) at 82 K as a function of the Zn coverage. Black and blue lines indicate the spectra of 0.2 and 1.9 ML, respectively. (a) mass = 29 (HCO^+ , the major cracking fragment of HCOOH), (b) mass = 44 (CO_2^+), (c) mass = 2 (H_2^+) and (d) mass = 64 (Zn^+). The heating rate was 1 K/s.

Figure 5.10 (a) shows integrated area for HCOOH and CO₂ desorption peaks as a function of HCOOH exposure. With increasing HCOOH exposure, the integrated areas of HCOOH on Cu(997) or Zn-Cu(997) are gradually increased. In the exposure larger than 10 shots, the integrated area of HCOOH on Zn-Cu(997) is higher than that of Cu(997). At lower HCOOH exposure (3~5 shots), the intensity of each peak is too weak to analyze quantitatively. On the other hand, the integrated areas of CO₂ on Zn-Cu(997) are always higher than those of Cu(997).

Figure 5.10 (b) shows the ratio of the integrated area for CO₂ desorption peak to HCOOH desorption peak as a function of HCOOH exposure. It should be noted that at small exposures (<5 shots) the very small intensities as shown in Fig. 5.10 (a) induce a large error in the area ratio as mentioned above. At higher HCOOH exposure (7~35 shots), the ratio for Cu(997) or Zn-Cu(997) are gradually decreased. These results indicate that the branching ratio between the desorption and dissociation for adsorbed HCOOH has been changed by the initial coverage of HCOOH. With increasing the initial coverages of adsorbed HCOOH, the desorption becomes a predominant reaction. The ratio of CO₂/HCOOH is nearly saturated at 35 shots. The present TPD measurements of

HCOOH on Cu(997) show that the saturation coverage of the first layer HCOOH is 30 shots (Fig. 5.6). These results are similar to the present TR-IRAS measurements of HCOOH/Cu(111) in Fig. 4.9 and Fig. 4.10. The desorption of adsorbed HCOOH is a rate-limiting step for the dissociation from HCOOH to monodentate formate species at higher initial coverages of adsorbed HCOOH.⁴⁴ The branching ratio (CO_2/HCOOH) between 7 and 35 shots were higher than that on Cu(997). This is qualitatively consistent with the present XPS measurements of HCOOH adsorbed on Zn-Cu(997) (Fig. 5.4). The produced formate species on Zn-Cu(997) was 3% higher than Cu(997).

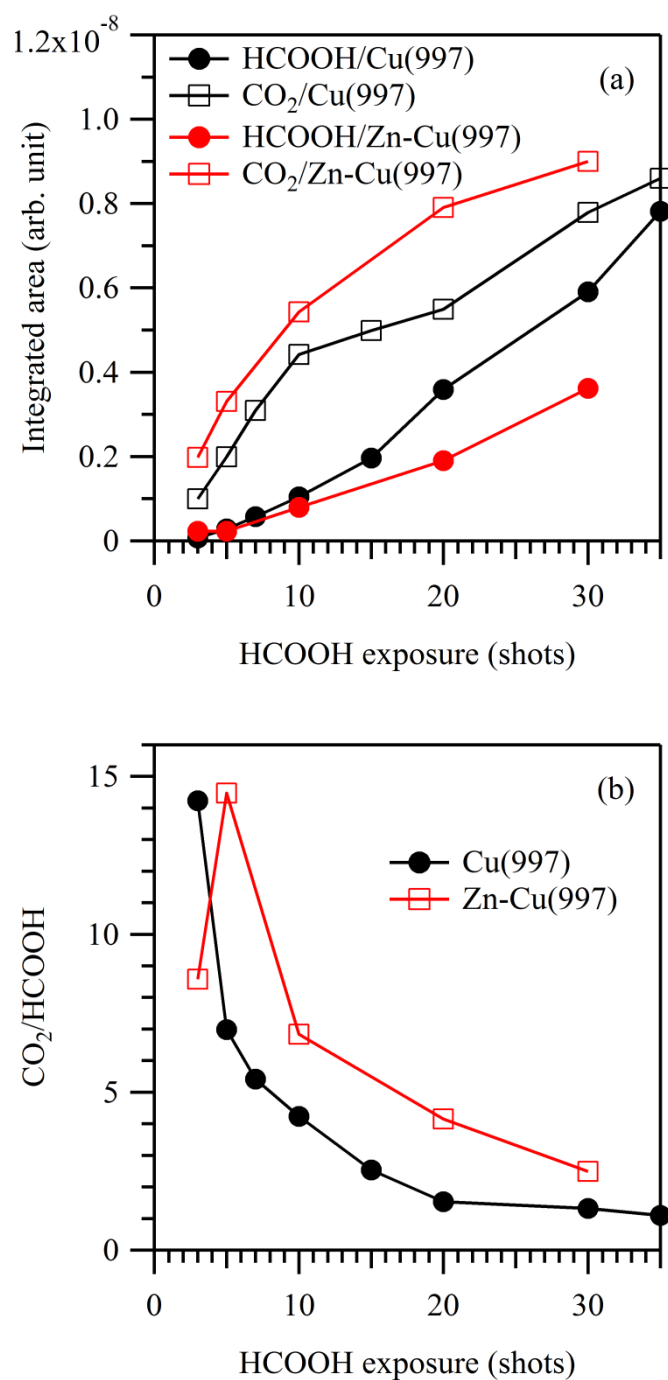


Figure 5.10 (a) Integrated area for HCOOH and CO₂ desorption peaks as a function of HCOOH exposure. (b) The ratio of the integrated for CO₂ desorption peak to HCOOH desorption peak as a function of HCOOH exposure.

Figure 5.11 (a) shows a series of IRAS spectra of HCOOH on Cu(997) at 82 K as a function of HCOOH exposure. Black and red dashed lines indicate the peaks of adsorbed species at the terrace and step sites, respectively. At HCOOH exposures up to 20 shots, six peaks were observed at 1713, 1672, 1654, 1630, 1384 and 1354 cm^{-1} . The peak assignments are summarized in Table 5.1. The peaks at 1713 and 1654 cm^{-1} on Cu(997) are close to the peaks at 1709⁴⁴ (1720⁴³) and 1655^{43,44} cm^{-1} on Cu(111), respectively. The peaks at 1713 and 1654 cm^{-1} on Cu(997) are assigned to the asymmetric OCO stretching modes, $\nu_{\text{as}}(\text{OCO})$, of the first layer HCOOH species and monodentate formate species on terrace sites, respectively. On the other hand, the peaks at 1672 and 1630 cm^{-1} originate from adsorbed species at the Cu step sites, and are assigned to the $\nu_{\text{as}}(\text{OCO})$ of HCOOH species and monodentate formate species, respectively.

At HCOOH exposures up to 10 shots, the peaks at 1672 (HCOOH at the step sites) and 1654 (monodentate formate on the terrace sites) cm^{-1} were observed. This indicates that the dissociation from adsorbed HCOOH to monodentate formate species occurs at the step sites and monodentate formate species diffuse to the terrace sites at 82 K. In fact, the previous STM

measurements show that low temperature (30 K) were necessary to visualize clean images at low coverages of HCOOH molecules on Cu(111).⁴³ The peaks at 1713 cm^{-1} (first layer HCOOH on the terrace sites) were observed above 15 shots. This originates from the saturation adsorption of HCOOH at the step sites. The amount of adsorbed HCOOH on the terrace sites is less stable than that at the step sites.

The peak at 1384 cm^{-1} on Cu(997) is close to the peak at 1388 cm^{-1} on Cu(111), which is assigned to an in-plane bending mode of $\delta(\text{C-H})$ of HCOOH species.⁴³ The $\delta(\text{C-H})$ peak at 1384 cm^{-1} was observed up to 241 K, and an only single vibrational energy was observed at the step and terrace sites. The $\delta(\text{C-H})$ peak was observed on Cu(111) when the adsorbed HCOOH was relatively higher coverages.^{43,44} However the $\delta(\text{C-H})$ peak on Cu(997) was observed even at lower exposures. If adsorbed HCOOH species are formed polymeric structures and adsorbed with its molecular plane parallel to the surface, the $\delta(\text{C-H})$ peak cannot be observed according to the surface-normal dipole selection rule for IRAS. Therefore, we think the HCOOH species are randomly orientated on Cu(997) without forming a 2-D hydrogen bonding network.

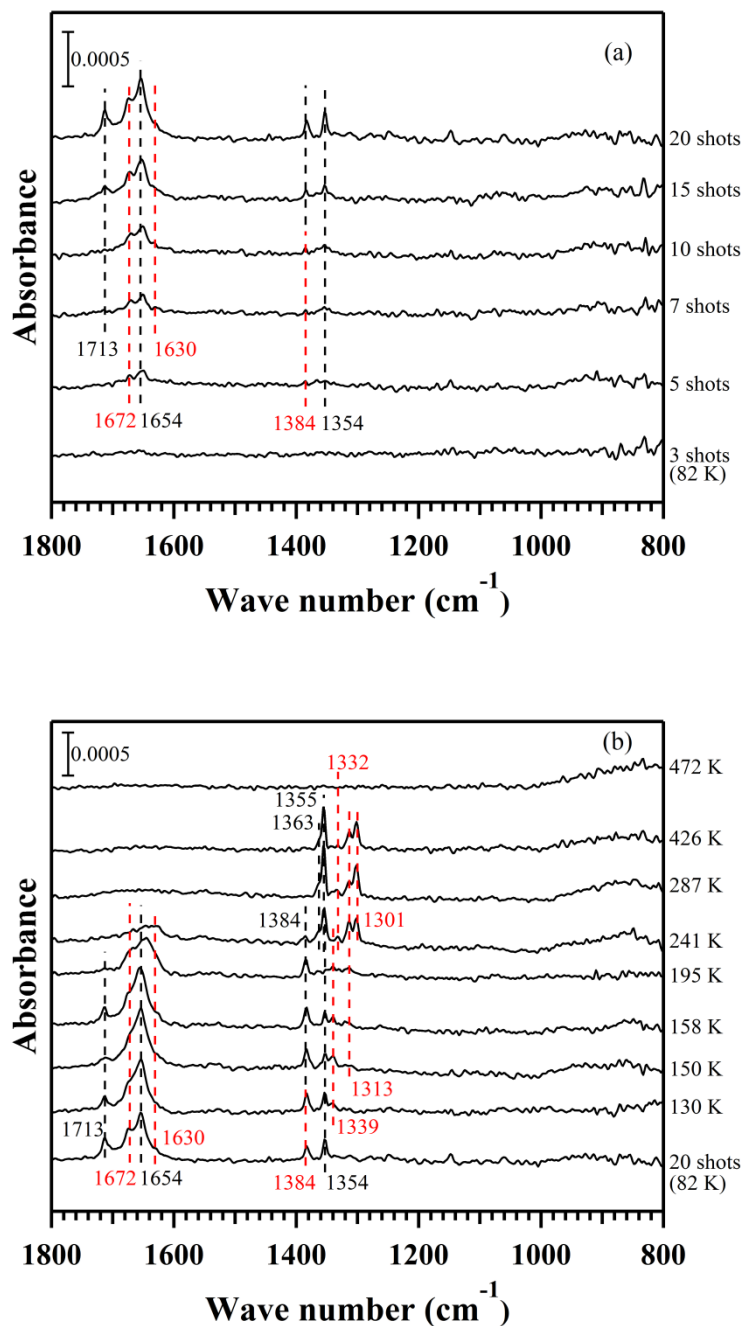


Figure 5.11. (a) A series of IRAS spectra of HCOOH on Cu(997) at 82 K as a function of HCOOH exposure. (b) A series of IRAS spectra of HCOOH (20 shots) on Cu(997) at 82 K and subsequent annealing. Black and red dashed lines indicate the peaks of adsorbed species at the terrace and step sites, respectively.

Table 5.1. Assignments of the observed vibrational peaks (cm^{-1}) of HCOOH and formate species.^{43,44}

Vibrational mode	Adsorption sites	Cu(997) (chapter 5)	Zn-Cu(997) (chapter 5)	Cu(111) (chapter 4) ⁴⁴	Cu(111) (reference ⁴³)
$\pi(\text{O-H})$	terrace	-	-	980 (HCOOH)	975 (HCOOH)
	step	-	-	-	-
$\pi(\text{C-H})$	terrace	-	-	1080 (HCOOH)	1084 (HCOOH)
	step	-	-	-	-
$\nu_s(\text{OCO})$	terrace	1363, 1355 (bidentate) 1354 (monodentate)	1364, 1351 (bidentate) 1354 (monodentate)	1360, 1345 (bidentate)	1357 (linked-formate) 1341 (bidentate)
	step	1339 (monodentate) 1332, 1313, 1301 (bidentate)	1339 (monodentate) 1335, 1301 (bidentate)	-	-
$\delta(\text{C-H})$	terrace	1384 (HCOOH)	1384 (HCOOH)	-	1388 (HCOOH)
	step	1384 (HCOOH)	1384 (HCOOH)	-	-
$\nu_{\text{as}}(\text{OCO})$ ($\nu(\text{C=O})$)	terrace	1654 (monodentate)	1654 (monodentate)	1655 (monodentate)	1655 (linked-formate)
	step	1630 (monodentate)	1646 (monodentate)	-	-
$\nu(\text{C=O})$	terrace	1713 (HCOOH)	1713 (HCOOH)	1709 (HCOOH)	1720 (HCOOH)
	step	1672 (HCOOH)	1672 (HCOOH)	-	-

ν : stretching mode, π : out-of-plane bending mode, δ : in-plane bending mode

Figure 5.11 (b) shows a series of IRAS spectra of HCOOH (20 shots) on Cu(997) at 82 K and subsequent annealing. Black and red dashed lines indicate the peaks of adsorbed species at the terrace and step sites, respectively. After heating up to 195 K, the peak at 1713 cm^{-1} (HCOOH on the terrace sites) completely disappeared. However the peak at 1672 cm^{-1} (HCOOH at the step sites) was observed after heating at 241 K. These results are consistent with the TPD results of HCOOH on Cu(997); adsorbed HCOOH species of the first layer and at step sites were desorbed from the surface at 172 and 250 K, respectively (Fig. 5.6). Monodentate formate species were adsorbed both the terrace (1654 cm^{-1}) and step (1630 cm^{-1}) sites up to 241 K.

The peaks at 1354 and 1339 cm^{-1} on Cu(997) are close to the peak at 1357 cm^{-1} on Cu(111), which are assigned to the symmetric stretching modes, $\nu_s(\text{OCO})$, of monodentate formate species (linked-formate) at the terrace and step sites, respectively.^{43,44} In addition, the peak at 1313 cm^{-1} was clearly observed at 150 K. This peak was not observed on Cu(111) and was remained up to 426 K. Thus, the peak at 1313 cm^{-1} originates from adsorbed species at step sites, and assigned to the $\nu_s(\text{OCO})$ of bidentate formate species. These results indicate that the monodentate formate species were formed at both the

terrace and step sites, and a part of monodentate formate species change to bidentate formate species at the step sites.

After heating up to 241 K, the peaks at 1384 ($\delta(\text{C-H})$ of HCOOH), 1354 ($\nu_s(\text{OCO})$ of monodentate formate species on the terrace sites) and 1339 ($\nu_s(\text{OCO})$ of monodentate formate species at the step sites) cm^{-1} decreased in intensity, and five peaks were observed at 1363 (a shoulder), 1355, 1332, 1313 and 1301 cm^{-1} . The peaks at 1363 and 1355 cm^{-1} are close to the peaks at 1360⁴⁴ and 1345⁴⁴ (1341⁴³) cm^{-1} on $\text{Cu}(111)$, respectively. These peaks at 1363 and 1355 are assigned to the $\nu_s(\text{OCO})$ of bidentate formate species on the terrace sites.⁴⁴ The peaks at 1313 and 1301 cm^{-1} originate from adsorbed species at the step sites, and are assigned to the $\nu_s(\text{OCO})$ of bidentate formate species. These two peaks were not observed on $\text{Cu}(111)$. The peak at 1313 cm^{-1} was observed above 150 K, indicating that a part of monodentate formate species are converted to bidentate formate species. The present TR-IRAS measurements show that the monodentate formate species are converted immediately to bidentate formate species if a Cu vacant site is obtained on $\text{Cu}(111)$ (Fig. 4.9).⁴⁴

The peak at 1332 cm^{-1} was observed up to 287 K. The $\nu_s(\text{OCO})$ peaks of monodentate formate species at $1600\sim 1700\text{ cm}^{-1}$ become very weak or not observed at 287 K. Therefore the peak at 1332 cm^{-1} may originate from bidentate formate species at the step sites; this peak has not been observed on Cu(111). However we cannot completely exclude the possibility of monodentate formate species because the vibrational energy of the monodentate formate species is also expected in this region.

Importantly, the both $\pi(\text{CH})$ (1080 cm^{-1}) and $\pi(\text{O-H})$ (980 cm^{-1}) peaks of polymeric HCOOH were not observed on Cu(997) in comparison with the present IRAS results on Cu(111) (Fig. 4.7). These peaks were not observed even after the $\nu_{as}(\text{OCO})$ peak of the first layer HCOOH species (1713 cm^{-1}) generated on Cu(997). This is due to the adsorption structure of HCOOH on Cu(997); a 2-D hydrogen bonding network of adsorbed HCOOH molecules is not well-developed to form the polymeric structures. In chapter 4, we discussed that the presence of a hydrogen bonding network stabilizes the HCOOH species and leads to a change into monodentate formate species on Cu(111). On the other hand, the Cu(997) surface shows the reactivity for HCOOH dissociation at low temperature without the stabilization of a 2-D hydrogen bonding network.

Figure 5.12 (a) shows a series of IRAS spectra of HCOOH on Zn-Cu(997) at 82 K as a function of HCOOH exposure. The coverage of Zn was estimated to be 0.2 ML judging from TPD of Zn after IRAS measurements. At HCOOH exposures up to 20 shots, six peaks were observed at 1713, 1672, 1654, 1646, 1384 and 1354 cm^{-1} . The peak assignments are summarized in Table 5.1. The peaks at 1713, 1672 and 1654 cm^{-1} on Zn-Cu(997) were observed as the same vibrational energies on Cu(997), which are assigned to the $\nu_{\text{as}}(\text{OCO})$ of the first layer HCOOH on the terrace sites, HCOOH at the step sites and monodentate formate species on the terrace sites, respectively.^{43,44} The peak at 1646 cm^{-1} assigned to monodentate formate species at the step sites has a different vibrational energy in comparison with that on the Cu(997) surface (1630 cm^{-1}). This is probably due to a local environmental effect at the Zn-Cu step sites. However the peak of monodentate formate species on the terrace sites (1654 cm^{-1}) was not shifted by the Zn-Cu alloying. This indicates that this monodentate formate species is adsorbed at a locally bare Cu site on the Zn-Cu(997) surface. We think that the step sites have a higher density of Zn than the terrace sites. The present TPD measurements on Zn-Cu(997) show that the desorption peaks of HCOOH are shifted to lower temperature sides, and the

peak shifts at the step sites are larger than the first layer HCOOH on the terrace sites (Fig. 5.7). The peaks at 1384 and 1354 cm^{-1} on Zn-Cu(997) were observed at the same vibrational energies on Cu(997). The peak at 1384 cm^{-1} is assigned to the $\delta(\text{C-H})$ of HCOOH species.⁴³ The peak at 1354 cm^{-1} is assigned to the $\nu_s(\text{OCO})$ of monodentate formate species at the Zn-Cu alloyed terrace site.^{43,44}

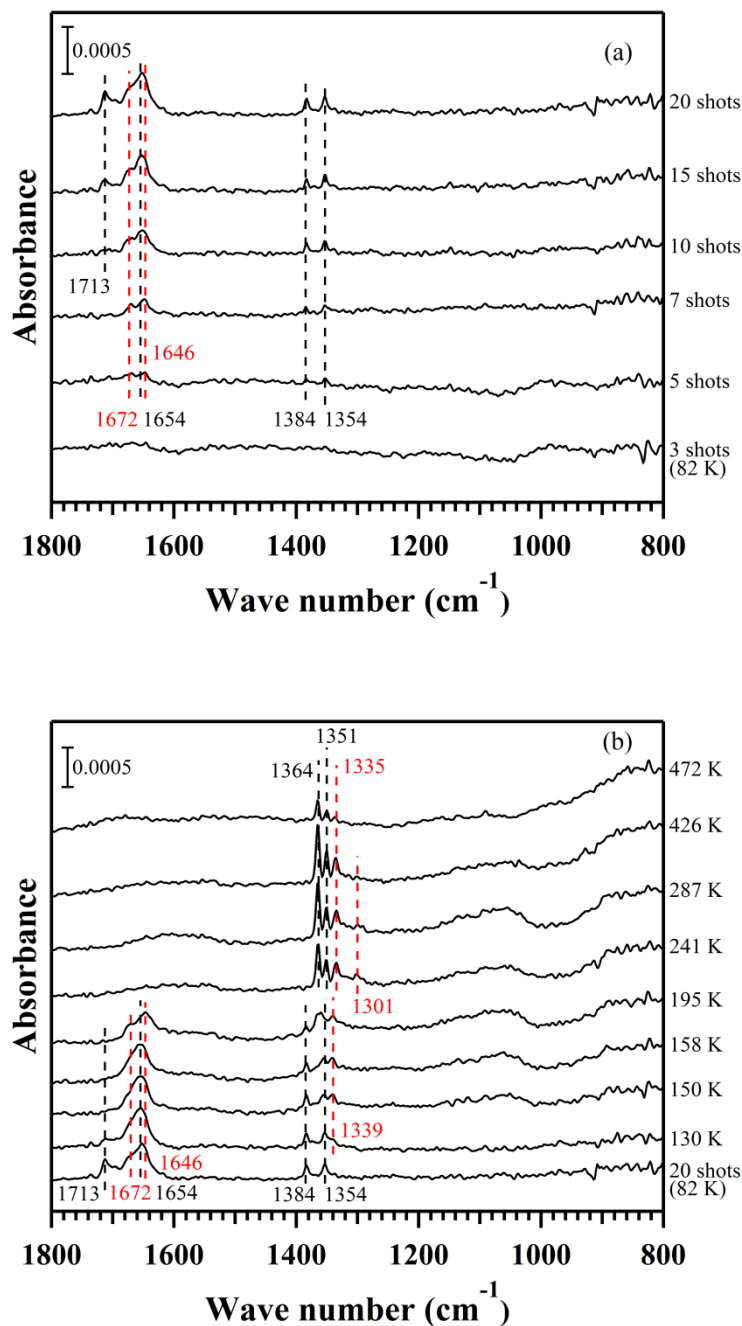


Figure 5.12. (a) A series of IRAS spectra of HCOOH on Zn-Cu(997) at 82 K as a function of HCOOH exposure. (b) A series of IRAS spectra of HCOOH (20 shots) on Zn-Cu(997) at 82 K and subsequent annealing. $\theta_{\text{Zn}} = 0.2$ ML. Black and red dashed lines indicate the peaks of adsorbed species at the terrace and step sites, respectively.

Figure 5.12 (b) shows a series of IRAS spectra of HCOOH (20 shots) on Zn-Cu(997) at 82 K and subsequent annealing. The peaks of adsorbed HCOOH for the first layer (1713 cm^{-1}) and step sites (1672 cm^{-1}) on Zn-Cu(997) disappeared at a lower annealing temperature than on Cu(997). This is consistent with the present TPD results (Fig. 5.6 and Fig. 5.7). After heating up to 195 K, the peaks of adsorbed HCOOH at the step sites (1672 cm^{-1}), monodentate formate species on the terrace sites (1654 cm^{-1}) and monodentate formate species at the step sites (1630 cm^{-1}) are still observed on Zn-Cu(997).

The peaks at 1384 , 1354 and 1339 cm^{-1} on Zn-Cu(997) were observed at the same vibrational energies on Cu(997). The peak at 1384 cm^{-1} is assigned to the $\delta(\text{C-H})$ of HCOOH species.⁴³ The peaks at 1354 and 1339 cm^{-1} are assigned to the $\nu_s(\text{OCO})$ of monodentate formate species at the Zn-Cu alloyed terrace and step sites, respectively.^{43,44} With heating up to 195 K, the peak of the monodentate formate species at the Zn-Cu alloyed step sites (1339 cm^{-1}) is increased in intensity. However the peak of the monodentate formate species at the Zn-Cu alloyed terrace sites (1354 cm^{-1}) did not change in contrast to the case on Cu(997). These results indicate that the monodentate formate species are stabilized at the Zn-Cu alloyed terrace sites. The present XPS and TPD

measurements show that the coverage of produced bidentate formate species on Zn-Cu(997) is higher than that on Cu(997) (Fig. 5.5 and Fig. 5.10 (b)). The stabilization of the monodentate formate species on Zn-Cu(997) leads to the increase of the produced bidentate formate species.

After heating up to 241 K, the peaks at 1384 ($\delta(\text{C-H})$ of HCOOH), 1354 ($\nu_s(\text{OCO})$ of monodentate formate on the terrace sites) and 1339 ($\nu_s(\text{OCO})$ of monodentate formate at the step sites) cm^{-1} decreased in intensity, and four peaks were observed at 1364, 1351, 1335 and 1301 cm^{-1} . The peak at 1301 cm^{-1} is assigned to the $\nu_s(\text{OCO})$ of bidentate formate species on Cu-step sites. This peak disappeared at 472 K, which is consistent with the IRAS results on Cu(997) (Fig. 5.11). The present TPD measurements show that a single desorption peak for formate decomposition is observed on Zn-Cu(997) (Fig. 5.7 (b)). These results indicate that the bidentate formate species are mobile on the surface at 423 K in order to access the Zn-Cu sites.

The peaks at 1364, 1351 and 1335 cm^{-1} are still observed after heating up to 472 K. The present TPD measurements show that the formate species remain on Zn-Cu(997) up to 500 K (Fig. 5.7 (b)). Therefore three peaks originate from

the bidentate formate species at the Zn-Cu alloyed sites. The peaks at 1364 and 1351 cm^{-1} on Zn-Cu(997) are close to the 1363 and 1355 cm^{-1} on Cu(997), respectively. The peaks at 1364 and 1351 cm^{-1} are assigned to the $\nu_s(\text{OCO})$ of bidentate formate species on the Zn-Cu terrace sites.^{43,44}

The peak at 1335 cm^{-1} on Zn-Cu(997) is close to the 1332 cm^{-1} on Cu(997), which is observed even after heating up to 472 K. Therefore the peak at 1335 cm^{-1} is assigned to bidentate formate species at the Zn-Cu step sites. The bidentate formate species at the Zn-Cu alloyed sites can be remained even at 472 K on Zn-Cu(997). The Zn on Cu surfaces plays a vital role in the stabilization of bidentate formate species on the Zn-Cu alloyed surface.

The IRAS experiments show that adsorbed HCOOH form a 2-D polymer on Cu(111) judging from the vibrational energy of $\pi(\text{O-H})$.^{43,44} A similar assignment has been reported previously on other metal substrate on Pt(111)⁷⁰ and Au(111)⁶⁹. In these studies, the structures of the first HCOOH layer are assigned to α -polymeric HCOOH by using vibrational spectroscopies such as IRAS and HREELS. On the other hand, Marcinkowski *et al.* reported that β -polymeric

HCOOH forms on Cu(111) by using a high-resolution STM.⁴⁵ We think that the morphology of adsorbed HCOOH depends on the experimental conditions such as the initial coverages of formic acid, sample temperature and surface structure. In fact, we elucidated that the dissociation kinetics for HCOOH adsorbed on Cu(111) depends on the initial coverage of adsorbed HCOOH. In addition, we also elucidated that a hydrogen bonding network of adsorbed HCOOH is not well-developed on Cu(997) from IRAS results. The Cu(997) surface has a close-packed terrace consists of nine atomic rows, and each terrace is separated by a monoatomic (111) step. We think that the formation of flat-lying polymeric HCOOH species is disturbed by the steps on Cu(997).

According to the present TPD results for HCOOH/Cu(997), the desorption of adsorbed HCOOH at Cu step site was observed at a higher temperature than that on Cu terrace site. The desorption of adsorbed HCOOH for the first layer was the first-order desorption. A similar result and kinetics for the desorption have been reported in the case of HCOOH/Au(997).⁸⁸ According to the present IRAS results for HCOOH/Cu(997), the peak of $\delta(\text{C-H})$ of HCOOH species (1384 cm^{-1}) was observed even at a submonolayer coverage. This indicates that the HCOOH molecules on Cu(997) are not adsorbed like α - and β -polymeric

HCOOH but are standing or tilted on the surface. On the other hand, the peak of $\delta(\text{C-H})$ of HCOOH species is observed on Cu(111) at a higher HCOOH exposure.^{43,44} This is due to the formation of condensed HCOOH phase.³⁸ If the first layer coverage reaches the saturation on Cu(111), the domain boundaries of adsorbed HCOOH species are formed which changes the orientation of a 2-D polymeric HCOOH.

We found that the dissociation of HCOOH on Cu(997) occurs even at 80 K. In addition, the coverage of formate species was increased when the Zn-Cu surface alloy was formed on Cu(997). According to the previous theoretical study, the activation barriers between intermediates for methanol synthesis reaction on Cu(211) are always lower than that on Cu(111).¹⁸ Alloying of Zn into the Cu(211)-step further increased the adsorption strength of HCOO, HCO, H₂CO, and H₃CO and decreased the activation barriers.¹⁸ We think that monodentate formate species on Cu(997) are stabilized at Cu step sites and which lead to decrease the activation energy between adsorbed HCOOH and monodentate formate species. The monodentate formate species are further stabilized at Zn-Cu step sites, when the Zn-Cu surface alloy is formed on

Cu(997). Thus, the coverage of produced formate species on Zn-Cu(997) becomes higher than that on Cu(997).

There are two important factors of Zn that affect the reaction of HCOOH on the Zn-Cu alloyed surfaces. The first one is a higher reactivity for the HCOOH dissociation at Zn-Cu step sites. This originates from a lower activation energy between adsorbed HCOOH and monodentate formate species at Zn-Cu step site. The second one is the stabilization of produced formate species on Zn-Cu alloyed surface. The produced bidentate formate species are a stable up to 500 K on the Zn-Cu(997) surface. We elucidated experimentally that the Zn can play a vital role in the stabilization of formate species on well-defined Zn-Cu step surfaces.

5.3 Conclusions

In chapter 5, we investigated the dissociation of a submonolayer HCOOH on Zn-Cu(111) and Zn-Cu(997) as well as clean Cu(111) and Cu(997) using high-resolution XPS, TPD and IRAS. The results are summarized in the list as follow.

- The order of the percentage of produced bidentate formate in initial adsorbed HCOOH was Zn-Cu(997): 20% > Cu(997): 17% > Cu(111): 13% > Zn-Cu(111): less than 4 %.
- The dissociation of HCOOH species adsorbed on Cu(997) were observed at 80 K.
- Adsorbed HCOOH molecules can be dissociated into monodentate formate species at step sites on Cu(997) without the stabilization of a 2-D hydrogen bonding network.
- The produced formate species are stabilized at Cu step sites and are further stabilized at Zn-Cu step sites.

Chapter 6

6.1 Concluding remarks

In this study, first, I investigated the desorption and decomposition kinetics of formic acid on Cu(111) using TPD, XPS and TR-IRAS. Secondly, I focused the decomposition reaction of formic acid on Zn-Cu(111) and Zn-Cu(997) as well as Cu(111) and Cu(997) using XPS, TPD and IRAS.

In chapter 4, the desorption and decomposition kinetics of formic acid on Cu(111) was investigated using TPD, XPS and TR-IRAS. Based on these experiments, I estimated the activation energies for desorption of formic acid (53-75 kJ/mol) and for dissociation from formic acid into monodentate formate species (65.0 kJ/mol) for the first time. The estimated values for the desorption are considerably large in comparison with the previous theoretical estimations on Cu(111); the theoretical adsorption energies were calculated to be 0.22 eV (21 kJ/mol)³⁵ and 0.24 eV (23 kJ/mol)³⁶. Note that these theoretical studies assumed an isolated formic acid molecule. However, in reality, adsorbed HCOOH species form a hydrogen bonding network on the Cu(111) surface.⁴³ On

the other hand, the activation energy from formic acid to bidentate formate was calculated to be 0.68 eV (66 kJ/mol)³⁵ and 0.61 eV (59 kJ/mol)³⁶. In the previous theoretical studies, no stable monodentate formate species on Cu(111) were found at a small coverage.³⁵ They noted that the coverage effects (lateral adsorbate-adsorbate interactions) can play an important role in determining the structural stability of various adsorbed states.³⁵ The adsorbed formic acid species in a hydrogen bonding network is more stable than an isolated formic acid molecule. Therefore, I have concluded that the hydrogen bonding network stabilizes the adsorption of formic acid and monodentate formate species.

In chapter 5, the decomposition reaction of formic acid on Zn-Cu(111) and Zn-Cu(997) as well as Cu(111) and Cu(997) were investigated using XPS, TPD and IRAS. The both $\pi(\text{CH})$ and $\pi(\text{O-H})$ peaks of polymeric formic acid were not observed on Cu(997) in comparison with the present IRAS results on Cu(111). This must originate from the adsorption structure of formic acid on Cu(997); a 2-D hydrogen bonding network of adsorbed formic acid molecules is not well-developed to form the polymeric structures. However, the Cu(997) has the reactivity for formic acid dissociation at 80 K, and adsorbed formic acid can be dissociated into monodentate formate species without the stabilization of a

hydrogen bonding network. We concluded that the monodentate formate species on Cu(997) are stabilized at Cu step sites and which lead to decrease the activation energy between adsorbed HCOOH and monodentate formate species. The Zn-Cu alloying effect on Zn-Cu(997) is clearly observed by TPD and IRAS measurements. The bidentate formate species at the Zn-Cu alloyed sites can be remained even at 472 K on Zn-Cu(997). We elucidated that the formate species are further stabilized at Zn-Cu step sites.

In conclusion, this thesis has elucidated the reaction mechanism of formic acid on copper model catalysts using modern surface spectroscopies. The structure of the Cu surface affects the adsorption structure of formic acid and the subsequent dissociation to monodentate formate species. In addition, an alloying effect is important in the stabilization of the produced formate species. The role of Zn will provide important information for methanol synthesis reaction on the Zn-Cu catalysts.

6.2 Future perspective

There are several issues that should be studied by using surface spectroscopies in more detail.

- (1) Microscopic adsorption structures of formic acid on the Cu(111) and Cu(997) surfaces.
- (2) Microscopic adsorption sites of Zn on the Zn-Cu(997) surface.
- (3) Microscopic adsorption structures and sites of formate species on the Cu(997) and Zn-Cu(997) surfaces.
- (4) Real-time observation of the intermediates (i.e., formate species) from CO₂ and H₂ on Zn-Cu surface alloy under high pressure and high temperature conditions.

The issues of (1), (2) and (3) can be directly elucidated by high resolution scanning probe microscopy (SPM). The adsorption structure of polymeric formic acid is not fully elucidated yet. In the previous studies, there are no microscopic observations of the first layer HCOOH at step sites. We have not figure out the origin of the multiple IRAS peaks for bidentate formate species on Cu(997). High resolution STM and atomic force microscopy (AFM) are powerful tools for

investigating the adsorption structures of adsorbate and substrate. We have already started the collaborative research by high resolution AFM. On the other hand, the issue of (4) can be elucidated by high pressure experiments such as the ambient pressure X-ray photoelectron spectroscopy (AP-XPS) using synchrotron radiation. The experimental condition in UHV is far from a real situation for catalysis. In order to elucidate the catalytic reaction, it is important to observe in-situ for the catalytic surface operating in the ambient condition. We introduced AP-XPS apparatus at the soft X-ray undulator beamline BL07LSU of SPring-8, and have started the investigation on activation and hydrogenation of CO₂.⁴⁸ Based on these experimental results, detailed mechanism between intermediates for methanol synthesis reaction will be clarified in the future.

References

- ¹ N. Schumacher, A. Boisen, S. Dahl, A.A. Gokhale, S. Kandoi, L.C. Grabow, J.A. Dumesic, M. Mavrikakis, and I. Chorkendorff, *Journal of Catalysis*, **229**, 265 (2005).
- ² A. Dibenedetto, A. Angelini, and P. Stufano, *Journal of Chemical Technology and Biotechnology*, **89**, 334 (2014).
- ³ P.J. Berlowitz and D.W. Goodman, *Journal of Catalysis*, **108**, 364 (1987).
- ⁴ K.-H. Ernst, C.T. Campbell, and G. Moretti, *Journal of Catalysis*, **134**, 66 (1992).
- ⁵ K.C. Waugh, *Catalysis Today*, **15**, 51 (1992).
- ⁶ V. Ponec, *Surface Science*, **272**, 111 (1992).
- ⁷ P.B. Rasmussen, M. Kazuta, and I. Chorkendorff, *Surface Science*, **318**, 267 (1994).
- ⁸ P. Rasmussen, P. Holmblad, and T. Askgaard, *Catalysis Letters*, **26**, 373 (1994).
- ⁹ T. Fujitani, M. Saito, Y. Kanai, T. Kakumoto, T. Watanabe, J. Nakamura, and T. Uchijima, *Catalysis Letters*, **25**, 271 (1994).
- ¹⁰ J. Yoshihara, S.C. Parker, A. Schafer, and C.T. Campbell, *Catalysis Letters*, **31**, 313 (1995).
- ¹¹ D.B. Clarke and A.T. Bell, *Journal of Catalysis*, **154**, 314 (1995).
- ¹² J. Yoshihara and C.T. Campbell, *Journal of Catalysis*, **161**, 776 (1996).
- ¹³ J. Nakamura, Y. Kushida, Y. Choi, T. Uchijima, and T. Fujitani, *J. Vac. Sci. Technol., A* **15**, 1568 (1997).
- ¹⁴ J. Nerlov and I. Chorkendorff, *Journal of Catalysis*, **181**, 271 (1999).
- ¹⁵ H. Nakano, I. Nakamura, T. Fujitani, and J. Nakamura, *The Journal of Physical Chemistry B*, **105**, 1355 (2001).
- ¹⁶ W. Jansen, J. Beckersb, J.C. v. d. Heuvelb, A.W.D. v. d. Gona, A. Bliiekb, and H.H.

Brongersmaa, *Journal of Catalysis*, **210**, 229 (2002).

¹⁷ J. Nakamura, Y. Choi, and T. Fujitani, *Topics in Catalysis*, **22**, 277 (2003).

¹⁸ M. Behrens, F. Studt, I. Kasatkin, S. Kühn, M. Hävecker, F. Abild-Pedersen, S. Zander, F. Girgsdies, P. Kurr, B.-L. Kniep, M. Tovar, R.W. Fischer, J.K. Nørskov, and R. Schlögl, *Science*, **336**, 893 (2012).

¹⁹ Y. Yang, C.A. Mims, R.S. Disselkamp, C.H.F. Peden, and C.T. Campbell, *Topics in Catalysis*, **52**, 1440 (2009).

²⁰ D.B. Clarke and A.T. Bell, *Journal of Catalysis*, **154**, 314 (1995).

²¹ I.E. Wachs and R. J. Madix, *Journal of Catalysis*, **53**, 208 (1978).

²² I.E. Wachs and R. J. Madix, *Applications of Surface Science*, **5**, 426 (1980).

²³ J.N. Russell, J.S.M. Gates, and J.T.Y. Jr., *Surface Science*, **163**, 516 (1985).

²⁴ G.C. Chinchin, P.J. Denny, J.R. Jennings, M.S. Spencer, and K.C. Waugh, *Applied Catalysis*, **36**, 1 (1988).

²⁵ R. Burch and S.E. Golunski, *Catalysis Letters*, **5**, 55 (1990).

²⁶ I. Chorkendorff, P.A. Taylor, and P. B. Rasmussen, *Journal of Vacuum Science & Technology A: Vacuum, Surfaces, and Films*, **10**, 2277 (1992).

²⁷ K.-H. Erunst, C.T. Campbell, and G. Moretti, *Journal of Catalysis*, **134**, 66 (1992).

²⁸ T.S. Askgaard, J.K. Nørskov, C. V. Ovesen, and P. Stoltze, *Journal of Catalysis*, **156**, 229 (1995).

²⁹ T. Fujitani, I. Nakamura, T. Uchijima, and J. Nakamura, *Surface Science*, **383**, 285 (1997).

³⁰ T. Fujitani, I. Nakamura, S. Ueno, T. Uchijima, and J. Nakamura, *Applied Surface Science*, **121/122**, 583 (1997).

³¹ X. Qi and M. Flytzani-stephanopoulos, *Industrial & Engineering Chemistry Research*, **43**, 3055 (2004).

- ³² N. Schumacher, A. Boisen, S. Dahl, A.A. Gokhale, S. Kandoi, L.C. Grabow, J.A. Dumesic, M. Mavrikakis, and I. Chorkendorff, *Journal of Catalysis*, **229**, 265 (2005).
- ³³ A.A. Gokhale, J.A. Dumesic, and M. Mavrikakis, *J. Am. Chem. Soc.*, **130**, 1402 (2008).
- ³⁴ G. Wang, Y. Morikawa, T. Matsumoto, and J. Nakamura, *Journal of Physical Chemistry B*, **110**, 9 (2006).
- ³⁵ L.C. Grabow and M. Mavrikakis, *ACS Catalysis*, **1**, 365 (2011).
- ³⁶ Y. Zhao, Y. Yang, C. Mims, C.H.F. Peden, J. Li, and D. Mei, *Journal of Catalysis*, **281**, 199 (2011).
- ³⁷ M. Bowker and R.J. Madix, *Surface Science*, **102**, 542 (1981).
- ³⁸ M. Bowker, S. Haq, R. Holroyd, P.M. Parlett, S. Poulston, and N. Richardson, *J. Chem. Soc., Faraday Trans.*, **92**, 4683 (1996).
- ³⁹ B.E. Hayden, K. Prince, D.P. Woodruff, A.M. Bradshaw, D.P. Woodruff, and A.M. Bradshaw, *Surface Science*, **133**, 589 (1983).
- ⁴⁰ F.C. Henn, J.A. Rodriguez, and C.T. Campbell, *Surface Science*, **236**, 282 (1990).
- ⁴¹ B.A. Sexton, *Surface Science*, **88**, 319 (1979).
- ⁴² D.H.S. Ying and R.J. Madix, *Journal of Catalysis*, **61**, 48 (1980).
- ⁴³ A.E. Baber, K. Mudiyansele, S.D. Senanayake, A. Beatriz-Vidal, K.A. Luck, E.C.H. Sykes, P. Liu, J.A. Rodriguez, and D.J. Stacchiola, *Phys. Chem. Chem. Phys.*, **15**, 12291 (2013).
- ⁴⁴ Y. Shiozawa, T. Koitaya, K. Mukai, S. Yoshimoto, and J. Yoshinobu, *The Journal of Chemical Physics*, **143**, 234707 (2015).
- ⁴⁵ M.D. Marcinkowski, C.J. Murphy, M.L. Liriano, N.A. Wasio, F.R. Lucci, and E.C.H. Sykes, *ACS Catalysis*, **5**, 7371 (2015).
- ⁴⁶ H. Nishimura, T. Yatsu, T. Fujitani, T. Uchijima, and J. Nakamura, *Journal of Molecular Catalysis A: Chemical*, **155**, 3 (2000).

- ⁴⁷ Y. Kim, T.S.B. Trung, S. Yang, S. Kim, and H. Lee, *ACS Catalysis*, **6**, 1037 (2016).
- ⁴⁸ T. Koitaya, S. Yamamoto, Y. Shiozawa, and K. Takeuchi, *Topics in Catalysis*, **59**, 526 (2016).
- ⁴⁹ F. Muttaqien, Y. Hamamoto, K. Inagaki, Y. Morikawa, F. Muttaqien, and Y. Hamamoto, *The Journal of Chemical Physics*, **141**, 034702, (2014).
- ⁵⁰ M.L. Ng, F. Abild-Pedersen, S. Kaya, F. Mbuga, H. Ogasawara, and A. Nilsson, *Physical Review Letters*, **114**, 246101 (2015).
- ⁵¹ J. Yoshinobu, K. Mukai, and T. Katayama, *Review of Scientific Instruments*, **79**, 2008 (2008).
- ⁵² A. Beniya, Ph.D. thesis, "Adsorption, Desorption and Thin Film Growth of Water Molecules on the Rh(111) Surface", The University of Tokyo (2007).
- ⁵³ W. Kirstein, B. Krüger, and F. Thieme, *Surface Science*, **176**, 505 (1986).
- ⁵⁴ B.J. Hinch and L.H. Dubois, *The Journal of Chemical Physics*, **96**, 3262 (1992).
- ⁵⁵ A. Toyoshima, T. Kikuchi, H. Tanaka, K. Mase, K. Amemiya, and K. Ozawa, *Journal of Physics: Conference Series*, **425**, 152019 (2013).
- ⁵⁶ T. Koitaya, Y. Shiozawa, K. Mukai, S. Yoshimoto, J. Yoshinobu, T. Koitaya, Y. Shiozawa, K. Mukai, S. Yoshimoto, and J. Yoshinobu, *The Journal of Chemical Physics*, **144**, 54703 (2016).
- ⁵⁷ C. Ammon, G. Held, J. Pantförder, and H.-P. Steinrück, *Surface Science*, **482–485**, 886 (2001).
- ⁵⁸ T. Koitaya, Y. Shiozawa, Y. Yoshikura, K. Mukai, S. Torii, F. Muttaqien, Y. Hamamoto, K. Inagaki, Y. Morikawa, and J. Yoshinobu, Submitted to *Surface Science* (2016).
- ⁵⁹ B. E. Hayden, Ch. 7 Reflection Absorption Infrared Spectroscopy, in J. T. Yates Jr. and T. E. Madey (Ed.) *Vibrational Spectroscopy of Molecules on Surfaces* (Plenum Press, New York) (1987).
- ⁶⁰ A. M. Bradshaw and E. Schweizer, Ch. 8 Infrared Reflection-Absorption Spectroscopy of Adsorbed Molecules, in R. J. H. Clark and R. E. Hester (Ed.) *Advances in Spectroscopy*:

Spectroscopy of Surfaces (Willey, New York) (1988).

⁶¹R. Ryberg, Infrared Spectroscopy of Molecules Adsorbed on Metal Surfaces p.1-, in K. P. Lawley (Ed.) Advances in Chemical Physics: Molecule Surface Interactions (Willey, New York) (1989).

⁶²S. Hüfner, Photoelectron Spectroscopy (Springer, Berlin) Third Ed (2003).

⁶³P.S. Bagus, F. Illas, G. Pacchioni, and F. Parmigiani, J. Electron Spectrosc., **100**, 215 (1999).

⁶⁴J. T. Yates, Ch.8 The Thermal Desorption of Adsorbed Species, in R. L.Park and M. G. Lagally (Ed.) Methods of Experimental Physics, Vol. 22 (Academic, New York) (1985).

⁶⁵J.B. Miller, H.R. Siddiqui, S.M. Gate1, J.N.R. Jr., J.T.Y. Jr., J.C. Tully, and M.J. Cardillo, J. Chem. Phys., **87**, 6725 (1987).

⁶⁶V.P. Zhdanov, Surface Science Reports, **12**, 183 (1991).

⁶⁷E. Habenschaden and J. Küppers, Surface Science, **138**, L147 (1984).

⁶⁸R. Raval and S. Munro, Journal of Electron Spectroscopy and Related Phenomena, **64–65**, 461 (1993).

⁶⁹M. Kazempoor and G. Pirug, Applied Physics A, **87**, 435 (2007).

⁷⁰M.R. Columbia, A.M. Crabtree, and P.A. Thiel, J. Am. Chem. Soc., **114**, 1231 (1992).

⁷¹P.R. Norton, R.L. Tapping, and J.W. Goodale, Surface Science, **72**, 33 (1978).

⁷²P. Hollins and J. Pritchard, Surface Science Letters, **99**, L389 (1980).

⁷³K. Nagai, Phys Rev Lett., **54**, 2159 (1985).

⁷⁴J.L. Daschbach, B.M. Peden, R.S. Smith, and B.D. Kay, Journal of Chemical Physics, **120**, 1516 (2004).

⁷⁵I.A. Bönicke, W. Kirstein, and F. Thieme, Surface Science, **307–309**, 177 (1994).

⁷⁶S.S. Fu and G.A. Somorjai, Surface Science, **262**, 68 (1992).

⁷⁷M. Behrens, Journal of Catalysis, **267**, 24 (2009).

- ⁷⁸ T. Fujitani and J. Nakamura, *Applied Catalysis A: General*, **191**, 111 (2000).
- ⁷⁹ M. Xi and B. E. Bent, *J. Phys. Chem.*, **97**, 4167 (1993).
- ⁸⁰ T. Koitaya, K. Mukai, S. Yoshimoto, and J. Yoshinobu, *Journal of Chemical Physics*, **138**, (2013).
- ⁸¹ L. Triguero, H. Ogasawara, M.G. Garnier, L.G.M. Pettersson, and A. Nilsson, *Journal of Electron Spectroscopy and Related Phenomena*, **128**, 179 (2003).
- ⁸² R. Raval, S.F. Parker, and M.A. Chesters, *Surface Science*, **289**, 227 (1993).
- ⁸³ M. Sano, T. Adaniya, T. Fujitani, and J. Nakamura, *The Journal of Physical Chemistry B*, **106**, 7627 (2002).
- ⁸⁴ D. Kolovos-Vellianitis, T. Kammler, and J. Küppers, *Surface Science*, **454**, 316 (2000).
- ⁸⁵ E.V. Thomsen, M. Christiansen, and J. Onsgaard, *Applied Surface Science*, **62**, 189 (1992).
- ⁸⁶ L. Chan and G.L. Griffin, *Journal of Vacuum Science & Technology A*, **3**, 1613 (1985).
- ⁸⁷ L. Chan and G.L. Griffin, *Surface Science*, **145**, 185 (1984).
- ⁸⁸ Z.-F. Wu, Z.-Q. Jiang, Y.-K. Jin, F. Xiong, G.-H. Sun, and W.-X. Huang, *Chinese Journal of Catalysis*, **37**, 1738 (2016).

List of Figures

Figure 1.1. Reaction network of simultaneous the methanol synthesis and water gas shift reaction ($\text{CO} + \text{H}_2\text{O} \rightarrow \text{CO}_2 + \text{H}_2$) reaction over Cu catalysts.....	3
Figure 1.2. Reaction network both methanol synthesis and reverse water gas shift on copper.....	4
Figure 1.3. Reaction scheme from formic acid to formate species on a Cu surface.....	5
Figure 2.1. Schematic diagram of IRAS chamber (top view).....	12
Figure 2.2. Schematic diagram of laboratory XPS chamber (top view).....	14
Figure 2.3. Schematic diagram of high-resolution XPS chamber (top view). (a) upper and (b) lower chamber.....	17
Figure 2.4. Photographs of single crystal of (a) Cu(111) and (b) Cu(997) mounted by sample holder used in IRAS and XPS chambers.....	19
Figure 2.5. A schematic model of the ideal Cu(997) surface.....	19
Figure 2.6. A photograph of the Zn deposition in an UHV chamber. The Zn is vapor-deposited onto the Cu(111) surface by radiation heating a zinc wire in a glass tube.....	21
Figure 3.1. Infrared light entering and reflecting on the metal surface (including P-polarized light and S-polarized light).....	25
Figure 3.2. Phase shift when S-polarized light is incident and reflected on the metal surface.	25

Figure 3.3. Phase shift when P-polarized light is incident and reflected on the metal surface.	25
Figure 3.4. Dynamic molecular and image dipoles when a molecule adsorbs its molecular plane parallel (left) or perpendicular (right) to the metal surface.....	26
Figure 3.5. Simulated TPD spectra based on Polanyi-Wigner equation.....	33
Figure 3.6. The demonstration of threshold TPD method using the simulated TPD spectra added the noise spectra.....	34
Figure 4.1. Model structures of adsorbed formic acid molecules as α - and β -polymeric formic acid.....	38
Figure 4.2. Multiplex TPD spectra of DCOOH adsorbed on Cu(111) at 85 K....	40
Figure 4.3. C1s XPS spectra of the saturated first layer HCOOH and CO saturation on Cu(111) at 83 K.....	42
Figure 4.4. TPD spectra of HCOOH adsorbed on Cu(111) at 85 K as a function of coverages.....	44
Figure 4.5. Arrhenius plot of TPD spectra for the first layer HCOOH on Cu(111) as a function of inverse temperature.....	47
Figure 4.6. The activation energy for desorption of HCOOH on Cu(111).....	47
Figure 4.7. TR-IRAS spectra of 0.26 ML HCOOH adsorbed on Cu(111) at 155.3 K as a function of elapsed time after the gas injection at $t = 0$ s.....	49
Figure 4.8. Internal vibrations of HCOOH, monodentate formate and bidentate formate species on Cu(111).....	50
Figure 4.9. (a) The plots of integrated area of monodentate formate $\nu(\text{C}=\text{O})$ as a function of elapsed time. (b) The plots of integrated area of formic acid $\pi(\text{O}-\text{H})$ as a function of elapsed time.....	54

- Figure 4.10. Arrhenius plot of $\ln(k_2)$ of $\pi(\text{O-H})$ for HCOOH on Cu(111).....55
- Figure 4.11. TR-IRAS spectra of 0.26 ML HCOOH adsorbed on Cu(111) at 165.1 K as a function of elapsed time after the gas injection at $t = 0$ s.....58
- Figure 4.12. TR-IRAS spectra of 0.5 ML HCOOH adsorbed on Cu(111) at 165.1 K as a function of elapsed time after the gas injection at $t = 0$ s.....61
- Figure 5.1. C 1s XPS spectra of clean (black), multilayer (green) and the first layer (red) cyclohexane on Cu(111) at 84 K.....69
- Figure 5.2. C 1s XPS spectra of clean (black) and CO saturation (red) on Cu(997) at 80 K.....69
- Figure 5.3. A series of (a) C 1s and (b) O 1s XPS spectra of HCOOH (0.28 ML) on Cu(111) at 80 K and subsequent annealing.....74
- Figure 5.4. A series of (a) C 1s and (b) O 1s XPS spectra of HCOOH (0.27 ML) on Cu(997) at 83 K and subsequent annealing.....78
- Figure 5.5. Multiplexed TPD spectra of HCOOH adsorbed on Cu(997) as a function of HCOOH exposure at 82 K. (a) mass = 29 (HCO^+ , the major cracking fragment of HCOOH) at lower HCOOH exposures (3~10 shots), (b) mass = 29 at higher HCOOH exposures (10~35 shots), (c) mass = 44 (CO_2^+) and (d) mass = 2 (H_2^+).....81
- Figure 5.6. Multiplexed TPD spectra of CO adsorbed on Zn-Cu(997) as a function of the coverage of Zn. (a) mass = 28 (CO^+), (b) mass = 64 (Zn^+) and (c) Zn coverage as a function of the integrated area of Zn desorption peak.....84
- Figure 5.7. TPD spectra of HCOOH adsorbed on Zn-Cu(997) as a function of HCOOH exposure at 82 K. (a) mass = 29 (HCO^+ , the major cracking fragment of HCOOH), (b) mass = 44 (CO_2^+), (c) mass = 2 (H_2^+) and (d) mass = 64 (Zn^+)....87
- Figure 5.8. The previous study for TPD of Zn on Cu(111) as a function of the

coverage of Zn. (a) low coverages from 0.15 to 4.48 ML; (b) high coverages from 0.34 to 30 ML.....88

Figure 5.9. TPD spectra of 5 shots HCOOH adsorbed on Zn-Cu(997) at 82 K as a function of the Zn coverage. (a) mass = 29 (HCO^+ , the major cracking fragment of HCOOH), (b) mass = 44 (CO_2^+), (c) mass = 2 (H_2^+) and (d) mass = 64 (Zn^+).90

Figure 5.10 (a) Integrated area for HCOOH and CO_2 desorption peaks as a function of HCOOH exposure. (b) The ratio of the integrated for CO_2 desorption peak to HCOOH desorption peak as a function of HCOOH exposure.....93

Figure 5.11. (a) A series of IRAS spectra of HCOOH on Cu(997) at 82 K as a function of HCOOH exposure. (b) A series of IRAS spectra of HCOOH (20 shots) on Cu(997) at 82 K and subsequent annealing.....96

Figure 5.12. (a) A series of IRAS spectra of HCOOH on Zn-Cu(997) at 82 K as a function of HCOOH exposure. (b) A series of IRAS spectra of HCOOH (20 shots) on Zn-Cu(997) at 82 K and subsequent annealing.....103

List of Tables

Table 4.1. Assignments of the observed vibrational peaks (cm^{-1}) of HCOOH and formate species on Cu(111).....50

Table 5.1. Assignments of the observed vibrational peaks (cm^{-1}) of HCOOH and formate species.....97

List of Publications

Papers included in this thesis:

Chapter 4:

Yuichiro Shiozawa, Takanori Koitaya, Kozo Mukai, Shinya Yoshimoto, and Jun Yoshinobu, “Quantitative analysis of desorption and decomposition kinetics of formic acid on Cu(111): The importance of hydrogen bonding between adsorbed species”, The Journal of Chemical Physics, **143**, 23, 234707-7pages, (December 2015).

Chapter 5:

Yuichiro Shiozawa, Takanori Koitaya, Kozo Mukai, Shinya Yoshimoto, and Jun Yoshinobu, in preparation.

Papers to which I have contributed but which are not included in this thesis:

1. Kaori Takeuchi, Susumu Yamamoto, Yuji Hamamoto, Yuichiro Shiozawa, Keiichiro Tashima, Hirokazu Fukidome, Takanori Koitaya, Kozo Mukai, Shinya Yoshimoto, Maki Suemitsu, Yoshitada Morikawa, Jun Yoshinobu, and Iwao Matsuda, “Adsorption of CO₂ on Graphene: A Combined TPD, XPS, and vdW-DF Study”, The Journal of Physical Chemistry C, **121**, 5, 2807-2814 (January 2017).
2. Shinya Yoshimoto, Yuichiro Shiozawa, Takanori Koitaya, Hiroyuki Noritake, Kozo Mukai, and Jun Yoshinobu, “Electronic states and electrical conductivity of the Si(111) native oxide surface adsorbed with electron donor tetrakis(dimethylamino)ethylene”, Journal of Applied Physics, **120**, 8, 085310-6pages (August 2016).

3. Takanori Koitaya, Susumu Yamamoto, Yuichiro Shiozawa, Kaori Takeuchi, Ro-Ya Liu, Kozo Mukai, Shinya Yoshimoto, Kazuma Akikubo, Iwao Matsuda, Jun Yoshinobu, "Real-Time Observation of Reaction Processes of CO₂ on Cu(997) by Ambient-Pressure X-ray Photoelectron Spectroscopy", *Topics in Catalysis*, **59**, 5, 526-531 (March 2016).
4. Takanori Koitaya, Yuichiro Shiozawa, Kozo Mukai, Shinya Yoshimoto, and Jun Yoshinobu, "Observation of Fano line shapes in infrared vibrational spectra of CO₂ adsorbed on Cu(997) and Cu(111)", *The Journal of Chemical Physics*, **144**, 5, 054703-8pages (January 2016).
5. Md. Zakir Hossain, Maisarah B. A. Razak, Hiroyuki Noritake, Yuichiro Shiozawa, Shinya Yoshimoto, Kozo Mukai, Takanori Koitaya, Jun Yoshinobu, and Sumio Hosaka, "Monolayer Selective Methylation of Epitaxial Graphene on SiC(0001) through Two-Step Chlorination–Alkylation Reactions", *The Journal of Physical Chemistry C*, **118**, 38, 22096–22101 (September 2014).
6. Shinya Yoshimoto, Masayuki Furuhashi, Takanori Koitaya, Yuichiro Shiozawa, Kazutaka Fujimaki, Yosuke Harada, Kozo Mukai, and Jun Yoshinobu, "Quantitative analysis of chemical interaction and doping of the Si(111) native oxide surface with tetrafluorotetracyanoquinodimethane", *Journal of Applied Physics*, **115**, 14, 143709-6pages (April 2014).